LENS - European Laboratory for Non-linear Spectroscopy
Universitá degli studi di Firenze

PhD Thesis
in Atomic and Molecular Spectroscopy
XXVII Cycle - FIS/03

1D bosons in optical lattices: from Superfluid to Bose glass

Lorenzo Gori

Supervisor: Prof. Giovanni Modugno
Coordinator: Prof. Roberto Righini

Florence - December 2014

CONTENTS

INTRODUCTION

With the macroscopic occupation of a single quantum state, Bose-Einstein condensates (BECs) represent the matter wave analogue of optical lasers. Like the invention of laser, also the discovery of BEC in 1995 [1] had a revolutionary impact on the development of atomic optics research and of quantum physics in general. For their properties of coherence and monochromaticity, BECs do represent very powerful tools for the investigation of many quantum problems related to different branches of physics [2]. As macroscopic quantum objects, whose wavefunction can be directly observed in the experiments, BECs widen the horizons of the quantum world.

The importance of BECs is enriched by the possibility to use optical lattices to trap and manipulate them. Behaving as ideal periodic potentials for atoms, that is without defects and lattice vibrations, optical lattices provide an extraordinary tool to experimentally study fundamental problems related to condensed matter physics, like, for instance, the Bloch theory for transport of electrons in metals [3–5]. As a matter of fact, a non-interacting BEC can be thought of as a unique macroscopic matter-wave whose dynamics in an ideal periodic potential can be related to that of a single electron in an ordinary crystal.

Moreover, the possibility to use Feshbach resonances [6, 7] to tune the interaction between the particles forming the BEC, further enriches the properties of the condensed many-body system. Interacting BECs in optical lattices do show very interesting phenomena: remarkably, when the lattice depth and

interactions are relatively small a BEC behaves like a superfluid, as demonstrated by several experiments like, for instance, the detection of quantized vortices [8, 9] or the frictionless flow below a critical velocity [10]. Conversely, when the lattice depth and interactions become large, different dissipation mechanisms may take place, eventually leading to a destruction of the superfluid behaviour [11]. A remarkable example, is the superfluid to Mott-insulator phase transition driven by pure quantum fluctuations, which causes the loss of the BEC phase coherence and the localization of atoms in correspondence of the lattice sites [12].

The physics of bosonic systems becomes even more fascinating when the periodic lattice is perturbed by a disordered potential. The celebrated phenomenon of Anderson localization [13], theoretically predicted in 1958 for electrons in crystals, has been recently observed using non-interacting BECs with laser speckles [14] and quasi-periodic optical lattices [15].

Finally, the complex interplay of disorder and interaction is expected to give rise to a new localized quantum phase, the Bose glass [16, 17]. Such a quantum phase, initially predicted by Giamarchi and Schulz in 1988, shares with the Mott insulator the property of being insulating and with the superfluid the property of being compressible, and thus characterized by a gapless excitation spectrum.

In this thesis we experimentally study fundamental problems related to the physics of bosonic systems at very low temperatures, close to the absolute zero, in the presence of both an ordered and a disordered optical lattice. We focus our study on one-dimensional (1D) systems which, besides being more accessible from a theoretical view point, exhibit very peculiar features such as, for instance, strong quantum phase fluctuations. Such phase fluctuations significantly affect the properties of a superfluid, leading to a new, quantum source of dissipation, the phase slips, besides the known classical energetic and dynamical instabilities. The first experimental evidence of quantum phase slips in a 1D atomic superfluid sample is reported in this thesis.

Thanks to the possibility offered by our experimental setup to independently control disorder and interactions, we explore for the first time the phase diagram describing the low-temperature properties of 1D disordered bosonic systems. Measurements of coherence, transport and excitation spectra highlight the features of a disordered insulator that extends from weak to strong interactions sorrounding the superfluid phase. Such a finite-T disordered insulator strongly resembles the $T = 0$ Bose glass phase predicted by theory. A comparison with theoretical analysis taking into account finite-temperature and inhomogeneity effects, confirm the experimental results.

The presentation of the thesis is organized as follows. In the first chapter I will introduce the main (experimental and theoretical) instruments related to the physics of BECs in 1D optical potentials. In the first part of the chapter I will focus on the experimental techniques employed to independently control interactions and disorder in the system, i.e. Feshbach resonances and quasi-periodic optical lattices, respectively. The importance and basic features of 1D systems will be described as well. The second part of the chapter, will introduce the disordered Bose-Hubbard model describing the several quantum phases that a 1D system can be subject to as the disorder and the interactions are suitably changed.

Chapter two and three respectively focus on the characterization of the superfluid phase (in a clean system) and of the Bose glass phase (in a disordered system). As for the clean case, I will first briefly describe the subtle relation between Bose-Einstein condensation and superfluidity. I will then introduce the concept of quasi-BEC, which characterizes 1D systems, both in terms of degeneracy temperature and of correlation length. By comparing coherence measurements with theoretical models we will show a new criterion to estimate the superfluid temperature for a 1D system in the lattice. The last part of chapter two is dedicated to the description of several transport measurements showing the different mechanisms of dissipation in a superfluid: the classical energetic and dynamical instability as well as the thermal and quantum phase slips due to the strong phase fluctuations present in 1D.

As for the disordered case, at the beginning of chapter three I will report on coherence and transport measurements showing the insulating properties of the system across the disorder-interaction plane. Theoretical studies, like Density Matrix Renormalization Group (DMRG) calculations and Exact diagonalization (ED) of the Hamiltonian for small homogeneous systems, will then show the different effects of finite temperature in the regimes of weak and strong interaction. Finally, measurements of the excitation spectrum will allow to probe the nature of the different insulating phases present in our inhomogeneous system. Thanks also to a theoretical model of fermionized bosons, such measurements will allow in particular to distinguish the gapless Bose glass from the gapped Mott insulator.

This PhD thesis is the result of experimental investigations I carried out in a research team at the European Laboratory for Non-linear Spectroscopy (LENS) in Florence from 2010 to 2014. Some of the experimental results have been compared to theory in a collaboration with Prof. T. Giamarchi (Geneva, Switzerland), Dr. G. Roux (Orsay, France) and Dr. I. P. McCulloch (Brisbane, Australia).

Many measurements reported and described in this thesis have been published in the two following journal articles:

- Transport of a Bose Gas in 1D Disordered Lattices at the Fluid-Insulator Transition. L. Tanzi, E. Lucioni, S. Chaudhuri, L. Gori, A. Kumar, C. D'Errico, M. Inguscio, and G Modugno. *Phys. Rev. Lett.* **111**, 115301 – Published 9 September 2013.

- Observation of a Disordered Bosonic Insulator from Weak to Strong Interactions. C. D'Errico, E. Lucioni, L. Tanzi, L. Gori, G. Roux, I. P. McCulloch, T. Giamarchi, M. Inguscio, and G. Modugno. *Phys. Rev. Lett.* **113**, 095301 – Published 25 August 2014.

Two other papers on the finite-T effects on disordered systems and on quantum phase slips are close to be submitted for publication.

CHAPTER 1

1D INTERACTING BEC IN QUASI-PERIODIC OPTICAL LATTICES

Contents

In this first chapter I will introduce the main ingredients that are necessary for the work described in this thesis, from both a theoretical and an experimental side. In Sec. 1.1 in particular, I will describe at a phenomenological level how Bose-Einstein condensation occurs and how a BEC, together with optical lattice potentials, is an excellent tool to experimentally manipulate both the interaction and the disorder in a 1D system.

In Sec. 1.2 I will then analyze the Bose-Hubbard (BH) model [18] describing the $T = 0$ many-body physics of interacting bosons in a lattice.

This model is particularly powerful as it allows to take into account quantum correlations between particles in the regime of strong interactions. The effect of disorder, which is our main interest, can be introduced in the model as well. I will thus report an overview of the quantum phases that a 1D system can undergo when both interaction and disorder are changed.

1.1 BEC with tunable interaction and disorder in 1D

Bose-Einstein condensation is a quantum phenomenon that occurs as a macroscopic number of identical bosons in thermal equilibrium occupy the same quantum (ground) state. As a result, quantum effects become relevant on a macroscopic scale. This condition, which was predicted in 1925 by A. Einstein and S. N. Bose [19, 20], was experimentally achieved in 1995 in a dilute gas of ^{87}Rb atoms [1]. Later on, many other atomic samples, among which ^{39}K, have been brought to the condensation[1].

In order to qualitatively understand how the phase transition to the Bose-Einstein condensate occurs, let us consider (Fig. 1.1a) a gas of atoms in thermal equilibrium with a thermal velocity v and a density $n = d^{-1/3}$, d being the mean distance between the particles. At room temperature T_R, the

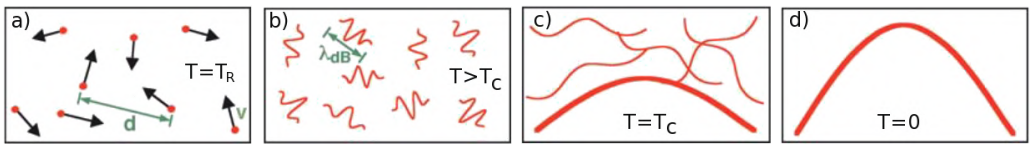

Figure 1.1: Phase transition to the BEC. (**a**) Classical distinguishable particles at room temperature T_R. (**b**) Spatial extension λ_{DB} of the wave functions associated to the particles at $T > T_c$. (**c**) wave functions overlap ($\lambda_{DB} \approx d$): a macroscopic fraction of undistinguishable bosons start condensing at $T = T_c$. (**d**) Giant wave of matter (pure BEC) at $T = 0$. Figure adapted from [21].

[1]The other samples that have been condensed are mainly of alkaline, alkaline earth, and lanthanoid atoms: ^{23}Na, ^{7}Li, H, ^{85}Rb, ^{4}He*, ^{41}K, ^{133}Cs, ^{52}Cr ^{40}Ca, ^{84}Sr, ^{86}Sr, ^{88}Sr, ^{133}Cs, ^{174}Yb ^{164}Dy and ^{168}Er.

atoms of the dilute gas are point-like particles and can therefore be spatially distinguished (classical phase). At lower temperatures (panel b), the wave-like behaviour of matter must be taken into account and the spatial extension of a particle can be suitably described in terms of its De Broglie wavelength:

$$\lambda_{DB} = \frac{h}{\sqrt{2\pi\, m k_B T}} \tag{1.1}$$

where m is the mass of the atoms, T is the gas temperature and h and k_B are respectively the Planck and Boltzmann constants. As the temperature of the system decreases, the width λ_{DB} of the wave function associated to the particles increases according to Eq. 1.1[2]. For low enough temperatures (panel c), when $\lambda_{DB} \approx d$, the wave functions start overlapping and consequently the particles are not distinguishable any longer.

Depending on the quantum nature of the particles, i.e. whether fermionic (half-odd integer spin) or bosonic (integer spin), two different phenomena can occur as the gas is cooled down below a critical temperature T_c. Fermions, in agreement with the Pauli exclusion principle, occupy different energy levels starting from the ground state and with increasing energy (degenerate Fermi gas). Bosons, which conversely may occupy the same position and the same single-particle state, form a macroscopic matter wave oscillating in phase as a unique coherent object (BEC). Ideally, for $T = 0$ (panel d), all the particles fall in the ground state and a pure Bose-Einstein condensate without any thermal component is formed.

It is important to note that Bose-Einstein condensation is a pure quantum phenomenon as it is driven only by quantum statistics which gives rise to a sort of effective (T-dependent) potential, attractive in the case of bosons (repulsive in the case of fermions). As a matter of fact this phase transition does not rely on the interactions between particles that, instead, may reduce the quantum effects and eventually lead to the destruction of the BEC, as we shall see in the next chapter.

[2]Note that this is in agreement with the Heisenberg principle as the reduction in the particle velocity uncertainty at low temperatures results in a increase in its position uncertainty, that is in its De Broglie wavelength.

The qualitative description of the Bose-Einstein condensation just shown can be made more quantitative in terms of the *phase-space density* $n\lambda_{DB}^3$, which is a parameter that describes the degree of quantum-mechanical behaviour of the system. For a system of non interacting particles (ideal Bose gas) the BEC phase transition can be analytically shown [22] to occur when

$$n\lambda_{DB}^3 = 2.612 \tag{1.2}$$

For a gas of ^{87}Rb at room temperature and pressure of 1 Atm, $n\lambda_{DB}^3 \approx 10^{-8}$, i.e. eight orders of magnitude lower than the condition 1.2 for the phase transition. In principle, such a condition could be satisfied both by increasing the density n and by decreasing the temperature T, being $\lambda_{DB} \propto T^{-1/2}$ (see equation 1.1). Nevertheless, for normal densities, at sufficiently low temperatures all the known interacting systems, with the exception of helium, become solid. In order to avoid such an undesired transition to the solid phase, very dilute samples[3] have to be employed and, consequently, the atoms have to be cooled down to very low temperatures, of the order of 100 nK.

1.1.1 Feshbach resonances

So far we have assumed to deal with an ideal BEC, thus neglecting the interactions between the particles forming the condensate. In dilute cold gases[4] only binary collisions are relevant and the two-body interaction potential $v(\boldsymbol{x} - \boldsymbol{x'})$ can be written in terms of a contact pseudo-potential as:

$$v(\boldsymbol{x} - \boldsymbol{x'}) = g\,\delta(\boldsymbol{x} - \boldsymbol{x'}) \qquad \text{with} \qquad g = \frac{4\pi\hbar^2}{m}\,a \tag{1.3}$$

where a is the scattering length. The *scattering length*, which is positive in the case of repulsive interactions and negative in the case of attractive ones[5],

[3]Note that the lower the pressure, the lower the probability of inelastic three-body collisions and the higher the lifetime of the metastable Bose-condensed phase.

[4]The diluteness condition for a cold gas is $d \gg a$, that is the mean inter-particle distance d has to be much greater than the scattering length a of the two body potential.

[5]In the following only positive a will be considered since for $a < 0$ a condensate is stable only for a very small number of atoms. As a matter of fact, above a certain critical number, the condensate collapses due to three-body inelastic collisions caused by the attractive interaction.

is the only relevant parameter when describing the collisional properties of a system at very low energies.

Let us now show how it is possible to tune the intensity of the scattering length, and thus the intensity of the interactions, by means of Feshbach resonances. First studied in nuclear physics [23–25], Feshbach resonances later on became important in atom physics [6, 7, 26] as they offer the possibility to tune the interactions in a controlled way simply by changing a magnetic field.

In order to describe the basic idea of Feshbach resonance, we consider (see Fig. 1.2) two diatomic molecular potential curves, $V_{op}(R)$ (ground state) and $V_{cl}(R)$ (excited state), corresponding to two spin configurations for atoms[6]. For large internuclear distances R, the potential $V_{op}(R)$ corresponds to the

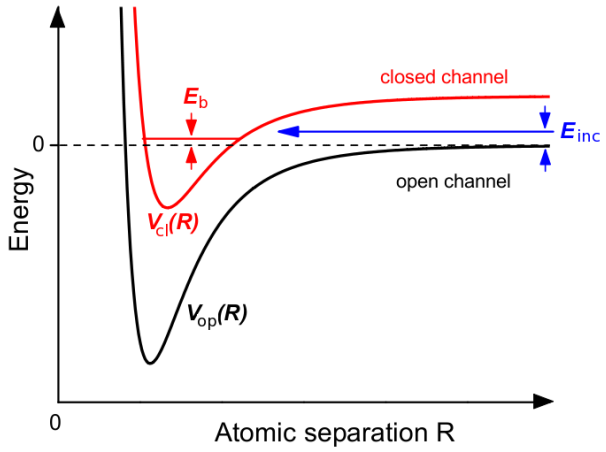

Figure 1.2: Basic model for Feshbach resonances. The scattering resonance occurs when two atoms colliding at energy E_{inc} in the open channel $V_{op}(R)$, resonantly couple to a molecular bound state with energy E_b, supported by the closed channel potential $V_{cl}(R)$. The relative energy of the two levels is controlled via magnetic field when the corresponding magnetic moments are different. Figure adapted from [27].

energy of the two free atoms[7] (dashed line), which is chosen here as energy

[6]In principle, a molecule has several potential curves corresponding to the different hyperfine and Zeeman levels. For simplicity, we consider here only one excited state, which is appropriate for an isolate resonance.

[7]Neglecting the Zeeman effect, the energy at $R \to \infty$ is exclusively determined by the

reference ($V_{op}(\infty) = 0$). As the two atoms collide with a very small incident energy E_{inc}, the level $V_{op}(R)$ - called *open channel* - is energetically accessible for a collisional process. The other potential $V_{cl}(R)$, which is not accessible (*closed channel*), may however have a bound molecular state close to 0. If now the two atoms have the possibility to make a (temporary) transition to this bound molecular state, then their scattering cross section can extremely increase. The (Feshbach) resonance may indeed take place as the energy level of the closed channel can be tuned, with respect to the open one, by varying a magnetic field. As a matter of fact, provided that the states corresponding to the two channels have different magnetic moments, i.e. they have a different response (Zeeman shift) to the applied magnetic field B, this one can be tuned in such a way that the energy E_b of the bound molecular state approaches E_{inc}.

Near a Feshbach resonance, the magnetic field dependence on the scattering length a is given by [28]

$$a(B) = a_{bg}\left(1 - \frac{W}{B - B_0}\right) \tag{1.4}$$

where B_0 is the *resonance center*, W the *resonance width* and a_{bg} the *background scattering length*, i.e. the scattering length far from the resonance. A plot of the scattering length a as a function of the magnetic field B is reported in Fig. 1.3. The figure shows the ^{39}K resonance at $B_0 \simeq 402\,\mathrm{G}$, that is also used in our experiment[8].

An important point of a Feshbach resonance is the *zero-crossing magnetic field* $B_{zc} = B_0 - W$, i.e. the value of B at which a vanishes. The behaviour of the scattering length in proximity of B_{zc}, as derived by Eq. 1.4, is given by

$$a(B) = \frac{a_{bg}}{W}(B - B_{zc}) \qquad \text{for} \qquad B \to B_{zc} \tag{1.5}$$

The parameter that is important in order to control the interaction around

sum of the hyperfine energies of the two free atoms.

[8]The resonance at $B_0 \simeq 402\,\mathrm{G}$ is accessible when the BEC is in the substate $|F = 1, m = 1>$, where F and m respectively label the hyperfine and Zeeman levels of the ^{39}K ground state.

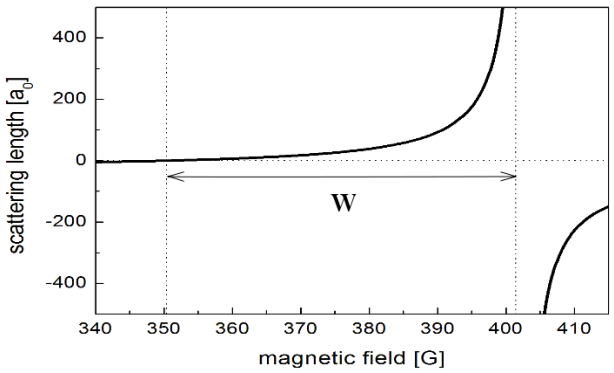

Figure 1.3: Magnetic field dependence of the scattering length a between the ^{39}K Feshbach resonance at $B_0 \simeq 402\,\mathrm{G}$ and the zero-crossing $B_{zc} \simeq 350\,\mathrm{G}$. Note that the small ratio a_{bg}/W ($\approx 0.5\,a_0/\mathrm{G}$) allows to change to zero the interactions of a ^{39}K BEC with high degree of accuracy.

the value $a = 0$, is the ratio a_{bg}/W: the smaller this ratio, the better the accuracy for tuning the interaction. For the resonance shown in figure, whose width is $W \simeq 52\,\mathrm{G}$ and $a_{bg} \simeq -29\,a_0$ (a_0 being the Bohr radius), the sensitivity around $B_{zc} = 350\,\mathrm{G}$ is $da/dB \simeq 0.56\,a_0/\mathrm{G}$. This means that with a stability, for instance, of 1 G for the magnetic field, the interactions of the BEC can be changed to zero with an uncertainty of about half a Bohr radius.

BEC of Potassium-39. All the experiments described in this thesis are performed using a BEC of Potassium-39 with tunable interactions [29]. The experimental setup employed to produce the BEC is largely described in previous theses at the "BEC-2" laboratory at LENS [30–34]. In the following I will recall only a few general properties of our sample.

^{39}K has a natural negative scattering length [35, 36], corresponding to an attractive interaction, which would make the BEC collapse [37–39]. Nevertheless, by using the Feshbach resonance at 402 G, it is possible not only to condense ^{39}K, by tuning the scattering length to positive values, but also to control the interaction energy at will as just described. ^{39}K is thus an excellent sample for the production of a BEC with tunable interaction.

At zero magnetic field the collisional properties of ^{39}K do not favour direct

evaporative cooling [40, 41]. For this reason, as a first stage before using the Feshbach resonance in the optical trap, we need to employ ^{87}Rb to sympathetically cool down ^{39}K. In spite of the small heteronuclear scattering length for the ^{39}K - ^{87}Rb collisions [42, 43], the sympathetic cooling for ^{39}K has been proven to work efficiently [41]. Recently, a new experiment in Florence [44] showed that it is possible to condense ^{39}K without employing other atomic species, provided that an efficient sub-Doppler cooling is performed and a deep optical trap is available.

1.1.2 Quasi-periodic optical lattice

Let us now introduce the second key ingredient that will allow us to suitably describe the behaviour of real systems, i.e. the *disorder*. The possibility to manipulate the disorder in ultracold systems with laser light is quite remarkable, especially as compared with the real systems in nature, where conversely the disorder – which is intrinsically present[9] – can not be controlled.

Many techniques have been exploited to create disordered potentials; a standard way is to employ the laser speckle technique [46–48]. The interference between the partial waves (randomly shifted in phase) scattered from the various facets of the rough surface of a diffuser, produces a random intensity distribution of light (spackle pattern). The typical length-scale l of the speckle grains depends on the numerical aperture NA of the optical system, $l \simeq \lambda/NA$, with λ the laser wavelength ($\lambda = 1064\,\mathrm{nm}$ in our case). Due to the limited optical access of our setup ($NA \sim 0.1$) the minimum speckle size achievable in our case would be quite large ($l \approx 10\,\mu\mathrm{m}$), i.e of the same order of magnitude of the BEC size (about $20\,\mu\mathrm{m}$). For this reason, in order to produce the disorder, we employed a quasi-periodic optical lattice whose "grain size" l is quite smaller as it is given by the lattice constant $d \approx 0.5\,\mu\mathrm{m}$.

A quasi-periodic optical potential can be obtained by superimposing to

[9] Note that the disorder plays a key role in nature as it, for instance, affects the transport properties of electrons in crystals [45].

an optical lattice with wavelength λ_1 a weaker one with an incommensurate wavelength λ_2, i.e. such that the ratio $\beta = \lambda_1/\lambda_2$ is an irrational number [49, 50]. Let us define the periodic potentials with wavelength λ_1 and λ_2 respectively as the *main lattice* potential V_1 and the *secondary lattice* potential V_2 (see Fig. 1.4 on the left); the quasi-periodic optical lattice, also known as bichromatic lattice, is then characterized by the potential

$$V(x) = V_1(x) + V_2(x) = s_1 E_{r1} \sin^2(k_1 x) + s_2 E_{r2} \sin^2(k_2 x) \tag{1.6}$$

where $k_i = 2\pi/\lambda_i$ $(i = 1, 2)$ are the lattice wavenumbers and s_i are the lattice heights in units of the recoil energies $E_{r,i}$[10]. A plot of Eq. 1.6 for $s_1 = 10$ and

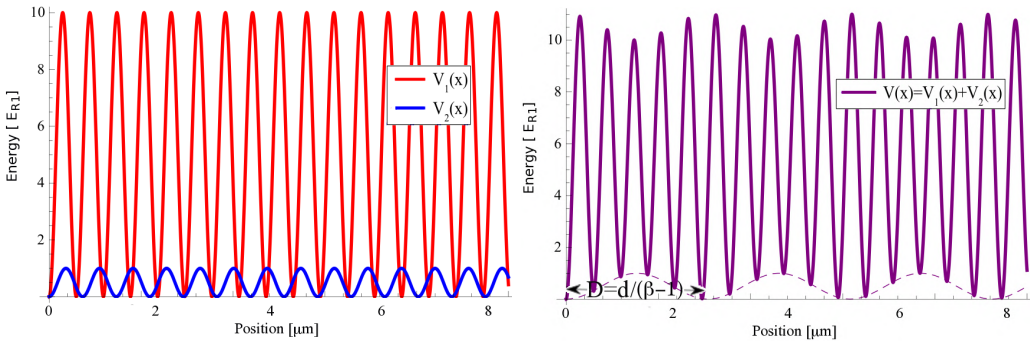

Figure 1.4: Quasi-periodic optical lattice (**right**) as a result of the superposition between two perfect lattices (**left**), one with $s_1 = 10$ and $\lambda_1 = 1064\,\text{nm}$ (red) and the other with $s_2 = 1$ and $\lambda_2 = 862\,\text{nm}$ (blue). The modulation (dashed line) induced by the secondary lattice produces a sequence of wells D apart, whose lattice sites with lower energy are at different potential heights.

$s_2 = 1$ is shown in Fig. 1.4 (on the right) where the modulation induced by the secondary lattice at the beating frequency $c\,(k_2 - k_1)$ is highlighted with a dashed line.

Provided that $s_2 \ll s_1$ and β is an irrational number, the secondary lattice induces a perturbation in the main one, resulting in an inhomogeneous and non-periodic shift of the energy minima. In other words, the effect of the

[10]The recoil energy $E_r = \hbar^2 k^2/2m$ is the kinetic energy with which an atom initially at rest recoils when it absorbs a photon with momentum $\hbar k$. This energy can also be thought of as the ground state energy $E = \hbar^2\pi^2/2md^2$ of a particle confined within a 1D-box of length $d = \lambda/2$, i.e. the lattice spacing.

secondary lattice is to produce a sequence of wells $D = d/(\beta - 1)$ apart, whose lattice sites at the bottom have different potential heights. This shift of the energy minima is in a range of size $s_2\beta^2$, thus proportional to the secondary lattice height s_2.

Moreover, it is possible to demonstrate [51] that the perturbation induced by the secondary lattice does not change significantly the position of the lattice sites, i.e. if $s_2 \ll s_1$ the position of the bichromatic lattice sites are $x_j \simeq d \cdot j$, d being the period of the main lattice.

Finally we note that the disorder introduced by using a bichromatic lattice is not a pure random disorder as it has a quasi-periodic structure, characterized by the frequencies ck_1, ck_2 and $c(k_2 - k_1)$. However the quasi-periodic potential breaks the translational invariance of a perfect lattice, and it can be thus used to study the physics of disordered systems.

1.1.3 1D systems

In this thesis we aim to study the physics of interacting disordered bosons focusing on the 1D case. The importance of 1D systems doesn't rely only on its theoretical simplicity. Besides being easier to be analytically and numerically studied than systems with higher dimensionality, 1D systems are also conceptually interesting for at least two reasons. First, they allow to reach the regime of strong interactions[11] where phase fluctuation effects become relevant, as we shall see in the next chapter. Second, the progress in material science in the last twenty years highlighted the existence of more and more bulk materials exhibiting very anisotropic magnetic and electronic properties that show a 1D structure inside. This is the case, for instance, of some organic conductors [52–56] or spin [57, 58] and ladder compounds [59, 60]. Moreover, with the enormous progress in chemical synthesis and

[11] In 3D, interactions mix the spatial degrees of freedom and the resulting interaction energy is redistributed along all three directions. When one tries to increase the interaction, the radial broadening of the atomic distribution lowers the density and, in turn, the interaction energy itself. In 3D is thus impossible to achieve interaction energies larger than the radial harmonic one.

nano-technologies many isolated 1D systems have been realized. Such systems, where electrons are confined to move along one channel, show plenty of interesting quantum effects. Remarkable examples are quantum wires [61, 62], Josephson junction arrays [63], edge states in quantum Hall systems [64], nanotubes [65, 66] and superconductors [67–69].

Let us thus discuss how it is possible to realize 1D systems and what are the conditions to be fulfilled. In the case of ultra-cold atoms, 1D systems (let say along the z direction) can be realized by means of a harmonic confining potential generated by two Gaussian beams along the orthogonal (x and y) directions. The intensity of such a potential must be large enough to freeze the orthogonal degrees of freedom, such that the dynamics of the system, and thus the physics of interest, occurs only along z. The resulting wavefunction can be thus factorized along z and $r = \sqrt{x^2 + y^2}$ as

$$\Psi(z, r) = \phi(z)\, e^{-r^2/2a_r^2} \tag{1.7}$$

where the second term is a Gaussian function with width $a_r = \sqrt{m\omega_r/\hbar}$ due to the radial harmonic confinement with frequency ω_r. The energy of the system can be written as the sum of the radial and axial terms as

$$E = E_z + \hbar\omega_r(n_r + 1) \tag{1.8}$$

where $n_r = n_x + n_y$, with n_x and n_y integer numbers. The system is thus characterized by radial quantized energy levels. If the temperature $k_B T$ and the interaction energy U are much smaller than the energy separation $\hbar\omega_r$ between the radial energy levels, i.e. if

$$k_B T,\, U \ll \hbar\omega_r, \tag{1.9}$$

then only the radial ground state is populated (see Fig. 1.5a on top). As for the axial wavefunction $\phi(z)$, its shape of course depends on the specific potential along z but even in the simplest case there will be an axial confinement due to the optical harmonic trap with frequency $\omega_z \ll \omega_r$. As a result,

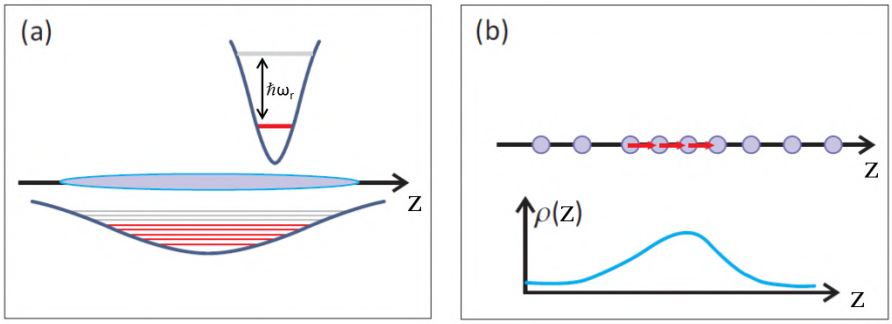

Figure 1.5: (**a**) Schematics of a 1D system. Due to the strong transverse harmonic confinement ($\hbar\omega_r \gg k_B T, U$) the radial degrees of freedom are frozen and only the ground state is occupied, contrary to what occurs along the axial (z) direction. Occupied levels are represented in red, empty levels in gray. (**b**) Collective excitation propagating along a 1D system of fermionized bosons. The excitation corresponds to a density wave $\rho(z)$ with length-scale larger than the interparticle spacing.

depending on their temperature and interaction energy, the atoms will be able to occupy several longitudinal energy levels but will still be in the radial ground state, as shown in Fig. 1.5a.

Fermionized bosons. Interacting 1D fluids, no matter if the particles are fermions or bosons, belong to a universality class of systems referred to as "Luttinger liquids" [70]. Such universality derives from the absence of a well-defined concept of statistics in 1D. As a consequence, under certain conditions fermionic particles can be described in terms of a bosonic field, and equivalently, bosonic systems can display fermion-like properties. The latter phenomenon in particular, which is usually referred to as "fermionization" of bosons, will be of particular relevance in chapter 3 when describing the localization of strongly interacting particles in the presence of disorder. As a general property, because of inter-particle interactions, if any atom tries to move, it inevitably pushes its neighbour along the 1D axis, which in turn pushes the other neighbour and so on. As a result, there will be a density wave propagating along the 1D system: no individual motion is possible and any individual excitation becomes a collective one, as illustrated in Fig. 1.5b.

These phenomena can be described in a more quantitative way introducing the *Lieb-Liniger* parameter characterizing the interaction strength of 1D bosons in the continuum [71]:

$$\gamma = \frac{m}{\hbar^2 n_{1D}} g_{1D} \qquad \text{with} \qquad g_{1D} = \frac{2\hbar^2}{m a_r^2} \frac{a}{(1 + Ca/a_r)} \tag{1.10}$$

and with $C = 1.0326$. γ is thus the ratio between the interaction energy $g_{1D} n_{1D}$ and the kinetic energy $\hbar^2 n_{1D}^2/m$ required to bring particles at a distance n_{1D}^{-1}. We note that far from a Feshbach resonance where $a \ll a_r \approx 1400\, a_0$, $g_{1D} \propto a$ as in the 3D case. We also note that $\gamma \propto n_{1D}^{-1}$, meaning that contrarily to the 3D case, as the density n_{1D} increases, interactions decrease with respect to the kinetic energy.

In terms of γ we can now say that the system is in the fermionic limit (Tonks-Girardeu gas [72]) if $\gamma \gg 1$ while it is in the bosonic limit if $\gamma \ll 1$. From an experimental point of view, by varying the scattering length a we can tune γ from about 0 up to values of the order of 10.

1.2 Disordered Bose-Hubbard model

After formally introducing the main features of the disordered Bose-Hubbard (DBH) model, in this section I will describe the several regimes of physical interest. Starting from the condition of null disorder, in Subsec. 1.2.1 I will describe firstly the interaction-induced transition from a conductive to an insulating phase (Mott insulator) taking also into account the experimental case of an inhomogeneous trapped system. In Subsec. 1.2.2 I will then consider the effect of disorder starting from the case of null interaction: above a disorder threshold value a transition to another insulating phase will be shown to take place (Anderson localization). Finally, in Subsec. 1.2.3, I will consider the delocalizing effect of weak interactions and the theoretical expectation for the strongly-interacting Bose glass phase driven by disorder.

The quantum state of a gas of identical interacting bosons in an optical lattice potential V_{latt} and in the presence of an external potential V_{ext}, can be described [73] by the second quantization Hamiltonian

$$\hat{H} = \int d^3x\, \hat{\psi}^\dagger(\boldsymbol{x}) \left[-\frac{\hbar^2\nabla^2}{2m} + V_{latt}(\boldsymbol{x}) + V_{ext}(\boldsymbol{x}) + \frac{g}{2}\hat{\psi}^\dagger(\boldsymbol{x})\hat{\psi}(\boldsymbol{x}) \right] \hat{\psi}(\boldsymbol{x}) \tag{1.11}$$

where $\hat{\psi}(\boldsymbol{x})$ is a boson field operator and the coefficient g is linearly related to the scattering length a, according to Eq. 1.3. A Bloch wavefunction describing the quantum state of a particle in a lattice can be expressed as a superposition of Wannier functions localized at the lattice sites. This kind of description is particularly convenient when one wants to describe atom-atom on-site interactions. Moreover, under the assumption that the energies involved in the system are small enough not to induce inter-band excitations, we can restrict ourselves to consider only the lowest energy band $n = 0$; the boson field operators can then be written in terms of Wannier functions (omitting the band index) as follows

$$\hat{\psi}(\boldsymbol{x}) = \sum_i \hat{a}_i w(\boldsymbol{x} - \boldsymbol{x}_i) \tag{1.12}$$

$\hat{a}_i$ being the annihilation operator of one boson at the i-th lattice site and $w(\boldsymbol{x}-\boldsymbol{x}_i)$ being the Wannier function localized at the i-th site position x_i. By substituting this equation in 1.11 and considering only the tunneling between neighbouring sites, one can obtain the disordered *Bose-Hubbard Hamiltonian*

$$\hat{H}_{DBH} = -J \sum_{\langle i,j \rangle} \hat{a}_i^\dagger \hat{a}_j + U \sum_i \frac{\hat{n}_i(\hat{n}_i - 1)}{2} + \sum_i \epsilon_i\, \hat{n}_i \tag{1.13}$$

where $\hat{a}_i$ and $\hat{a}_i^\dagger$ are the boson annihilation and creation operators satisfying the canonical commutation relation $[\hat{a}_i, \hat{a}_j^\dagger] = \delta_{ij}$, $\hat{n} = \hat{a}_i^\dagger \hat{a}_i$ is the number operator representing the number of particles at the i-th lattice site, and the symbol $\langle i, j \rangle$ indicates that the sum has to be considered only between nearest neighbouring sites. As for the quantities J, U and ϵ_i, they are particularly important as they define the energy scales of the system:

- $J = -\int d^3x\, w^*(\boldsymbol{x} - \boldsymbol{x}_i) \left[-\frac{\hbar^2}{2m}\nabla^2 + V_{latt}(x)\right] w(\boldsymbol{x} - \boldsymbol{x}_j)$ is the *tunneling energy* which is related to the overlap between the Wannier functions localized at the i-th and j-th sites. As it represents the probability for an atom to hop from one site to another it can be thought of as a measure of the delocalization of the particles throughout the lattice.

- $U = \frac{4\pi\hbar^2}{m}\, a \cdot \int d^3x\, |w(\boldsymbol{x})|^4$ is the *on-site interaction energy*, i.e. the energy related to the repulsive ($a > 0$) interaction between two atoms at the same lattice site. Note that in the BH Hamiltonian U is multiplied, for each lattice site, by the number of atom pairs $\hat{n}_i(\hat{n}_i - 1)/2$, in agreement with the fact that a site with $n_i = 0, 1$ does not contribute to the total interaction energy. Note also that interactions among atoms of different sites are here neglected.

- $\epsilon_i = \int d^3x\, V_{ext}(\boldsymbol{x})|w(\boldsymbol{x} - \boldsymbol{x}_i)|^2 \approx V_{ext}(\boldsymbol{x}_i)$ is the lattice *site energy offset*. This energy contribution to the system may arise from two factors: the first one is the external trap potential, which usually varies smoothly across the lattice such that the energy ϵ_i within each lattice site can be assumed constant; the second factor is the disorder, which can be produced by means of the laser techniques previously discussed. In the case of a quasi-periodic optical lattice, $\epsilon_i \in [-\Delta, \Delta]$ where $2\Delta \simeq \beta^2 s_2 E_{r2}$ is the energy range of the disorder induced by the secondary lattice of depth s_2 [74].

We want to calculate now the integrals J and U and express them in terms of the optical lattice depth which is the parameter that can be controlled in the experiments. For the moment let us consider the more general case of a 3D optical lattice potential:

$$V_{latt} = \sum_j V_{0,j}\, sin^2(kx_j) \qquad j = x, y, z \tag{1.14}$$

where $V_{0,j}$ is the lattice depth along the j-th direction, which is usually expressed in terms of recoil energies E_r as the dimensionless quantity

$$s_j = \frac{V_{0,j}}{E_r} \qquad \text{with} \qquad E_r = \frac{\hbar^2 k^2}{2m}. \tag{1.15}$$

Under the assumption that around each minimum of the lattice potential this one can be approximated by a harmonic potential well ($sin^2 x \approx x^2$), the corresponding Wannier functions at each site i can be approximated as follows

$$w_i(\boldsymbol{x}) = \prod_{j=1}^{3} \left(\frac{k s_j^{\frac{1}{4}}}{\sqrt{\pi}} \right)^{\frac{1}{2}} e^{-(k\,x_j)^2 \sqrt{s_j}/2} \tag{1.16}$$

i.e. Gaussian functions whose width $a_j = k^{-1} s_j^{-1/4}$ decreases as the optical lattice depth s_j increases. With such an approximation for $w_i(x)$, it is possible to analytically calculate the above integrals for J_j (along each direction $j = x, y, z$) and U:

$$J_j = \frac{4}{\sqrt{\pi}} E_r\, s_j^{3/4}\, e^{-2\sqrt{s_j}}\,; \qquad U = \sqrt{\frac{8}{\pi}}\, E_r k\, a \left(\prod_{j=1}^{3} s_j \right)^{1/4} \tag{1.17}$$

From equations 1.17 we observe that increasing the optical lattice depth s_j yields to an increase of the ratio U/J_j since it corresponds to:

- an exponential drop of the tunneling energy J_j as a consequence of the higher barrier that the particles have to hop in order to tunnel from one site to another.

- an increase in the interaction energy U as a consequence of the tighter confinement of the particle density distribution within each lattice site.

To sum up, the quantum phase of the system depends on the interplay between the just described three energy scales: the tunneling energy J_j (related to s_j), the interaction energy U (related to s_j and the scattering length a) and the disorder parameter Δ (related to s_2).

1.2.1 Clean system: SF-MI phase transition

Let us start considering the ideal case of a translationally invariant 1D system in which there is no trap potential and no disorder; as the site energy

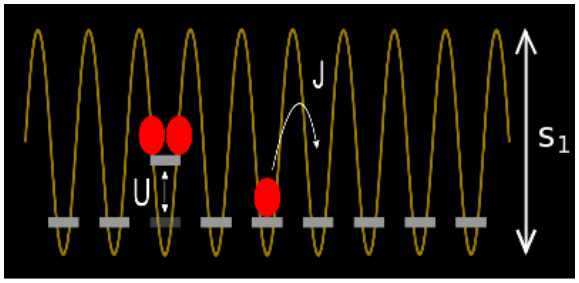

Figure 1.6: Homogeneous Bose-Hubbard model (ϵ_i = const). The energy of the system increases of the amount U, due to the repulsive interaction between two atoms sharing the same site, and decreases of the amount J, due to a particle hop from one site to another. Note that the higher the potential depth s_1, the larger the ratio U/J.

level ϵ_i is constant all over the lattice, we can neglect the last term in the DBH Hamiltonian 1.13 which thus reduces to

$$\hat{H}_{BH} = -J \sum_{\langle i,j \rangle} \hat{a}_i^\dagger, \hat{a}_j + U \sum_i \frac{\hat{n}_i(\hat{n}_i - 1)}{2} \tag{1.18}$$

The Bose-Hubbard model in the homogeneous case is illustrated in Fig. 1.6. Depending on the ratio U/J between the two remaining energy terms the system may show two quantum phases with different and well defined features, i.e. the superfluid phase and the Mott insulator phase.

When $U \ll J$, that is the first term in Eq. 1.18 is the dominant one, each atom is delocalized throughout the lattice and the system is said to be a *superfluid* (SF). Let us define the Bloch lowest energy state of a single delocalized particle as the superposition $\sum_i \hat{a}_i^\dagger|0\rangle$ of the wavefunctions localized on each lattice site; the ground state of the system of N identical bosons can be then written as

$$|\Psi_{SF}\rangle = (\sum_i \hat{a}_i^\dagger)^N|0\rangle \tag{1.19}$$

that is the product of the N single-particle delocalized states. The system is thus described by one macroscopic wavefunction whose phase is consequently constant and well defined on each lattice site. As a consequence, the density distribution of the atoms after a free expansion[12] from the lattice, shows

[12]After a free expansion (*time-of-flight*) of a few tenths of ms, the spatial density

sharp peaks $2\hbar k$ apart resulting from the interference of the phase coherent matter wave (see Fig. 1.7).

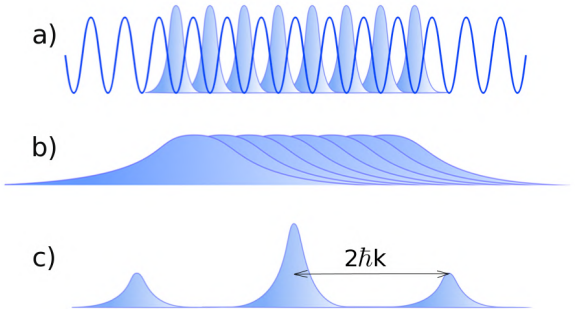

Figure 1.7: Interference pattern of the momentum density distribution after a free expansion from an optical lattice. (**a**) If the lattice height is low enough such that $J \gg U$, the Wannier functions localized at each site are phase locked to each other due to the tunneling. (**b**) When the optical lattice is switched off, the Wannier wavefunctions are free to expand. The narrower the initial (spatial) density distribution, the broader the final (momentum) density distribution. (**c**) The phase-locked expanded functions interfere each other giving rise to sharp peaks $2\hbar k$ apart, whose envelope is given by the single site density distribution.

In a SF, thus, while for each site the phase is perfectly defined, the number of particles per site is not determined and exhibits Poissonian fluctuations. This is in agreement with the Heisenberg uncertainty principle for which the phase operator $\hat{\phi}_i$ and the number operator $\hat{n}_i$ are conjugate variables that obey to the commutation relation $[\hat{\phi}_i, \hat{n}_i] = i$.

When $U \gg J$, that is the second term in Eq. 1.18 is the dominant one, for the system is energetically convenient that the atoms remain still and localized in correspondence of the energy minima: an atom jumping from a site to a neighbour one would cause an energy cost for the system equal to

distribution $|\Psi(\boldsymbol{x})|^2$ of a non-interacting BEC approaches the density distribution $|\Psi(\boldsymbol{p})|^2$ in the momentum space. This is regardless of the shape of the trapping potential. In the particular case of a BEC initially confined in an optical lattice with period d, the matter wave shows interference peaks approximately $1/d$ apart which recall the interference pattern of a diffraction grating. In that case, the lower the slits aperture, the larger the number of peaks; correspondently here, the smaller the width of the confined Wannier functions (i.e. the higher the lattice height), the larger the number of peaks.

U. This system is said to be a *Mott insulator* (MI). The strong repulsive interaction forces the particles not to share the same sites, leading to a homogeneous and well defined distribution of the particles across the lattice. For a given chemical potential μ, the particle number per site is thus well determined and the ground state of the system is given by the product of the single-site Fock states:

$$|\Psi_{MI}\rangle = \prod_i (\hat{a}_i^\dagger)^n |0\rangle, \tag{1.20}$$

$n \in \mathbb{N}$ being the homogeneous site filling.

While the particle number per site is perfectly determined, there is no phase correlation (no overlap) between the Wannier functions localized at each site. As a result, no macroscopic phase coherence holds.

The SF to MI phase transition with ultracold atoms was first observed by Greiner et al. [12] by increasing the lattice height s_1 (and thus the ratio U/J). The time-of-flight (TOF) fluorescence images of Fig. 1.8, show, for increasing

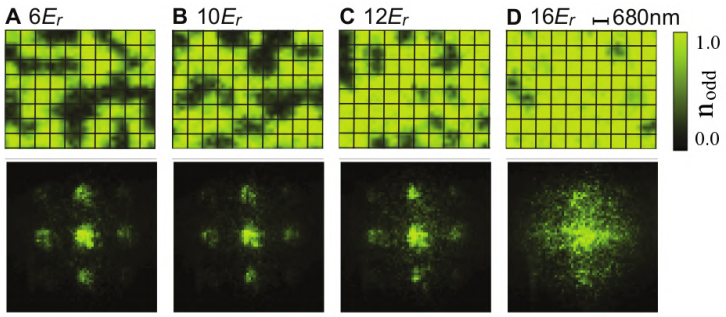

Figure 1.8: (**top row**) Single-site imaging of atom number fluctuations across the SF-MI phase transition. The in-situ fluorescence images are taken for increasing 2D-lattice heights from a region of 10 by 8 lattice sites within the $n = 1$ Mott shell that forms in a deep lattice. Sites occupied with odd or even atom numbers appear in the images respectively as full or empty sites. This is the case of the SF regime (**A** and **B**), whereas in the MI regime, fillings other than 1 are highly suppressed (**D**). (**bottom row**) Corresponding fluorescence images after free expansion of the cloud in the 2D optical lattice: the phase coherence is progressively lost moving from A to D. Figure adapted from [75].

depths of a 2D optical lattice, the progressive loss of phase coherence in

the momentum density distribution (bottom row). Simultaneously, the high resolution in-situ images (top row), show the progressive reduction of atom number fluctuations across the 2D optical lattice.

The phase diagram of Fig. 1.9 shows the boundaries between the SF and MI phases at $T = 0$, as a function of the ratios μ/U and J/U [16]. In the

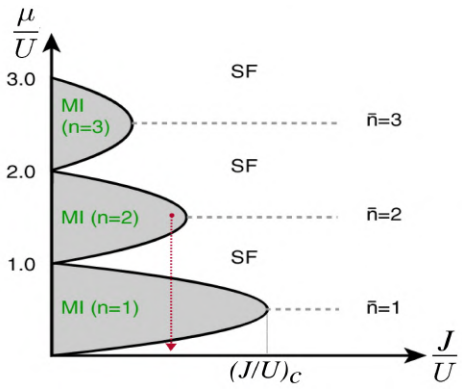

Figure 1.9: Phase diagram of the SF to MI transition in a homogeneous system as a function of the ratios μ/U and J/U. The MI lobes are characterized by a constant filling n and thus a vanishing compressibility K (corresponding to a discontinuous energy spectrum). In the SF phase the filling is defined only on average and, due to its gapless spectrum, the system is compressible. Note that the larger the average filling $\bar{n}$, the larger the interaction energy $(J/U)_c$ required to enter the corresponding MI domain. Red line: for a given J/U, decreasing the effective μ along the trap, MI domains alternate SF regions. Figure adapted from [16].

MI phase ($J/U \ll 1$), for a given value of the chemical potential μ[13], the site filling n is well defined (integer number). In particular, as the chemical potential μ increases, the site filling n discontinuously increases. In the SF phase ($J/U \gg 1$), instead, for a given μ, the site filling is defined only on average (poissonian number fluctuations). Note that for larger μ, and thus for larger site fillings n, the phase transition from MI to SF occurs at a smaller critical value $(J/U)_c$.

[13]The chemical potential μ, for a given temperature $T < T_c$, is a positive value depending only on the average particle density. As we shall see, in a trap, the role of μ will be played by an effective chemical potential μ_i taking into account the local system inhomogeneities.

Excitation spectrum and compressibility. So far we have compared the SF and MI phases referring only to the particle number fluctuations and the phase coherence properties. There are other two important features that characterize the two quantum phases, i.e. the excitation spectrum and the compressibility.

As it happens in solid state physics, the conductivity properties of the system are strictly related to its excitation spectrum: like the electrons in the metals, the atoms in the SF phase are capable to move from one site to another due to their *gapless energy spectrum*: when even a weak external force is applied to the system, the atoms start moving as they can be excited to states with energy very close to that of the original state by changing the momentum of some atoms by a small amount.

Conversely, in the MI phase where the atoms are not free to move, the energy spectrum is discontinuous with a gap of the order of U. In a homogeneous system, as sketched in Fig. 1.6, removing an atom from a site and adding it to a neighbouring one with the same filling, has an energy cost equal to the on-site interaction energy U (see also the phase diagram 1.9 in the limit $J \to 0$). Fig. 1.10 shows an experimental energy spectrum [76] with

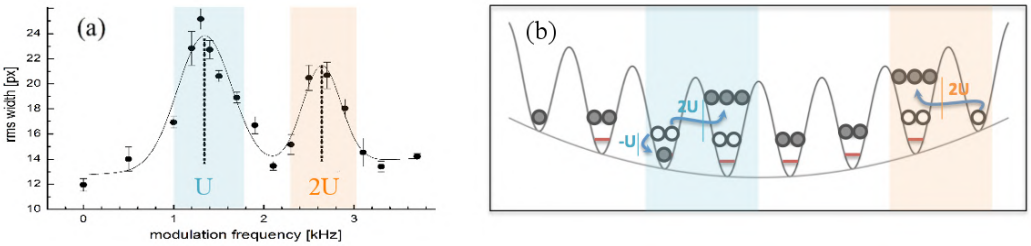

Figure 1.10: (**a**) Excitation spectrum for a MI, showing two peaks at the excitation energies U and $2\,U$. (**b**) Schematic of the excitations: the former peak corresponds to the hop of an atom to a site with the same filling (blue), the latter corresponds to the hop of an atom to a site with different site filling (pink), as it occurs at the boundary between two MI domains due to the inhomogeneity of the confined sample. Figure adapted from [76].

two peaks at the excitation energies U and $2\,U$. The former corresponding to the characteristic energy gap, the latter being due to the inhomogeneity

of the system.

As for the compressibility, it is a measure of the density change as a response to an energy change; formally

$$K = \frac{\partial n}{\partial \mu}. \tag{1.21}$$

The MI lobes of the phase diagram 1.9 are characterized by a constant site filling n and, consequently, a compressibility $K = 0$: a system in the MI phase is thus incompressible. This fact is a direct consequence of the discontinuous nature of the energy spectrum. The SF, whose energy spectrum is gapless, is instead compressible: a small change in the energy of the system results in a change in the average particle number per site.

In table 1.1 the features of the SF and MI phases are summarized.

Superfluid ($J \gg U$)	*Mott-insulator* ($U \gg J$)
Long-range phase coherence	No phase coherence
Poissonian number fluctuations	No number fluctuations
Gapless excitation spectrum	Gap in the excitation spectrum
Compressible	Not compressible

Table 1.1: Properties of the superfluid and Mott-insulator phases.

Inhomogeneous case. Let us now take into account the experimental case in which a local energy variation is always introduced by the presence of an external potential, due at least to the confining force exerted by the focused beams that form the optical lattices. The term $\sum_i \epsilon_i n_i$ in the DBH Hamiltonian 1.13 must thus not be neglected any longer. Due to the energy offsets ϵ_i, the system can be thought to be characterized by a local effective chemical potential $\mu_i = \mu - \epsilon_i$ slowly varying through the lattice; This quantity is strictly related to the system density such that an increase of μ_i causes an increase of the local filling. With reference to Fig. 1.11, for a harmonic trapping potential, μ_i and thus the density are maximum for the atoms at the center of the trap and progressively decrease moving towards

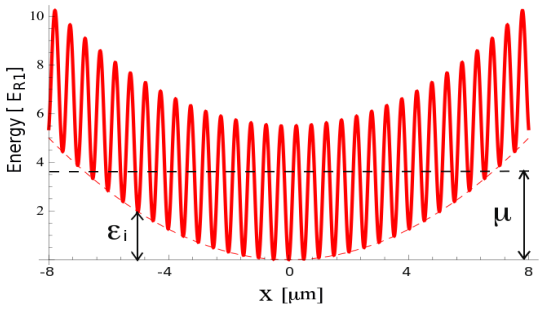

Figure 1.11: Optical lattice potential in the presence of a harmonic trap. The local effective chemical potential $\mu_i = \mu - \epsilon_i$, and thus the density, decreases moving from the lattice center to the edges.

the edges. According to the phase diagram of Fig. 1.9 (red dashed line), for a given value $J/U < (J/U)_c$, the atoms alternate different phases depending on their position across the trap: moving from the center of the trap towards

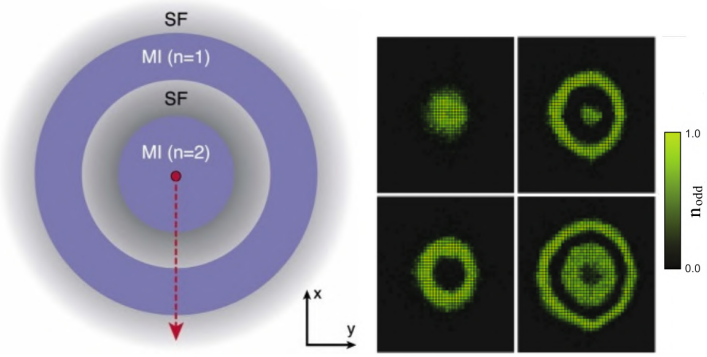

Figure 1.12: (**left**) Spatial distribution of the alternating MI and SF phases for a system confined in a 2D harmonic trap with $J/U < (J/U)_c$. (**right**) Single-site images of the MI shell structure ($J \to 0$) for increasing atom number. Full (empty) shells contain an even (odd) atom number per site. Figures adapted from [75, 77].

the edges, MI shells alternate to SF shells, the formers being characterized by a lower and lower filling (see Fig. 1.12 on the left). In the limit case of $J = 0$, only MI phases hold and the density profile has a step-like structure, also known as wedding cake or shell structure, with integer filling of all sites,

highest fillings being at the center of the trap. Fig. 1.12 (on the right) shows experimental images of the shell structure for increasing atom number [75].

1.2.2 Disordered system: Anderson localization

In this section we will take into account a non interacting system and we will see how its transport properties are affected by the presence of disorder. In particular we are interested in the phenomenon, first studied by P. A. Anderson more than 50 years ago [13], of localization of particles and waves in disordered media. Anderson studied the transport of electrons in crystals by using a single-particle tight-binding model with random on-site energies (see Fig. 1.13a): he showed that the transport, i.e. the diffusion of an initially localized wave-packet, is suppressed if the disorder amplitude Δ exceeds a critical value of the order of the tunneling energy J[14]. From another point of view (Fig. 1.13b), Anderson localization can be understood by considering the quantum-wave nature of particles. In this wave picture, the localization is determined by the destructive interference resulting from the several multiple scattering paths, which again prevents any diffusion.

In the following we will see how the original idea of Anderson can be developed to study the disorder-induced localization of a quantum wavefunction in a quasi-periodic optical lattice. It has been proven that this system shows a transition from extended to localized states analogous to the Anderson transition for a pure random disorder. The main difference is that with a quasi-periodic lattice such a transition at finite Δ occurs already in 1D [50, 80], whereas in the case of pure random disorder, 2D or 3D systems are required [81].

Let us consider a non interacting system ($U = 0$) in a 1D quasi-periodic optical lattice of the form 1.6. The DBH Hamiltonian 1.13 takes then the

[14]Due to the high electron-electron and electron-phonon interactions, the transition between extended and localized states studied by Anderson for non-interacting electrons has not been directly observed in crystals [45]. Nevertheless, owing to the importance and the general validity [78] of his discovery, in 1977 Anderson was awarded the Nobel Prize in Physics.

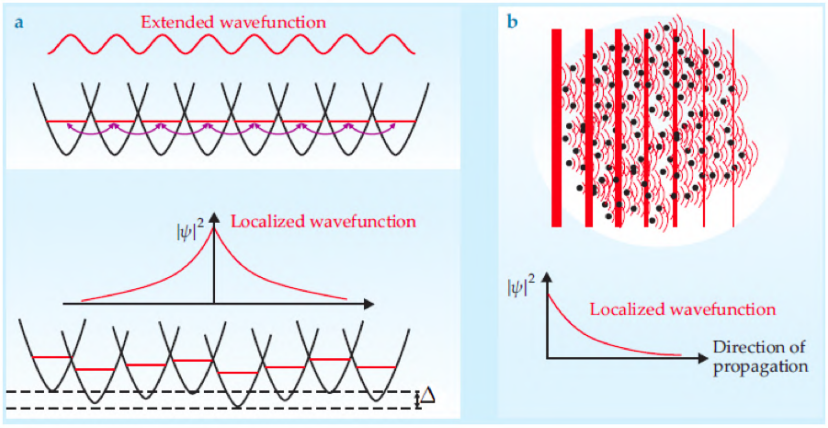

Figure 1.13: Schematic of Anderson localization from the twofold particle-wave point of view [79]. (**a**) Anderson localization in terms of tunneling of particles: in an ordered lattice (top) particles can tunnel between neighboring sites, freely propagating across the lattice with an extended wavefunction. If the regularity of the lattice is broken (bottom) by randomly changing the depth of the potential at each lattice site by an amount $\Delta \gtrsim J$, the tunneling is suppressed and particles localize with an exponential decaying wave-function. (**b**) Anderson localization in terms of destructive interference of waves propagating in a medium with large concentration of randomly distributed scatterers.

form (*Aubry-André Hamiltonian* [80])

$$\hat{H}_{AA} = -J \sum_{\langle i,j \rangle} \hat{a}_i^\dagger, \hat{a}_j + \sum_i \epsilon_i \, \hat{n}_i \qquad \text{with} \qquad \epsilon_i = \Delta \, cos(2\pi\beta \, i). \tag{1.22}$$

where the second term contains the quasi-periodic shift of the on-site energies due to the secondary lattice. $J \approx e^{-2\sqrt{s_1}}$ and $\Delta \simeq s_2 E_{r2} \, \beta^2/2$ are thus the two relevant energies which, as previously discussed, can be controlled independently by changing the heights s_1 and s_2 of the main and secondary lattice potentials, respectively.

As mentioned in Subsec. 1.1.2, when the ratio of the two lattice wavenumbers $\beta = \lambda_1/\lambda_2$ is an irrational number, the system displays features of a quasi-disorder system. If the disorder amplitude Δ is large enough, for the system is energetically convenient that the atoms are localized in correspondence of the energy minima forming an Anderson insulator (AI): an atom jumping from a site to a neighbour would result in an energy cost for the system of the order of Δ (see the second term of equation 1.22). In particular,

if the inverse of the golden ratio is used, $\beta = (\sqrt{5}-1)/2$, the model shows a "metal-insulator" phase transition from extended to localized states exactly at $\Delta/J = 2$ [80]. However, due to the limited degree of "irrationality" of our β, the experimental transition results broadened and shifted towards larger values of Δ.

Momentum distribution and diffusion. From the analysis of the momentum density distribution $\rho(k)$ we can get information on the eigenstates of the system. The width of $\rho(k)$ is inversely proportional to the spatial extent of the condensate in the lattice. In Fig. 1.14a we show the theoretical momentum distributions $\rho(k)$ for increasing values of Δ/J [82]. Without

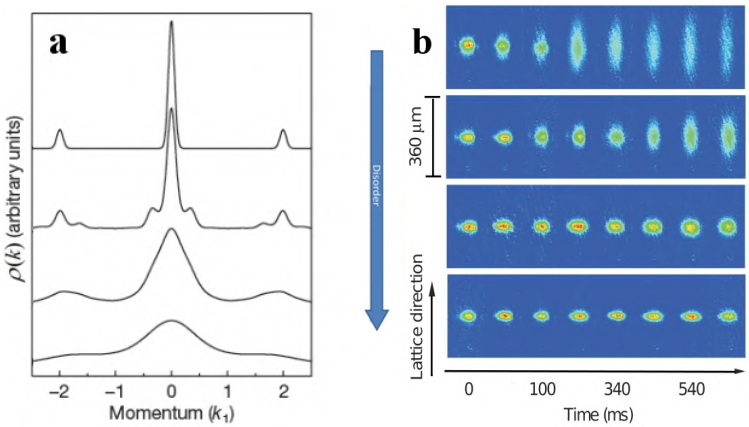

Figure 1.14: Broadening of momentum distribution and reduced diffusion for increasing disorder strength [82]. (**a**) Momentum distributions $\rho(k)$ for increasing Δ/J (0, 1.1, 7.2 and 25, from top to bottom). The interference pattern of a regular lattice observed at $\Delta = 0$ is at first modified by the appearance of peaks at the beating between the two lattices, and then increasingly broadened. Momentum is measured in units of $k_1 = \pi/d$. (**b**) In-situ absorption images of the BEC spatial distribution as a function of time and for increasing values of Δ. In absence of disorder the BEC expands ballistically, while for large disorder diffusion is completely suppressed.

disorder, the typical grating interference pattern can be observed, the three peaks at $k = 0, \pm 2k_1$ reflecting the periodicity of the primary lattice. The tiny width of the peak at $k = 0$ indicates that the wavefunction is spread over many lattice sites [83]. For weak disorder, the eigenstates of the Hamil-

tonian in equation 1.22 are still extended, and additional momentum peaks appear at momentum space distances $\pm 2(k_2 - k_1)$ from the main peaks, corresponding to the beating of the two lattices. As Δ/J further increases, $\rho(k)$ broadens and its width eventually becomes comparable with that of the Brillouin zone, $\pm k_1 = \pm \pi/d$, indicating that the extension of the localized states has decreased down to the order of the lattice spacing d.

As a comparison I also show in Fig. 1.14b an experimental observation [84] of the reduced diffusion induced by disorder. The measurements have been performed by suddenly switching off the main harmonic confinement and letting the atoms expand along the one-dimensional bichromatic lattice. In correspondence to the progressive broadening of the momentum distribution with Δ, the figure shows the progressive reduction of diffusion of the BEC in the quasi-periodic lattice: while in the regular lattice ($\Delta = 0$) the expansion along the lattice (vertical) direction is ballistic, increasing disorder the atoms expand with a progressively reduced velocity to the extent that no diffusion at all can be observed at large disorder.

1.2.3 Bose glass from weak to strong interactions

So far we have considered only the two limit cases of either null disorder or null interaction. The former case showing the SF-MI transition, the latter one showing the SF-AI transition. When both disorder and interaction are simultaneously taken into account, another quantum phase, the Bose glass (BG), is expected to appear [16, 17]. The characterization of the phase diagram showing the behaviour of the BG phase across the disorder-interaction plane (see Fig. 3.1) will be the subject of Chapter 3. Here I describe the main theoretical features focusing in particular on the BG properties in the two regimes of weak and strong interactions.

Weakly-interacting BG. Let us now see how introducing a weak repulsive interaction affects a disordered system. While disorder alone tends to localize non-interacting particles in the absolute lowest energy state, giving rise

to the just described phenomenon of Anderson localization (see Fig. 1.15a), weak repulsive interactions can counteract this effect drastically changing the features of the system [85]. In particular, a weak repulsion can "screen"

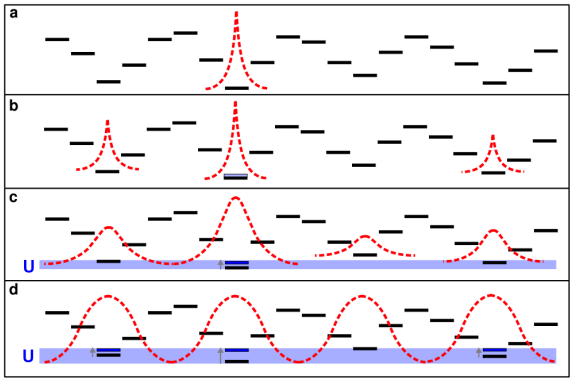

Figure 1.15: Schematic of the interaction-induced delocalization in a quasi-periodic optical lattice [85]. (**a**) AI ($U = 0$): for sufficiently large Δ the wavefunctions are exponentially localized and only the absolute lowest energy level is populated. (**b**) *Anderson glass*: with a very weak interaction several lowest energy levels are populated. (**c**) weakly-interacting BG: due to the repulsive interactions several lowest energy levels become almost degenerate and the corresponding wavefunctions are modified giving rise to locally coherent fragments, though long-range phase coherence is not yet restored. (**d**) BEC: for large interaction strengths the energy minima are degenerate and a coherent extended wavefunction is formed.

the disorder [86] and bring the system back to a coherent, extended SF (d), passing through an intermediate glassy phase (b,c). In the evolution from an AI to a SF we can think of two different stages:

- A very weak interaction pushes the bosons out of the lowest localized state, increasing the overall size of the system. The many-body states are however very close to the single-particle ones, and there is no coherence between distant or even neighbour states. This regime is often addressed as an Anderson (or Lifshitz) glass in literature [87–89].

- For larger interaction energies (of the order of a tenth of Δ), the energy minima – where most of the atoms are localized and thus the effect of the interaction is larger – start becoming degenerate and consequently

the many-body wavefunctions may occupy a few neighbouring sites. Here the system can locally be SF, but, globally, it is still an insulator. This regime is often addressed as weakly interacting BG glass [16, 90, 91] (or fragmented BEC [89]).

Strongly-interacting BG. Let us now describe the regime of strong interaction in the presence of disorder. Here we will focus our description on the transition that the system, with a given strong-interaction U, undergoes when the disorder amplitude Δ is gradually added. As discussed in Subsec. 1.2.1, when the system is homogeneous ($\epsilon_i = 0$), its properties are totally determined by the competition between the tunneling energy J and the interaction energy U (see Fig. 1.16a). In particular, in the limit of

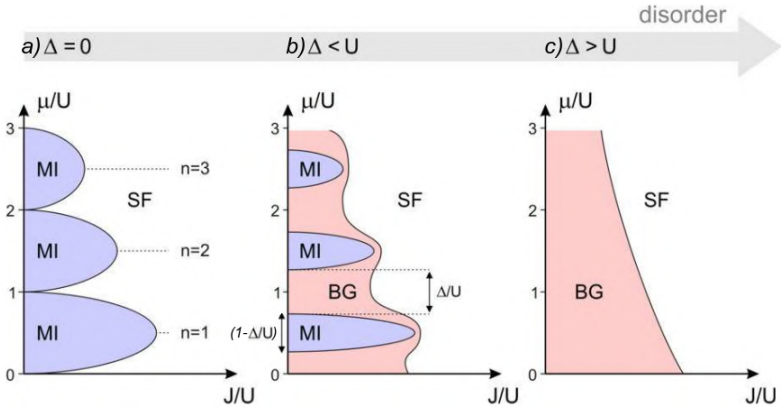

Figure 1.16: Phase diagram for a strongly-interacting disordered system as a function of the ratios μ/U and J/U [92]. Depending on the interplay between the energy scales J, U and Δ, three quantum phases can be identified: a superfluid (SF), a Mott-insulator (MI) or a Bose-glass (BG).

strong interactions ($U \gg J$), the system is characterized by MI domains, each of them with an integer site filling n determined by the local effective chemical potential. When a weak disorder $\Delta < U$ is added to the system (Fig. 1.16b), the MI lobes are expected [16] to shrink, their size being given by $\mu/U = 1 - \Delta/U$, and progressively make room to another quantum phase[15],

[15]Whether the strongly interacting BG is different or not from the BG at weak inter-

known as strongly-interacting BG phase. For larger disorders, when $\Delta \geq U$ (Fig. 1.16c), the MI lobes should completely disappear and, for a sufficiently small J, only the BG phase should hold.

Phenomenologically, the BG phase can be thought of as something in between a MI and a SF phase. Like a MI, the BG is insulating since it doesn't have long-range phase coherence. Like a SF, it has a gapless excitation spectrum (and consequently a finite compressibility), as I am going to show right away. It is important to note that the coexistence of these two properties, i.e. insulating and gapless excitation spectrum, is not in contradiction: despite the zero energy gap, excitations only occur locally giving rise to regions of local superfluidity with short-range phase coherence but, globally, the BG remains insulating. We also stress here that such features are in general typical of *glass*. As a matter of fact the quantum phase we previously referred to as Anderson glass or fragmented BEC in the weak-interaction regime is not different from the BG phase just described, in the sense that both are insulating and incompressible.

Gapless excitation spectrum. Let us now try to understand the gapless nature of the excitation spectrum in the BG phase. This will automatically explain why its compressibility, which has been defined in Eq. 1.21, is non zero. With reference to Fig. 1.17a we first consider the limit case of a homogeneous MI ($J \to 0, \Delta = 0$): as explained in Subsec. 1.2.1, the lowest excitation is $\Delta E = U$ corresponding to the energy cost of an atom jumping from one site to a neighbouring one with same filling (see also Fig. 1.10). Introducing disorder (Fig. 1.17b) yields random energy differences $\Delta_i \in [-\Delta, \Delta]$ between neighbouring sites. As a result, the energy cost due to an atom jumping from one site to a neighbouring one is now position dependent as $\Delta E_i = U \pm \Delta_i$. This means that in the full BG regime, when $\Delta \geq U$, an infinite-sized system can be excited at arbitrarily small energies as the energy gap approaches zero. We finally note that due to its finite size, a real system has an excita-

action is still an open question; see the discussion in Sec. 3.1.

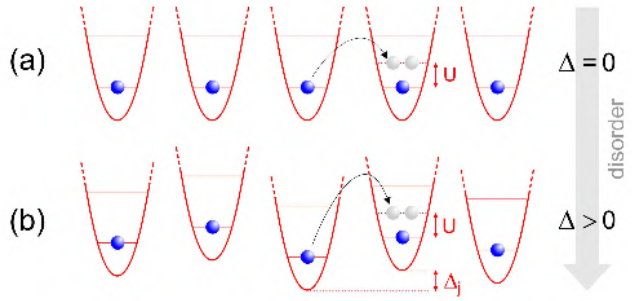

Figure 1.17: (**a**) In a homogeneous MI the energy cost for an atom jumping from one site to a neighbouring one with same filling is $\Delta E = U$. (**b**) If some disorder is introduced the energy cost for such a process becomes $\Delta E_i = U \pm \Delta_i$, Δ_i being the disordered-induced energy difference between neighbouring sites. Figure adapted from [92].

tion spectrum that, even though very small, has always a finite gap.

CHAPTER 2

CLEAN SYSTEM: THE SUPERFLUID PHASE

Contents

In this chapter we will consider a clean system, that is a system in the absence of disorder, focusing on the properties of a 1D SF. After describing the particular relationship between Bose-Einstein condensation and superfluidity in the more general 3D case (Sec. 2.1), we will see how the properties of a BEC, as well as of the SF, are affected by a reduced dimensionality (Sec. 2.2). In this section we will also describe the experimental procedure to create a

1D system and to investigate its coherence properties. In Sec. 2.3, we will then investigate the effects of the finite temperature on our experimental system by using theoretical methods. Such methods, in particular, will allow us to estimate the temperature of a 1D SF. Finally, in Sec. 2.4, we will report on several transport measurements showing the different mechanisms of dissipation of a SF in 1D, where the effect of strong phase fluctuations play a significant role.

2.1 BEC versus Superfluidity

One of the main reasons why much effort has been invested in the study of Bose-Einstein condensation is that this phenomenon is closely related to those of superfluidity and of superconductivity, the former being characterized by a frictionless flow of matter, the latter by a frictionless flow of charge. In this section we will focus on the phenomenon of superfluidity, attempting to describe at a basic level its subtle relationship to Bose-Einstein condensation.

The first system where the two phenomena have been investigated experimentally is liquid ^{4}He. Due to the light mass of its atoms, liquid helium exhibits strong quantum fluctuations which prevent it from becoming solid even at $T = 0$. As a matter of fact, except at high pressures (above 25 atm), helium is the only permanent liquid available in nature. As shown in Fig. 2.1, below the temperature $T_\lambda = 2.17$ K liquid helium (usually referred as to He I) becomes superfluid (He II). Remarkably, the experimental value of T_λ is close to the critical temperature $T_c = 3.1\,\mathrm{K}$ for Bose-Einstein condensation predicted for an ideal Bose gas at the same density[1]. This fact suggests the existence of a relationship between SF and BEC.

As a matter of fact, analogies between the two phenomena can be found both theoretically and experimentally. According to Landau's theory, if the excitation spectrum of the system satisfies certain criteria (which we shall see in Subsec. 2.4.1), the motion of the fluid does not cause any energy dissipation

[1]Note that due to the relatively high density, T_c for liquid helium is much higher than that for alkali atoms (of the order of tenths of nK), in agreement with Eq. 1.2.

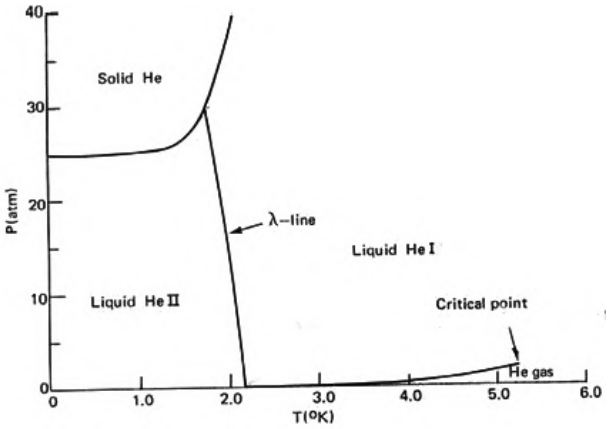

Figure 2.1: Pressure-temperature phase diagram of ^{4}He [93]. The λ line separates the normal (HeI) from the superfluid (HeII) phase of liquid helium.

[94]. These Landau criteria of superfluidity are met not only by the excitation spectrum of He II but also by the Bogoliubov excitation spectrum associated to an interacting BEC.

On the experimental side, using ultracold atoms it was possible to observe the remarkable transport properties of He II, like for instance the frictionless flow below a critical velocity [10], the second sound [95], the irrotational flow (and hence the reduced moment of inertia) [96] and the formation of vortices with quantized circulation [8, 9].

Despite these similarities, superfluidity and Bose-Einstein condensation are different phenomena. For instance, in an ideal Bose gas (thus in absence of interactions), 100 % of the particles can condense into the state with the lowest available energy, thus forming a BEC. However, as shown in Subsec. 2.4.1, an ideal Bose gas does not become SF. Conversely, in He II only about 7 % [97] of the atoms actually form a BEC, even though almost 100 % of the atoms can flow without friction. Let's consider the BEC wavefunction $\Psi = \sqrt{n_0}e^{-i\phi}$; this is connected to the SF velocity $\boldsymbol{v}_{SF}$ according to the well known relation [93]

$$\boldsymbol{v}_{SF}(\boldsymbol{r}) = \frac{\hbar}{m}\nabla\phi(\boldsymbol{r}). \tag{2.1}$$

The connection to the SF is thus only for the phase ϕ of the BEC wave-

function and not for its amplitude $\sqrt{n_0}$. As a matter of fact, the condensate density $n_0 = |\Psi|^2$ cannot be identified with the superfluid density n_{SF}. This fact, which is evident even at $T = 0$, is a consequence of the quantum depletion of the BEC, that is the fraction n_{QD} of atoms that are not in the single particle ground state at $T = 0$. Population of higher states occurs in the presence of interactions. As we saw, in a strongly interacting system as it is He II, this fraction can be even $n_{QD} \simeq 90\,\%$.

In other words, the main difference between BEC and superfluidity is that BEC is a property of the ground state, while superfluidity is a property of the excited states. This is entirely analogous to superconductivity, where the electrons condense into Cooper pairs (bosonic ground state), and where the interaction between the Cooper pairs introduces a finite energy gap between the ground state and excited states. In turn, this energy gap is responsible for the system becoming a superconductor. Thus, in both systems, it is the interaction between the particles that is responsible for the exotic behaviours, rather than the way they arrange themselves in the ground state.

In summary, we saw that even though a BEC and a SF are closely related one to the other, the presence of one phenomenon doesn't necessarily imply the presence of the other and vice versa. In the next section we will consider the case of 1D systems where even if we can not formally define a real BEC, the atomic sample indeed seems to behave as a SF. However, we already anticipate here that due to strong quantum fluctuations, the behaviour of 1D systems is quite subtle and not only the properties of a real BEC but actually also those of a SF are not completely preserved; as we shall discuss in Subsec. 2.4.3 a 1D SF is in fact always affected by the dissipation mechanism of phase slips.

2.2 1D quasi-condensate

In Sec. 1.1 we have seen that in 3D, decreasing the temperature below the critical value T_c, the size of the system wavefunction $\lambda_T \propto T^{-1/2}$ increases becoming comparable with the inter-particle mean distance d, i.e. $\lambda_T \gtrsim d$,

and a macroscopic fraction of the ideal Bose gas condenses in the lowest energy state. Correspondingly, the chemical potential μ, which is negative above the critical temperature, vanishes at T_c and remains essentially zero below. Conversely, in 1D (and also in 2D in a box) μ vanishes only at zero temperature, thus the critical temperature for Bose-Einstein condensation is $T_c = 0$ and no BEC can be formed at finite T [98]. In table 2.1 we report the conditions for the condensation critical temperature T_c in D dimensions, for both a box and a harmonic potential. Those results can be understood

D	box	harmonic
1	$T_c = 0$	$T_c = 0$
2	$T_c = 0$	$T_c > 0$
3	$T_c > 0$	$T_c > 0$

Table 2.1: Conditions for BEC critical temperature T_c in a box and in a harmonic potential as a function of the system dimension D.

considering the D-dependence of the density of states, which in the case, for example, of a box is $g(E) \propto E^{\frac{D}{2}-1}$. In a 3D gas, thus, $g(E)$ increases with E. Therefore, at sufficiently low T it becomes impossible to thermally occupy other than the lowest energy state. Conversely, in 1D (and 2D) the density of states does not increase with E and the phenomenon of BEC is absent.

2.2.1 Degeneracy temperature and correlation length

Even though in 1D it's not possible to define a critical temperature T_c below which there is a real BEC, it is always possible to define a *degeneracy temperature* T_D below which the quantum nature of particles cannot be neglected and the system is said to be a *quasi-condensate*. The degeneracy temperature

$$T_D = \frac{\hbar^2}{mk_B} n_{1D}^2 \tag{2.2}$$

satisfies the condition, analogous to that of Eq. 1.2 for the 3D case, that the 1D phase space density parameter $n_{1D}\lambda_T$ is of the order of unity. Here $n_{1D} = N/L$ is the 1D density, L being the length of the system[2].

[2]Note that in the presence of a lattice, its spacing is $d = L/N = n_{1D}^{-1}$.

Let us now analyze the features of a quasi-condensate in terms of the coherence properties of the system. Be $\rho(\boldsymbol{x}) = \langle \hat{\Psi}(\boldsymbol{x'})^\dagger \hat{\Psi}(\boldsymbol{x''}) \rangle$ the *correlation function* between two wavefunctions separated by a distance $\boldsymbol{x} = \boldsymbol{x'} - \boldsymbol{x''}$; according to [99] the condition for Bose-Einstein condensation is

$$\lim_{|\boldsymbol{x}|\to\infty} \rho(\boldsymbol{x}) = n_0 \tag{2.3}$$

that is the correlation function is finite even at infinite distances, n_0 being the density of atoms in the ground state. This is the case of a 3D BEC which is a macroscopic coherent object whose phase $\phi(\boldsymbol{x})$ is well defined throughout the system. In 1D this is not true any longer, as the strong phase fluctuations destroy the long range order of the system. As a matter of fact, the mean square fluctuations of the phase for 1D systems are expected [98] to diverge linearly at large distances $x = x' - x''$, that is

$$\langle \Delta\phi(x)^2 \rangle = \langle [\phi(x') - \phi(x'')]^2 \rangle = \frac{m k_B T}{n_{1D} \hbar^2} |x|. \tag{2.4}$$

As a consequence the correlation function in 1D decays exponentially, i.e.

$$\rho(x) \simeq n_{1D}\, e^{-\frac{\langle \Delta\phi(x)^2 \rangle}{2}} = n_{1D}\, e^{-\frac{|x|}{2\xi}} \tag{2.5}$$

with *correlation length*

$$\xi = \frac{n_{1D}\hbar^2}{m k_B} \frac{1}{T}. \tag{2.6}$$

The T-dependent length ξ represents thus the distance over which the system is coherent. As we shall see in the next section, this very important parameter is directly related to the momentum distribution width which is experimentally observable. According to the condition 2.3, in 1D there is no condensation as the correlation function approaches zero at large distances. Nevertheless, if the correlation length ξ is sufficiently large with respect to the system size L, then the phase coherence is preserved throughout the system, which thus behaves as a real condensate. We can then define the quasi-condensate as that system that exhibits intermediate properties between a real condensate and a normal system, in which $\rho(x)$ drops towards zero over a microscopic distance. In particular, by using the definitions 2.2 and 2.6 for

the correlation length and the degeneracy temperature, the conditions to be fulfilled for having a quasi-condensate are:

$$\frac{T}{T_D} = \frac{L/N}{\xi} < 1. \tag{2.7}$$

As we shall see in Sec. 2.3 this is the case of our experimental 1D system, where the correlation length is larger than the lattice spacing (which is exactly L/N for a filling $n = 1$) and the temperature is smaller than T_D. The

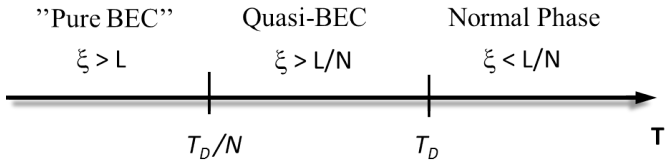

Figure 2.2: Phase diagram for 1D systems. For $\xi > L$ the system behaves as a pure BEC. Below T_D where $\xi > L/N$ the coherence properties are still preserved (quasi-BEC), while for shorter ξ the phase coherence is lost (normal phase).

conditions for the different regimes are summarized in the diagram of Fig. 2.2.

2.2.2 Momentum distribution and coherence

We now report on the investigation of the correlation properties of our experimental system. To directly determine the correlation function $\rho(x)$ we would need to have explicit knowledge of the in-trap density distribution which is usually not possible in the experiment (unless a setup with a high resolution, single-site imaging is provided). Nevertheless, the spatially averaged correlation function $g(x) = \int \rho(x', x + x')dx'$ can be easily related to the momentum distribution $\rho(p) = |\hat{\Psi}(p)|^2$ which, conversely, is accessible in the experiment. Using the Wiener-Khinchin theorem $\hat{\Psi}(p) \propto F[\hat{\Psi}(x)]$ we get

$$g(x) = F^{-1}[\rho(p)] \tag{2.8}$$

that is the correlation function is nothing else than the inverse Fourier transform of the momentum distribution $\rho(p)$. In the experiment, $\rho(p)$ is obtained performing time of flight (TOF) absorption imaging, that is by releasing

the atomic cloud from the trapping confinement and letting it free to expand before acquiring the image. If the expansion time is sufficiently large ($t_{TOF} \gg 1/\omega_i \ \ \forall i$) and the interactions can be neglected[3], the image reproduces the in-trap momentum distribution,

$$n_{TOF}(x) \approx \rho(p). \tag{2.9}$$

Since the correlation function $\rho(x)$ decays exponentially on the length scale ξ, its Fourier transform $\rho(p)$ is a Lorentian function

$$\rho(p) \propto \frac{1}{p^2 + \Gamma^2} \tag{2.10}$$

whose HWHM width Γ is inversely proportional to ξ:

$$\Gamma = \frac{0.63\hbar}{\xi}. \tag{2.11}$$

The TOF image of Fig. 2.3 shows a typical momentum distribution of the

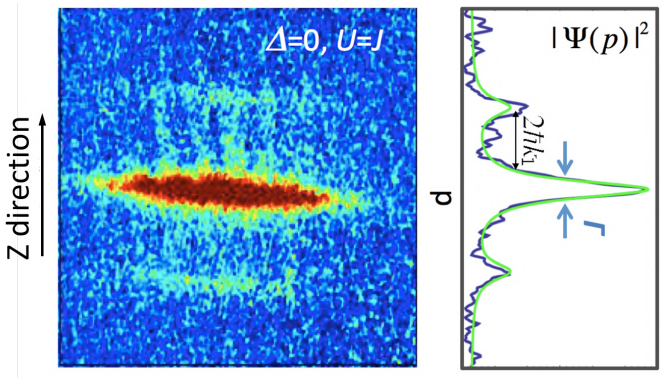

Figure 2.3: TOF image (**left**) of the momentum distribution $\rho(p)$ for a SF atomic sample in a lattice aligned along the $\hat{z}$ direction. The image is integrated along the horizontal direction (**right**) and fit with 3 Lorentian functions. The width Γ of the central peak gives information on the coherence properties of the system. Note the matter-wave interference fringes along $\hat{z}$ and the absence of phase coherence due to the potential tubes along the horizontal direction.

[3]Due to the strong radial confinement of 1D tubes, the fast expansion along the radial direction makes the system dilute after less than 1 ms, thus making negligible the effect of interaction along the axial direction. Moreover, in our case, the interaction is tuned to zero via the Feshbach resonance during the expansion.

sample and its intensity profile along the lattice direction $\hat{z}$ obtained integrating along the horizontal direction. A Lorentian fit with Eq. 2.10 provides the width Γ from which we determine the correlation length ξ of the system.

We note that the factor 0.63 in Eq. 2.11 takes into account the effect of the trap: the central region with larger density gives rise to a larger effective correlation length, i.e. $\xi/0.63$ [100]. As we shall see in Subsec. 2.3.1, also the effect of the optical lattice must be taken into account; when calculating the correlation length of Eq. 2.6, at least in a first approximation, one should replace the mass m with the reduced mass m^* for the atoms in the periodic potential.

2.2.3 Experimental procedure

In this subsection we describe the procedure used in our experiment to create a 1D system and to investigate its coherence properties. This will be useful to understand the various sources of loss of phase coherence in a SF sample, like for example an increase of temperature (next section) or an increase of interaction that can enhance dissipation mechanisms (Subsec. 2.4.2). This technique will result also very useful in the next chapter when the effect of disorder will be introduced to characterize the phase diagram of the momentum distribution as a function of both interaction and disorder. For simplicity, we describe already here also the experimental procedure used to tune disorder in the system.

Array of 1D potential tubes. As a starting point we consider a 3D interacting BEC of ^{39}K atoms prepared in an optical trap with mean frequency $\omega \simeq 2\pi\times 80\,\mathrm{Hz}$, at a scattering length $a = 210\,a_0$. In Fig. 2.4 we then report the temporal sequence employed to load the atoms in an array of 1D potential tubes at different interaction and disorder values. The 3D BEC is adiabatically transferred from the optical trap into the 1D potential tubes by ramping up a 2D strong optical lattice along the horizontal directions with a 400 ms s-shaped ramp. With a lattice depth $s_r = 30$ the radial trapping

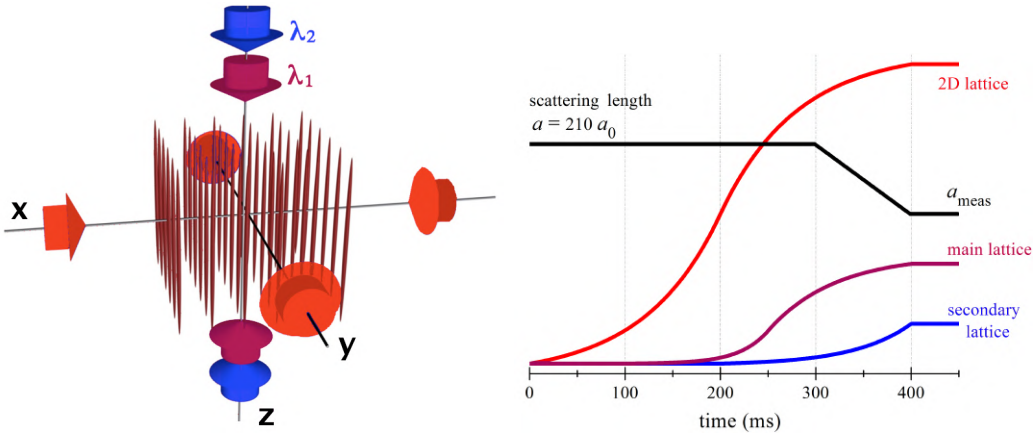

Figure 2.4: Optical lattice potentials (**a**) resulting from the loading temporal sequence (**b**). A 400 ms s-shaped ramp of a 2D strong optical lattice (red) with $s = 30$ forms an array of 1D potential tubes. The main (purple) and secondary (blue) lattices are subsequently raised up at different heights depending on the desired value of J and Δ respectively, while the scattering length (black) is linearly changed in the last 100 ms to get the desired value of U.

frequency of each tube $\omega_r \simeq 2\pi\times 50\,\text{kHz}$ is larger than all other energy scales and the tunneling between neighboring tubes is suppressed on the time scale $t_{exp} \sim 100\,\text{ms}$ of the experiments (i.e. $h/J_r \sim 1s \gg t_{exp}$). We can thus study the physics along the potential tubes, which can be effectively thought of as 1D systems (see Subsec. 1.1.3). Typically, out of a BEC sample of $N_{tot} \approx 30\,000$ atoms we get approximately 500 tubes with an average number of atoms $\bar{N} \approx 60$ each[4].

Inside the potential tubes. At later stages also the main and secondary lattices are adiabatically raised up, as shown in the figure. The depth s_1 of the main lattice, whose lattice spacing is $d = \lambda_1/2 = 532\,\text{nm}$, can be tuned according to the first of equations 1.17 in order to have the desired value of

[4]The atom number per tube can be determined by integrating the Thomas-Fermi profile of the interacting sample along the tubes. In the tube (i,j) the resulting number of atoms is $N_{i,j} = N_{0,0}[1 - \frac{2\pi N_{0,0}}{5N_{tot}}(i^2 + j^2)]^{3/2}$ where N_{tot} is the total atom number, $N_{0,0} = 5N_{tot}d^2/2\pi R_x R_y$ is the atom number in the central tube, $R_{x,y}$ are the Thomas-Fermi radii in the horizontal directions, which depend on the atomic scattering length a set by the Feshbach field, and $d = \lambda/2$ is the spacing of the tubes. For typical $N_{tot} = 3\times 10^4$ and $a = 210\,a_0$, we estimate an upper limit of $N_{0,0} = 96$, and an average $\bar{N} \approx 60$.

the tunneling energy J. Analogously, the depth s_2 of the secondary lattice (lattice spacing $d = \lambda_2/2 = 428\,\text{nm}$) can be tuned in order to have the desired value of disorder ($\Delta \propto s_2$). Finally, in the last 100 ms when the radial confinement is sufficiently strong to freeze the number of occupied tubes, the scattering length a is also tuned according to the second of equations 1.17 to have the desired value of the interaction energy U.

Momentum distribution detection. For a given set of parameters J, U and Δ, we can detect the coherence properties of the system by using the TOF imaging technique previously described. All the trapping potentials are thus suddenly switched off and the atoms let free to expand for 16 ms, after which the density distribution in coordinate space approaches the one in momentum space. As described in Subsec. 1.2.1 (Fig. 1.7), if before switching off the optical lattices the Wannier wavefunctions localized in each lattice site are phase-locked to each other, i.e. the system is a SF, then the Wannier functions interfere one with each other giving rise to sharp peaks in the density distribution along the direction of the free expansion. In particular, the distance between the peaks corresponds to the size of the Brillouin zone in the momentum distribution, that is $2\hbar\pi/d = 2\hbar k_1$, with $d = \lambda_1/2$ being the spacing of the optical lattice generated by the laser beam with wavelength λ_1. The image of momentum distribution of Fig. 2.3, taken at small interaction $U \simeq J$ (and in absence of disorder, $\Delta = 0$), shows the typical interference pattern of a coherent SF. Three horizontal stripes arising from the matter-wave interference along the tubes direction $\hat{z}$ can be easily distinguished. By contrast, the broad distribution along the other direction is a clear evidence of the absence of phase coherence between the wavefunctions belonging to different potential tubes.

As described in Subsec. 1.2.1, when the on-site interaction energy U is much larger than the tunneling energy J, the system enters the MI phase and the phase coherence is completely lost. Fig. 2.5 shows an absorption image of the momentum distribution in the MI regime taken at a large interaction

value, $U = 32\,J$.

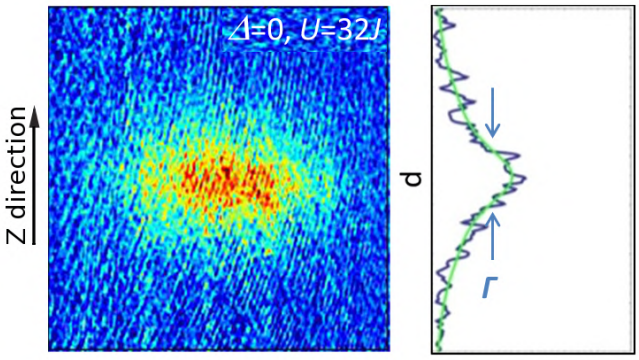

Figure 2.5: Absorption image of momentum distribution taken with interaction energy $U = 32\,J$ and representative of a MI sample. Note that the phase coherence is lost also along the $\hat{z}$ direction.

The large width Γ of the momentum distribution is a clear evidence of the loss of phase coherence of the sample; the correlation function decays according to Eq. 2.5 on a length scale ξ shorter than the lattice spacing d. As we shall see in Subsec. 2.4.2 this loss of phase coherence can be related to a complex mechanism of dissipation of the system, i.e. the interaction-enhanced phase fluctuations. We finally point out that, given a SF sample, a broadening of the momentum distribution analogous to that of Fig. 2.5, can be obtained also by increasing the temperature. As a matter of fact, the correlation length ξ can provide information also on the temperature of the sample and this will be the subject of the next section.

2.3 Comparison with theory: finite-T effects

In this section we make use of theoretical methods, like *density-matrix renormalization group* (DMRG) and *exact diagonalization* (ED), to investigate the effects of the finite temperature on our experimental system. This study has been performed in a collaboration with a theoretical group led by Prof. T. Giamarchi. The former method, in particular, will provide us information on the coherence properties of our inhomogeneous system at $T = 0$.

From a comparison with the theory we will thus get an insight on the loss of coherence induced by temperature in the experimental SF. The latter method will then allow us to estimate the temperature of the 1D SF.

We first study the inhomogeneous system described by the Bose-Hubbard Hamiltonian 1.13 using DMRG calculations at $T = 0$ [90, 101, 102]. Such calculations give access to the single-particle correlation function $g_{i,j}$ between the wavefunctions at sites i and j. Taking into account the trapping geometry and averaging over the distribution of tubes, the $T = 0$ momentum distribution for our inhomogeneous system can be obtained as

$$\rho(p) = |W(p)|^2 \sum_{lm} e^{ip(l-m)} g_{lm}, \tag{2.12}$$

which is analogous to Eq. 2.8, $W(p)$ being the Fourier transform of the Wannier function computed numerically.

To account for the finite temperature effects we thus compare the experimental $\rho(p)$ to that of the $T = 0$ theory. By looking at Fig. 2.6, we can immediately notice that the theoretical momentum distribution obtained by Eq. 2.12 (blue curve) is considerably narrower than the experimental one (black curve). In order to quantify the thermal broadening we phenomenologically introduce, in addition to the intrinsic ($T = 0$) correlation length ξ_0, a *thermal correlation length* ξ_T so that

$$\frac{1}{\xi} = \frac{1}{\xi_0} + \frac{1}{\xi_T} \tag{2.13}$$

and the exponential decay of the correlation function $g_{l,m}$ results multiplied by a factor $e^{-|i-j|/\xi_T}$ [103]. According to Eq. 2.8 this corresponds to convolve the theoretical Lorentian $\rho(p)$ of width Γ_0 with another Lorentzian distribution of width $1/\xi_T$. The convolution (red curve) of width $\Gamma = \Gamma_0 + 1/\xi_T$ is performed keeping ξ_T as a free fitting parameter in such a way that the theoretical and experimental distributions match best. For the sake of simplicity, one can assume the same ξ_T for all distances and all tubes.

As a first consideration we notice that there is a good agreement between theory and experiment. We then observe that the thermal correlation length,

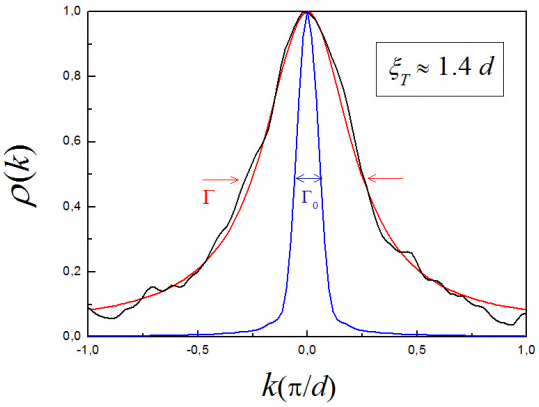

Figure 2.6: Comparison between the experimental momentum distribution $\rho(k)$ (black) and the one obtained with DMRG calculations for our inhomogeneous system at $T = 0$ (blue). The momentum p is here expressed in terms of the wavevector $k = p/\hbar$. The thermal correlation length ξ_T, which phenomenologically accounts for thermal effects, is obtained from the convolved momentum distribution (red) of width $\Gamma = \Gamma_0 + 1/\xi_T$ that best fit to the experimental one. For $U = 2\,J$, from a DMRG calculated $\xi_0 = 13.2\,d$ and a measured $\xi = 1.25\,d$ we get a thermal correlation length $\xi_T \simeq 1.4\,d$.

which gives a measure of the thermal effect on the system phase coherence, is rather short ($\xi_T \approx d$), showing thus a relevant impact of temperature on the SF. Despite this thermal broadening, the correlation length fulfils the condition 2.7 for the existence of a quasi-BEC. We finally point out that this phenomenological approach, which for the SF regime has already recognized being valid [103], can be actually used also in the presence of disorder, as we shall see in the next chapter. There we will see that for a strongly interacting BG, ξ_T is instead large.

2.3.1 Superfluid temperature

In this subsection we show a method to estimate the temperature of the 1D SF in the lattice. Eq. 2.6 provides a relation between the temperature and the correlation length ξ in the continuum, i.e. in the homogeneous case in the absence of the lattice. According to Ref. [100], the temperature in a

trapped system can be calculated as

$$T = \frac{\hbar^2 n}{0.63\, k_B m d}\,\Gamma \tag{2.14}$$

the factor 0.63 taking into account the larger effective correlation length in the trap. This equation provides an overestimation of the temperature since the width Γ takes into account, besides the thermal broadening $1/\xi_T$, also the intrinsic broadening Γ_0, which however can be subtracted according to Eq. 2.13 whenever the intrinsic correlation length ξ_0 is given (by DMRG calculations).

An extensive numerical study in the presence of the lattice is though a very difficult task. As a first, rough approximation, one can take into account the effect of the lattice by simply replacing the mass m with the zero-momentum reduced mass:

$$m^* = \frac{\hbar^2}{2Jd^2}. \tag{2.15}$$

The approximation becomes worse and worse as the lattice depth increases and one cannot even neglect any more the momentum-dependence of m^* as in 2.15. To get a more rigorous connection between the system temperature and the measurable correlation length we have therefore performed an exact diagonalization of the Bose-Hubbard Hamiltonian 1.18 for small homogeneous systems with length up to $L = 12\,d$. For a given interaction (and disorder) value we are able to calculate the temperature behaviour of the correlation functions $g_{i,j}$ and, by an exponential fit of their tails, of the correspondent correlation length $\xi(T)$. An estimation of the experimental temperature in the SF regime, can be thus achieved from a comparison between $\xi(T)$ and the thermal correlation length ξ_T measured as discussed in the previous subsection. As shown in Fig. 2.7, in the SF regime ($\Delta = 0$, $U = 2\,J$) we find a clear increase of $\xi(T)^{-1}$ for increasing T. At low temperatures, finite-size effects prevent us from obtaining quantitative results for $\xi(T)$, as it increases becoming comparable with the size of the system L. Nevertheless, we are able to determine the correct scaling of the inverse correlation length for

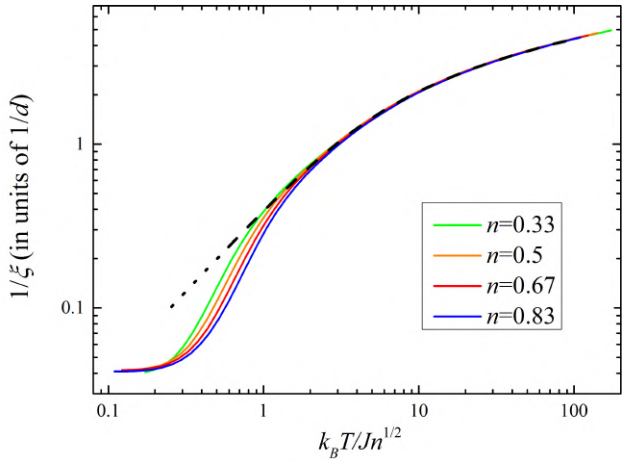

Figure 2.7: Inverse correlation length $1/\xi(T)$, calculated by exact diagonalization for a small homogeneous system with $L = 12\,d$ in the SF regime ($\Delta = 0$, $U = 2\,J$) and for various site fillings $n \leq 1$. The dashed line is a fit of the high-T numerical data with Eq. 2.16. Inset: density dependence of $1/\xi(T)$.

higher temperatures. As a matter of fact, in the range $k_BT = (2 - 100)\,J$, which is also the range of experimental interest, the numerical results are very well fit by the following relation

$$\xi(T) = \frac{d}{\operatorname{arcsinh}(\frac{k_BT}{\alpha J\sqrt{n}})} \tag{2.16}$$

with $\alpha = 2.50(5)$ being a fitting parameter. In such range of temperatures the plot shows that the intrinsic ($T = 0$) inverse correlation length is negligible ($\xi(0)^{-1} \ll \xi(T)^{-1}$) and in Eq. 2.13 we can thus identify $\xi(T)$ with ξ_T. From the thermal correlation length $\xi_T = 1.38(13)\,d$ obtained by the fit of the measurement performed at $U = 2\,J$ (and $\Delta = 0$) shown in Fig. 2.6, we obtain this way the experimental temperature for the SF[5],

$$k_BT = 3.1(4)(3)J. \tag{2.17}$$

Since the tunneling energy set by a lattice depth $s = 9$ is $J = h\times 110\,\mathrm{Hz}$, this corresponds to $T = 16\,\mathrm{nK}$. The experimental temperature is smaller than the

[5]the first uncertainty source is the statistical error on ξ_T and n, and the second one is the systematic error on the calibration of N_T ($\simeq 50\,\%$).

degeneracy temperature

$$k_B T_D = \frac{3}{16} N\hbar\omega_z^* \simeq 8J, \tag{2.18}$$

confirming thus the quantum nature of the system (quasi-BEC). Here the relation 2.2 given for the degeneracy temperature of an uniform gas has been replaced with that for a trapped gas [104], $\omega_z^* = \omega_z \sqrt{\frac{m}{m^*}}$ being the axial trapping frequency rescaled for the reduced mass $m^* \simeq 4\,m$ due to the optical lattice.

The results for $\xi(T)^{-1}$ shown in Fig. 2.7 refer to the case $U = 2\,J$, but other calculations in the SF regime, suggest little or no dependence on U. To our knowledge, this behaviour of $\xi(T)$ was not found in previous studies of bosonic systems. A similar result, $\xi(T) \simeq d/\mathrm{arcsinh}(k_B T/J)$, was however found for spinless fermions in a lattice [105], which represents the $U = \infty$ limit for a bosonic system.

For vanishing T, Eq.2.16 tends instead to the usual linear scaling in T^{-1} of the Luttinger liquid theory, $\xi(T) \simeq dJ/k_B T$ [103], which in turn is essentially Eq. 2.14. We note that the finite size of our simulations does not allow to study this low-T range, but the data in Fig.2.7 suggest that it is reached only for $k_B T \ll J$.

We finally point out that outside the SF regime, the study of $\xi(T)$ with the ED method just described is a very difficult task because in general there will be a coexistence of different phases, each one showing a different dependence on T. Moreover, even in the presence of a single phase one might expect a non-trivial dependence of the correlation length on all the parameters in the problem, i.e. $\xi = \xi(T, n, U, \Delta)$. Conversely, in the SF regime of small interactions, there is no dependence of ξ neither on Δ nor on U and the dependence on n is simply a scaling factor.

2.4 Measurements of dissipative mechanisms in a Superfluid

A SF is a system that by definition has the property to not dissipate energy. Nevertheless this strictly occurs only under certain conditions, which become more and more stringent in systems at lower dimensionality. After considering the Landau's criterion for superfluidity, experimentally focusing on the key role played by interaction (Subsec. 2.4.1), we will see how the strong fluctuations present in 1D systems can introduce important dissipation mechanisms. In particular, we will see that besides the known Landau velocity, there is another critical velocity v_c above which the system becomes (dynamically) unstable and the SF properties get lost (Subsec. 2.4.2). The dependence of the dynamical instability on the interaction will be considered as well: transport measurements will show how v_c decreases increasing U and approaches zero at the MI transition. Finally, in Subsec. 2.4.3, we will see that even at lower velocities and at zero temperature, 1D systems are actually always subject to small excitations, the phase slips, whose generation rate increases with velocity, having the dynamical instability as manifestation of their proliferation.

2.4.1 Landau instability

According to the Landau's criterion of superfluidity [93], a system can flow without friction if its velocity v is smaller than a finite *critical (Landau) velocity* given by[6]

$$v_L = \min_{\boldsymbol{p}} \frac{\epsilon(\boldsymbol{p})}{p} \tag{2.19}$$

where $\epsilon(\boldsymbol{p})$ is the dispersion law of the system. Conversely, for $v > v_L$ it is energetically convenient for the SF to create elementary excitations. This dissipative phenomenon is referred to as *energetic (Landau) instability*.

[6]The lowest velocity v_L at which a moving body can excite any of the states with energy $\epsilon(\boldsymbol{p})$ is a direct consequence of the energy and momentum conservation laws.

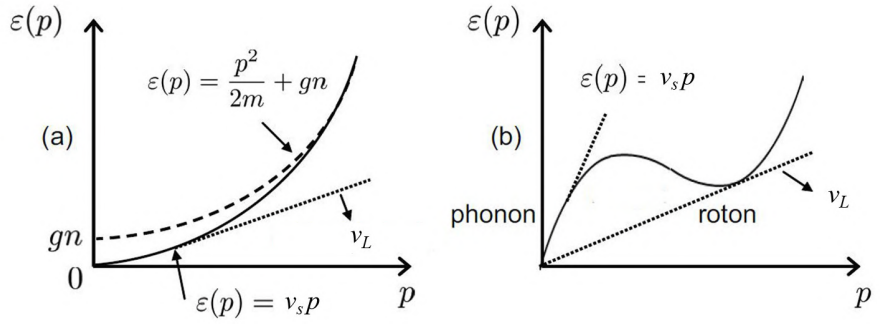

Figure 2.8: Excitation spectrum $\epsilon(p)$ of a weakly interacting BEC (**a**) and of He II (**b**). Both systems are SF as they exhibit a finite critical velocity satisfying Eq. 2.19. From the phonon-like part of the spectrum for the BEC we get $v_L = v_s$. Note that, despite He II is a strongly interacting system, it exhibits a smaller critical velocity ($v_L < v_s$) due to the rotonic structure of its spectrum. Figure adapted from [106].

Let's now recall the Bogoliubov dispersion law (see Fig. 2.8a) for the elementary excitations of a weakly interacting BEC, i.e.

$$\epsilon(p) = \sqrt{\frac{gn}{m}p^2 + \left(\frac{p^2}{2m}\right)^2} \tag{2.20}$$

where g is the interaction coupling parameter 1.3 and n is the density. For small momenta $p \ll v_s m$ the dispersion law takes the phonon-like form $\epsilon(p) = v_s p$ with

$$v_s = \sqrt{\frac{gn}{m}} \tag{2.21}$$

being the *sound velocity*. In the opposite limit $p \gg m v_s$ the dispersion law approaches the free particle law $\epsilon(p) \approx p^2/2m + gn$. We can easily see (Fig. 2.8a) that a weakly interacting BEC fulfils the Landau criterion 2.19 since there exists a non zero critical velocity, which in particular coincides with the sound velocity $v_s \propto \sqrt{g}$. As also discussed in Sec. 2.1, interactions play thus a crucial role for obtaining a non vanishing Landau velocity and thus a SF. As a matter of fact the Landau velocity decreases with decreasing interaction g and vanishes in the limit $g = 0$ of an ideal BEC ($\min \frac{\epsilon(p)}{p} = 0$ for $\epsilon(p) = p^2/2m$). Strongly interacting fluids such as liquid ^{4}He also fulfil the

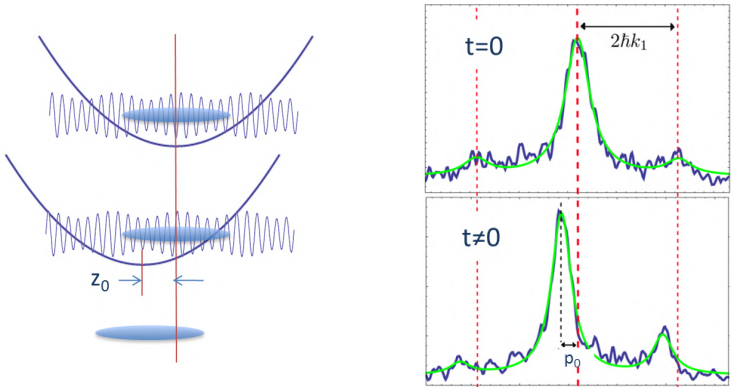

Figure 2.9: (**left**) Kick sequence. The center of the trap potential is shifted by the amount z_0. After the system evolution in the trap for a time t, all the optical potentials are switched off and the atoms freely expand for a time $t_{TOF} = 16\,\mathrm{ms}$. (**right**) Momentum distributions immediately after the kick ($t = 0$) and after an evolution time $t \simeq 1\,\mathrm{ms}$. The displacement of the quasi momentum p_0 at this given time is also shown.

Landau's criterion of superfluidity even though in this case the Landau velocity is smaller than v_s due to the complex phonon-roton excitation spectrum (Fig. 2.8b).

We experimentally investigated the Landau instability, and in particular the role of interaction for the existence of a SF, by performing transport measurements, that is studying the dynamics of a trapped 1D system after that an impulse has been imparted to it. The technique we employed, which mutatis mutandis will be useful also for other measurements (with and without disorder) presented in this thesis, is described in a general way in the following.

Transport measurement procedures. After creating a trapped quasi-condensate according to the loading procedure described in Subsec. 2.2.3, we observe the response of the system to an impulse ("kick") imparted by abruptly switching off the magnetic field gradient partially compensating for gravity. As shown in Fig. 2.9, the switching off of the field gradient induces a shift z_0 (a few μm) of the trapping potential, so that the atoms,

which are no longer in the potential minimum, start oscillating. We let the atoms evolve for a variable time t, after which all the optical potentials (trap and lattice) are switched off and TOF absorption images are recorded. As described in Subsec. 2.2.2, a TOF image approximately reproduces the in trap momentum distribution, i.e. $n_{TOF}(z) \approx \rho(p)$[7]. Fig. 2.9 also shows two examples of momentum distribution, one at $t = 0$, which we take as a reference ($p(0) = 0$), and one at the evolution time $t \simeq 1\,\text{ms}$, whose peak is displaced by the amount p_0.

Let us now analyse the dynamics of the atomic cloud in the trap and in the presence of the lattice. This can be modelled with the system of semi-classical motion equations:

$$\begin{cases} \dot{p} = -k_e z - \beta \dot{z} \\ \dot{p} = m^*(p)\ddot{z} \end{cases} \tag{2.22}$$

The first equation is that of a standard damped harmonic oscillator where the elastic constant k_e and the viscous friction coefficient β are respectively related to the axial trapping frequency $\omega_z = \sqrt{k_e/m}$ and the damping rate $G = \beta/2m$, the latter being the parameter of interest as it is a measure of the dissipation in the system. The second equation takes into account the effect of the lattice through the effective mass which is in general a function of p[8], i.e.

$$m^*(p) = \frac{\hbar^2}{2Jd^2}\frac{1}{cos(pd/\hbar)}. \tag{2.23}$$

In absence of any dissipation mechanism the atoms would oscillate with a frequency $\omega^* = \omega\sqrt{\frac{m}{m^*}}$. For a finite damping rate G, the position $p_0(t)$

[7]The atoms position $x_{TOF}(t)$ after the time of flight is actually related to the in-trap momentum $p(t)$ as $z_{TOF}(t) = z(t) + t_{TOF}\, p(t)/m + t_{TOF}^2 g/2$ where $z(t)$ and $p(t)$ are the in-trap position and momentum after the evolution time t. Therefore, the position in TOF at time t, with respect to that at time 0, is $z_{TOF}(t) - z_{TOF}(0) = z(t) + t_{TOF} p(t)/m$, having chosen $z(0) = 0$ and $p(0)$ as initial conditions. For t_{TOF} large enough, we can neglect the small contribution of the in-situ position ($z(t) \sim \mu$m), so that $[z_{TOF}(t) - z_{TOF}(0)] \propto p(t)$ and we can safely identify the measured $n_{TOF}(z)$ with $\rho(p)$.

[8]The dependence on p comes from the fact that $m^* = \left[\frac{\delta^2\epsilon(p)}{\delta p^2}\right]^{-1}$, with the dispersion law of the atoms in the lattice being $\epsilon(p) = \epsilon_0 - 2J\cos(pd/\hbar)$. We note that for a small lattice m^* can be assumed to be independent of p as it is in the free particle limit ($s \to 0$) where $\epsilon(p) = p^2/2m$ yields $m^* = m$.

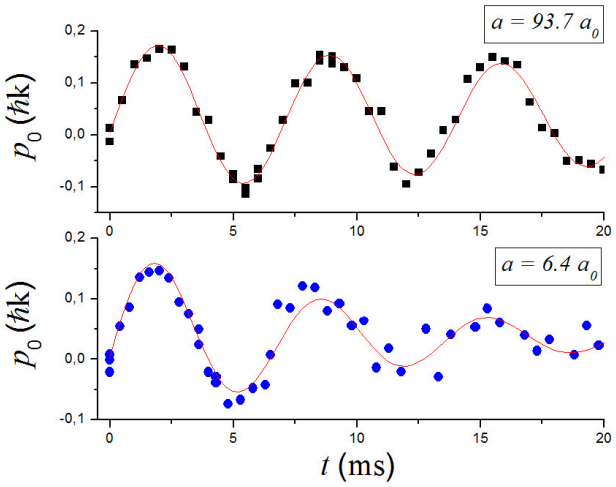

Figure 2.10: Damped oscillations in 1D systems for two interaction values, $a = 93.7\,a_0$ (**top**) and $a = 6.4\,a_0$ (**bottom**). The data (black points) are fit with Eq. 2.24 (red curve). At small interactions, where the sound velocity v_s is smaller, the oscillation is significantly more damped.

of the momentum distribution peak, can be approximated with a damped oscillation function

$$p_0(t) = p_{max} e^{-G^* t} sin(\omega' t) \tag{2.24}$$

with amplitude $p_{max} = m^* \omega^{*2} z_0 / \omega'$ and frequency $\omega' = \sqrt{\omega^{*2} - G^{*2}}$, with $G^* = G\,m/m^*$ being the lattice renormalized damping rate.

Transport measurements in absence of the lattice. To investigate the behaviour of our 1D quasi-BEC and the possible relation of its excitations to the Landau instability, we performed preliminary transport measurements in absence of the lattice [107]. In this case the equations of motion 2.22 can be solved analytically and the equation 2.24 for a damped oscillation is an exact solution. Fig. 2.10 shows, for two values of scattering length a, the momentum peak $p_0(t)$ obtained as previously described for different evolution times t in the trap. As expected, an oscillation in coordinate space reflects in an oscillation in momentum space and the data are well fit by equation 2.24. For large interaction ($a \approx 100\,a_0$), the oscillation is almost purely peri-

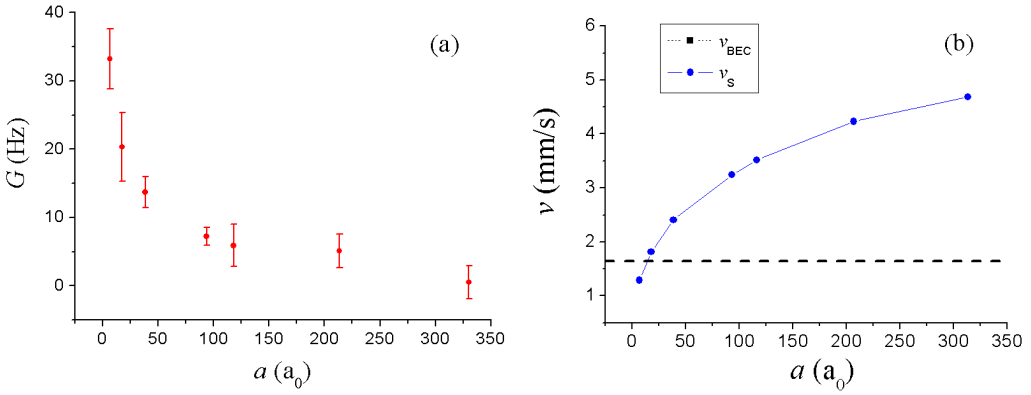

Figure 2.11: Damping rate G (**a**) and sound velocity (**b**) as a function of the scattering length a. The dashed line shows the BEC velocity $v_{BEC} = (1.64 \pm 0.16)$ mm/s, obtained from the average of the oscillation amplitudes. G is small for large a values where $v_{BEC} < v_s$. For small a values ($a \lesssim 20\, a_0$) where $v_{BEC} > v_s$, G increases as the Landau instability sets in.

odic, while for small interaction ($a \lesssim 10\, a_0$) it becomes significantly damped. Fig. 2.11a shows the damping rate G obtained from the fit as a function of a. Correspondingly to the quite sudden decrease of G, the sound velocity v_s (which increases with the interaction according to 2.21) becomes larger than the quasi-BEC velocity v_{BEC} (Fig. 2.11b). This fact indicates that the dissipation mechanism observed in our system for small interaction can be presumably related with the Landau instability[9].

Further measurements performed in higher dimensionality (not shown here) seem to confirm this result. They show that as the dimensionality D is increased, the damping rate G stops being significant at increasing values of a. This is a consequence of the interaction strength being smaller in 2D, and even smaller in 3D, for a given value of a.

[9] A more systematic study, for example as a function of the quasi-BEC velocity, would be useful to confirm this preliminary investigation. We cannot exclude a priori that the source of dissipation could be related to the presence of an impurity in the system, due for example to some imperfections in the optical lattices forming the 1D potential tubes or to the presence of some Rb atoms left in the sample even after the condensation of K.

2.4.2 Dynamical Instability

So far we have seen that in the absence of a lattice the system becomes energetically unstable when it moves faster than the sound velocity v_s. In the presence of a lattice, the system can be subject to another dissipation mechanism, the so called *dynamical instability*: a rapid growth of excitations breaks the phase coherence of the system as soon as its center of mass velocity v exceeds the critical velocity $v_c = \frac{\hbar}{md}\frac{\pi}{2}$. According to Eq. 2.1, such condition corresponds to the phase difference between adjacent sites becoming larger than $\pi/2$[10]. A naive interpretation of this mechanism is the following: when $v > \pi/2$, the tunnelling is not fast enough to lock the phases of adjacent sites, which start to run independently, and the system loses its long range coherence. As a matter of fact, entering this unstable regime we aspect to observe the following phenomena related to the *coherence* (a) and *transport* properties (b) of the system [108]:

a) The phases of adjacent sites become completely uncorrelated and the long range coherence of the SF state is rapidly lost. The lattice sites are still occupied by coherent states, but their phases start evolving independently. As a consequence, the interference peaks in the TOF expansion disappear.

b) Because of this effective dephasing among the lattice sites, the atomic current ceases to be driven by a coherent tunnelling process. The center-of-mass stops oscillating and the atomic sample stays blocked on a side of the harmonic potential. Tunnelling processes are still present, but their average effect on the center-of-mass motion is null: the system is thus an insulator.

Another simple interpretation of the dynamical instability can be given in terms of the effective mass m^*, which as already said takes into account the effect of the lattice. When $v > v_c$ the effective mass turns out to be

[10]For the sake of simplicity, from now on we will express the critical velocity and the correspondent critical momentum p_c in terms of phase differences, i.e. $v_c = p_c = \pi/2$.

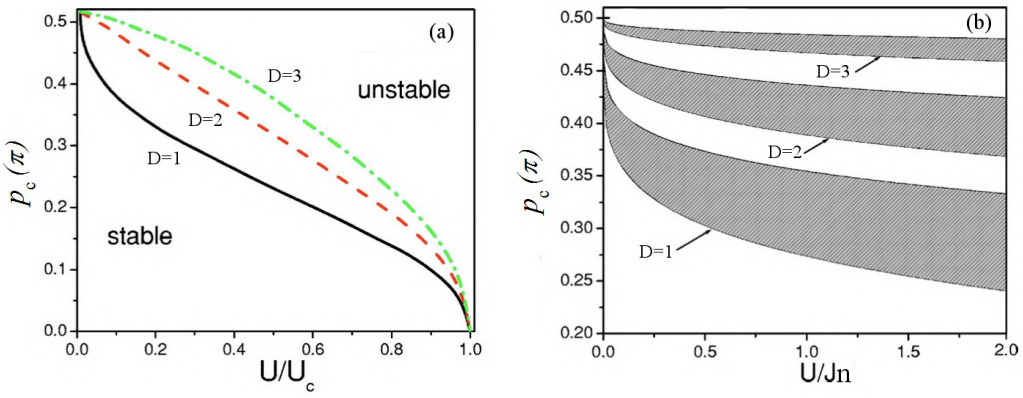

Figure 2.12: (**a**) Mean field phase diagram separating the SF (stable) regime from the dinamically unstable one, for different dimensionalities D [11]. The critical momentum at $U = 0$ is $p_c = \pi/2$ and decreases as U increases approaching zero at the SF to MI transition ($U = U_c$). (**b**) Effects of quantum fluctuations on the phase diagram. Increasing the ratio U/nJ the sharp classical transitions become broad crossovers (shaded regions) with a current decay intermediate between those in the stable and unstable regimes. Note that the strong broadening in 1D anticipates the SF to insulator transition to smaller critical momenta p_c.

$m^* < 0$ and correspondingly the BEC behaves as if it is subject to a negative scattering length [109]. Such attractive interaction brings the BEC to a sudden collapse [37–39].

So far we have assumed that interactions were small: the condition $v_c = \pi/2$ for the dynamical instability and the consequent transition from a SF to an insulator is in fact strictly valid in the limit $U = 0$. As described in Subsec. 1.2.1, as the interactions become large enough ($U \gtrsim J$) approaching a critical value U_c, the system undergoes the SF-MI transition, even for vanishing velocities. We thus expect that the critical velocity decreases as the interactions increase, approaching zero at $U = U_c$. Fig. 2.12a reports a mean-field-based phase diagram showing the critical momentum p_c as a function of U for different dimensionalities D [11, 110]. We point out that this result, which is obtained from a classical analysis, nicely works only when quantum effects can be neglected, thus only in 3D and/or at small interactions ($U \lesssim nJ$). Quantum fluctuations of the phase are in fact determined

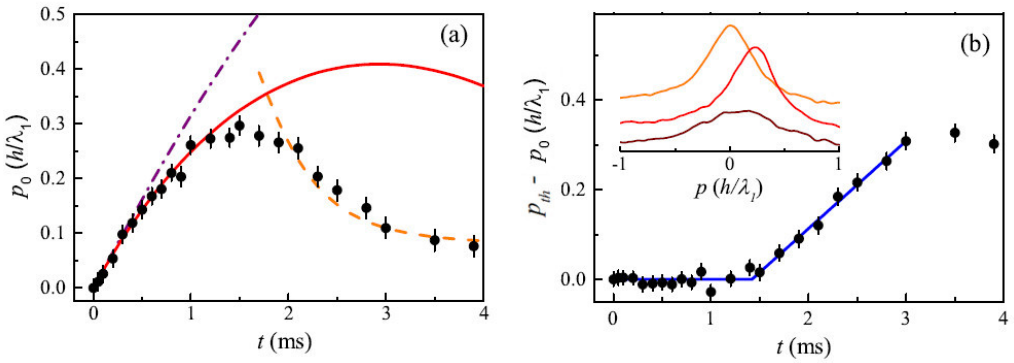

Figure 2.13: (**a**) Time evolution of the quasi momentum p_0 for $U = 1.26\,J$ and $n = 3.6$. The fit to the experimental data at short (red line) and long times (orange line) provide $G_{in} = 2\pi \times 135(10)$ Hz and $G_{fin} = 2\pi \times 600(50)$ Hz for the initial and final damping rates, respectively. The purple line is the expected oscillation in the absence of damping. (**b**) The dots show the difference between the fit to the initial damped motion p_{th} and the experimental data p_0. A piecewise fit (blue line) determines the critical momentum p_c. (**Inset**) Broadening of $\rho(p)$ during the time evolution: $t = 0$, $t = 0.8$ ms and $t = 3.5$ ms from top to bottom.

by the ratio U/nJ: as shown in Fig. 2.12b, increasing the interactions their effect becomes relevant and the sharp mean-field phase transitions become now crossovers, wider and wider as the dimensionality D is decreased. As a consequence, in our 1D system we expect to observe a SF to insulator transition as a function of U at lower critical momenta p_c with respect to that predicted by the classical mean field theory. This is what we are going to see right away. In the next subsection, in particular, we will relate this anticipated dynamical instability to the phase slips induced by the quantum (and thermal) fluctuations.

Transport measurements with a deep lattice [111]. We repeat the transport measurements previously described, in the presence now of the optical lattice. The lattice depth in recoil energies is $s = 8$. A typical time evolution of the quasi momentum p_0 at interaction energy $U = 1.26\,J$ and density $n = 3.6$ is shown in Fig. 2.13a. We observe interesting features in the dissipation of the system: after a weak damping at low momenta, there is a

rather sharp change of the system behaviour with a strong damping at large momenta, which corresponds to the occurrence of the dynamical instability. We fit the evolution of the quasi momentum p_0 with the damped oscillation function resulting from the solution of the equation system 2.22, leaving the damping rate G as a free fitting parameter. We identify two different regimes in the system dynamics. From the fit at short times (red curve), we find damping rates ranging as $G_{in} = 2\pi \times (20 - 300)\,\mathrm{Hz}$, depending on the interaction energy. At longer times, as p_0 increases towards the center of the Brillouin zone ($p = h/2\lambda_1$), a sudden increase of the damping stops the growth of p_0. The following decay of p_0 towards zero momentum is fit (orange curve) with a damping rate $G_{fin} \sim 1\,\mathrm{kHz}$. As expected, this change of behaviour is accompanied by an increase of the width of the momentum distribution $\rho(p)$. The inset of Fig. 2.13b shows the progressive broadening of $\rho(p)$ during the evolution (red and brown) with respect to the initial one (orange). In order to estimate the critical momentum p_c that separates the initial regime of weaker dissipation from the strongly unstable one, we plot the difference between the (red) fit of the initial oscillation and the experimental data (Fig. 2.13b): the interception of the two linear fits (piecewise fit) identifies the "breaking" time corresponding to p_c.

We performed similar dynamical measurements for different interaction energies U. A plot of p_c versus U is reported in Fig. 2.14. As expected by theory (Fig. 2.12a), the measured p_c features a clear decrease for increasing U, eventually approaching zero at the SF to MI transition. We note that even deep into the insulating regime, p_c doesn't vanish completely but stops at a finite value[11]. Such a finite value is probably due to that low density part of the system (outer potential tubes) that doesn't reach the localization condition $n = 1$ and keeps moving. From a piecewise fit of the data we get a critical value $U_c = 5.9(2)(4)\,J$ that is comparable with the theoretical one, $U_c = 2 \times 2.67\,J$ (for the calculated [114] mean filling $n = 2$). The uncertainties here are statistical and systematic, respectively.

[11] In the measurements reported in Ref. [112], the finite value of p_c was of the order of the inverse size of the system.

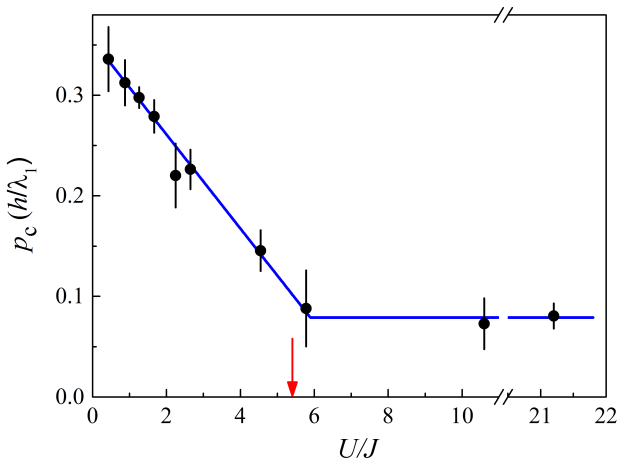

Figure 2.14: Critical momentum p_c as a function of the interaction energy U. A piecewise linear fit determines the critical value U_c for the SF-MI transition. The arrow marks the theoretical value for $n = 2$. Note that the p_c values are down-shifted with respect to those predicted for the non dissipative 3D systems.

To conclude, we stress that also in one dimension the onset of the Mott regime can be detected from a vanishing of the critical momentum p_c, as previously done in 3D systems [112]. In 1D the transport is however clearly dissipative (finite G_{in}) also for $p < p_c$, due to the presence of phase slips.

2.4.3 Phase slips

As already said, at $p = \pi/2$ a SF becomes dynamically unstable and undergoes a classical localization transition. For $p < \pi/2$ the system is instead stable provided that phase fluctuations are small. In 1D quantum and thermal fluctuations of the phase are strongly enhanced though. Such phase fluctuations generate phase slips which are responsible for the decay of the superfluid (as well as the superconducting) flow of the system also at small velocities (smaller than v_L and v_c). The reduction of the SF flow, in turns, causes the broadening of the mean field transition previously discussed and shown in Fig. 2.12.

With reference to Fig. 2.15 we now describe the phase slip process. At the phenomenological level a 1D superfuid can be described by a complex order

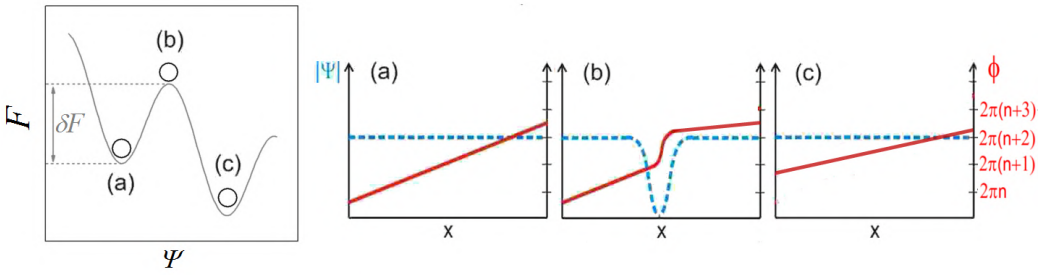

Figure 2.15: Phase slip process. (**left**) Landau free energy potential $F[\Psi]$: if thermal and quantum fluctuations are strong enough to overcome the energy barrier δF the system decays from the metastable state (a) to the metastable state (c). (**right**) Spatial variation of the amplitude of the order parameter $\Psi(x)$ (left axis, blue line) and phase ϕ (right axis, red line) before (**a**), during (**b**) and after (**c**) the phase slippage. After the whole process the phase gradient and thus the SF velocity $\boldsymbol{v}(x) \propto \nabla\phi(x)$ is reduced. Figure adapted from [113].

parameter $\Psi(x) = |\Psi(x)|e^{-i\phi}$. In this picture, a superfuid state corresponds to a local minimum of the Ginzburg-Landau free energy potential F, with F a functional of $|\Psi(x)|$ [115]. This state does not correspond to the absolute energy minimum, as the absolute minimum is characterized by no flow. Such a state is thus metastable and can decay towards another metastable state with lower energy (and lower velocity) if thermal and quantum fluctuations in the order parameter are strong enough to overcome the Ginzburg-Landau free energy barrier δF between the two metastable states. More in detail, such fluctuations cause deviations of both the modulus $|\Psi(x)|$ and the phase $|\phi(x)|$ of this order parameter from their equilibrium values. A non-trivial fluctuation corresponds to temporal suppression of $|\Psi(x)|$ down to zero in some point (e.g., $x = 0$) inside the lattice. As soon as the modulus of the order parameter $|\Psi(0)|$ vanishes, the phase $\phi(0)$ can jump by the value 2π. After this process the modulus $|\Psi(0)|$ gets restored and the phase gradient results reduced. In the whole process the SF velocity thus reduces, according to Eq. 2.1.

Let's discuss now the specific role played by thermal and quantum fluctuations in the phase slip process. As shown in Fig. 2.16, three different mechanisms may activate a phase slip, depending on the regime of temperature.

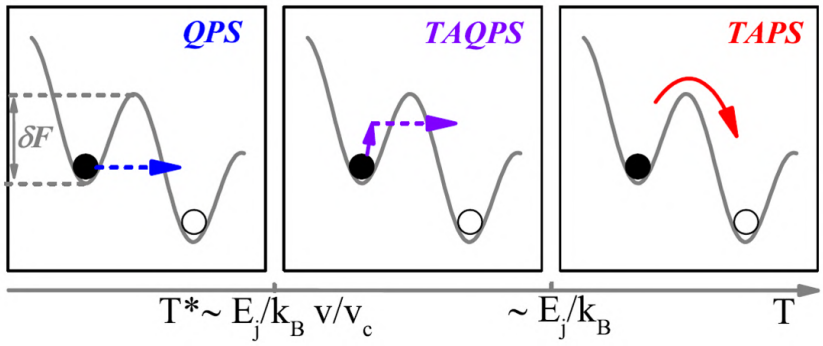

Figure 2.16: Sketch of the phase slips activating mechanisms as a function of temperature. Above the Josephson plasma temperature E_j/k_B, phase slips are classically activated by thermal fluctuations. Below the crossover temperature $T^* \sim E_j/k_B \times v/v_c$, phase slips are activated by pure quantum tunneling. For intermediate T both mechanisms occur. Note that T^* depends on v and via E_j also on γ.

When the temperature is higher than the free-energy barrier, $T \gg \delta F/k_B$, the order parameter may overcome δF via thermal fluctuations, causing thermal activated phase slips (TAPS) with a nucleation rate determined by the Arrhenius law as $\Gamma_T \propto e^{-\delta F/k_B T}$ [116, 117]. When $T < \delta F/k_B$, the probability of TAPS is small, and quantum phase slips occur mainly via quantum tunneling through the free-energy barrier [118]. Following standard quantum mechanical arguments one can find a characteristic temperature T^*, below which the QPS nucleation rate is temperature-independent, $\Gamma_Q \propto e^{-\delta F/\hbar\omega_0}$, with ω_0 an effective attempt frequency [119, 120]. In an intermediate range of temperatures, $T \gtrsim T^*$, QPS can be thermally assisted (TAQPS) [121], and the rate acquires a power-law dependence on temperature[12].

Besides the temperature, the nucleation rate Γ depends also on the velocity and in particular on the ratio v/v_c (or equivalently p/p_c) [121, 122]. In the following we will investigate the transport properties of the system in two regimes of velocities; this study will highlight the different contribution given by thermal and quantum processes in the phase slips, eventually allowing a

[12]The analytical expression of δF, ω_0 and T^* depend on the specific properties of the superfluid, including the type of obstacles that the superfluid experiences, e.g. disorder, periodic potentials or isolated defects.

characterization of the crossover between the QPS and the TAQPS regimes.

Transport at relatively large momenta [111]. Let us first analyse better the transport measurements previously described for the critical momentum p_c as a function of U. From the fit of the time evolution of the quasi momentum p_0 at momenta smaller than p_c, i.e. before the system breaks, we can determine the oscillation damping rate G_{in} (see Fig. 2.13), a quantity that is strictly related to the nucleation rate Γ. In this regime of relatively large, time-dependent momenta p, no theoretical models estimating Γ in terms of the damping rate are available though[13]. We then try to heuristically compare the experimental observations to the existing models valid for large velocities, for which the quantum and thermal nucleation rates are respectively [122]

$$\begin{cases} \Gamma_Q \propto e^{-7.1\sqrt{\frac{nJ}{U}}(\pi/2-p)^{5/2}} \\ \Gamma_T \propto e^{-\frac{4nJ}{3k_BT}(\pi/2-p)^3} \end{cases} \qquad (p \to \pi/2) \tag{2.25}$$

As a first thing we note that both the nucleation rates exponentially increase while approaching $p_c = \pi/2$, where the system becomes dynamical unstable. We then note that the theoretical crossover temperature[14] for our experimental parameters is in the range $k_BT^* = (1.5 - 3.5)\,J$, hence of the same order as the estimated experimental temperature, $T \simeq 3\,J$. This suggests a possible coexistence of quantum and thermal phase slips. To understand whether there is a more significant contribution of one or the other mechanism, we phenomenologically employed the models 2.25 to estimate the critical momentum p_c to enter the strongly dissipative regime at different U, i.e. $p_c(U)$, imposing an arbitrary cut-off for Γ_Q and Γ_T (corresponding to our constant $G_{fin}/2\pi \approx 1$ kHz in the experiment). In the calculations we used the parameters as in the experiment, $T = 3\,J$, and we introduced an arbitrary constant to phenomenologically adapt the phase-slip nucleation rate Γ_Q (and Γ_T) to

[13] As we shall see later on, in the opposite limit $p \to 0$, G_{in} is related to Γ by $G_{in} \propto \Gamma/p$.

[14] The crossover temperature (in units of k_B) is of the order of the plasma Josephson energy, which in the tight binding model is given by $E_j \simeq \sqrt{nJU}$.

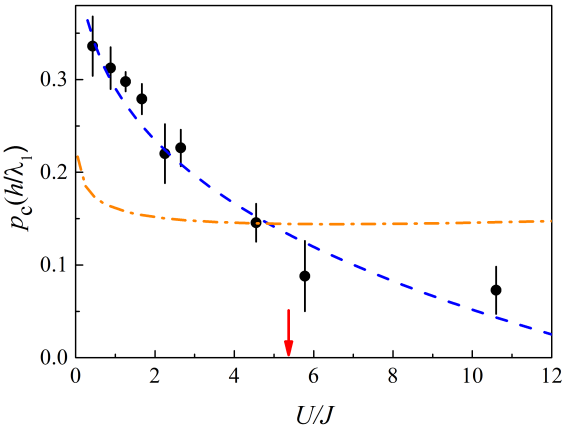

Figure 2.17: Critical momentum p_c as a function of the interaction energy U. The experimental data (dots) are compared with the phenomenological models for the phase-slip nucleation rates in the quantum (blue line) and thermal (orange line) regimes.

the damping rate. Such constant has been chosen to reproduce the observed p_c at $U = 4.5\,J$. The experimental data and the two phenomenological predictions of $p_c(U)$ obtained with the two models are shown in Fig. 2.17. While the quantum phase-slip rate can capture the observed evolution of $p_c(U)$, the thermal rate has only a weak dependence on U at constant temperature, thus suggesting a more relevant role of the quantum mechanism.

Transport at relative small velocities [123]. We now report on transport measurements that provide the first experimental evidence of quantum phase slips in 1D atomic superfluids. Here we explore the regime of relative low velocities and of intermediate interactions, far from the SF-insulator transition where the phase slip rates tend to diverge exponentially. In such a regime of small v, the theory [121] predicts that the QPS and the TAQPS nucleation rates scale respectively as

$$\begin{cases} \Gamma_Q \sim v^{\alpha(\gamma)} \\ \Gamma_{TQ} \sim vT^{\beta(\gamma)} \end{cases} \quad (v \to 0) \tag{2.26}$$

where $\alpha(\gamma)$ and $\beta(\gamma)$ are parameters that decrease as the interaction γ of Eq. 1.10 increases [121] and that depend on the specific properties of the

SF[15]. Moreover, the theory shows that the crossover from TAPS to QPS occurs at the temperature (see Fig. 2.16):

$$T^* \simeq E_j/k_B \times v/v_c, \tag{2.27}$$

where $E_j = \hbar v_s/\sqrt{2}d$ is the Josephson plasma energy [124], which increases with the interaction γ via the sound velocity v_s. In the following we summarize the main steps of the work:

a) By using the technique described in Subsec. 2.4.1, we measure the damping rate G of the SF oscillating in a harmonic potential in the presence of a weak[16] optical lattice ($s = 1$), for a wide range of velocities (below v_c and v_s) and interactions.

b) We relate the measured damping rate G to the theoretical phase slip nucleation rates 2.26 using the simple relation[17] [122]

$$G \propto \Gamma/v \tag{2.28}$$

c) We observe a change of behaviour in G with increasing interaction and velocity that is consistent with the crossover from the TAQPS to the QPS regime.

In order to study the dynamics of the system at different velocities, we suddenly shift the center of the harmonic trap by a tunable amount. Like in the other experiments, the kick to the system is imparted by switching off

[15]Depending on the type of obstacles that the SF experiences, the α parameter changes: in terms of the Luttinger parameter K, α is simply: $2K-3$ in the case of disorder, $2K-2$ in the case of a periodic potential and $2K-1$ in the case of a defect. K is related to the Lieb-Liniger parameter γ according to the relation $K^{-1} = \sqrt{\gamma}/\pi\sqrt{1-\sqrt{\gamma}/2\pi}$.

[16]Working with a small lattice depth s has the advantage to increase the critical velocity v_c, which is proportional to the tunneling rate J between adjacent sites [108]. Therefore this choice, on one side allows to satisfy the stability condition $v < v_c$. On the other side, it doesn't allow a quantitative comparison with equations 2.26, which are derived in the tight-binding regime ($s > 5$).

[17]In our case of underdamped regime ($G \ll \omega_z$), relation 2.28 can be simply derived as follows: the peak acceleration is $dv/dt = -Gv$, which in terms of phase slips can be written as $\delta v/\delta t$, where $\delta t^{-1} = \Gamma$ and $\delta v = -h/mL$ is the velocity variation following an individual phase slip of 2π in a chain of length L.

the magnetic field gradient compensating the gravity; the momentum distribution $\rho(p)$ is then recorded via TOF imaging. By fitting $\rho(p)$ with a Lorentzian function, we get the quasi momentum p_0 and the distribution half-width-half-maximum δp, which is related to the mean temperature via $T = \frac{\hbar n}{0.63\, m^* k_B d}\, \delta p$ (see Eq. 2.14). Fig. 2.18 shows a typical time evolution

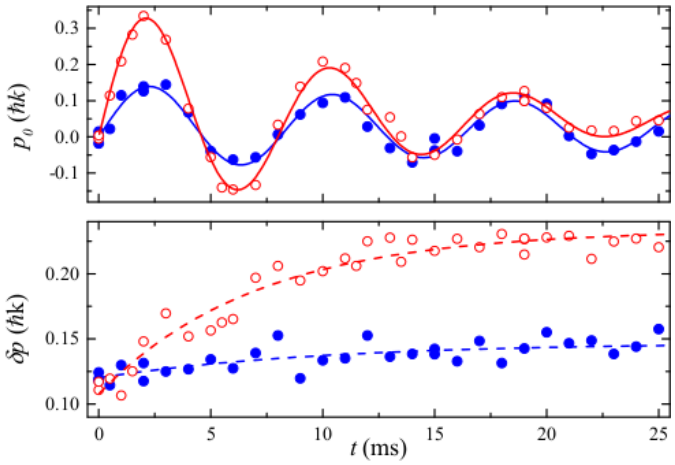

Figure 2.18: Damped oscillations in an optical lattice with depth $s = 1$. The time evolutions of the quasi momentum p_0 (**top**) and of the momentum width δp (**bottom**) are shown for two different velocities at the interaction $\gamma \simeq 1.2$. At small velocity, $v = 1.4(4)$ mm/s (blue), the damping is almost null and δp remains quite constant. At larger velocity, $v = 2.2(4)$ mm/s (red), both the damping and δp increase significantly. The continuous and dashed lines are fits to determine the damping rate G and the time constant τ respectively.

of p_0 and δp at a given interaction energy ($\gamma \simeq 1.2$) and at two different trap shifts, corresponding to two different velocities. We fit the time evolution of p_0 according to Eq. 2.24 for an oscillator with a friction term: $p_0(t) = m^* v_{max} \exp(-Gt) \sin(\sqrt{\omega^{*2} - G^2}t)$, where v_{max} is the maximum of the oscillation (occurring at a quarter of a period, $t = \pi/2\sqrt{\omega^{*2} - G^2}$) in absence of damping ($G = 0$). The growth of δp is fit with the exponential function $\delta p(t) = \delta p(0) + p_\infty[1 - \exp(-t/\tau)]$, p_∞ being the relative saturation value. We find that the damping rate G is directly related to the constant time τ, as $2\tau \simeq 1/G$. This relation can be interpreted considering that the mechanical energy dissipated in the oscillation is converted into momentum spread. We differentiate each measurement according to

its (maximum) velocity $v = v_{max}\exp(-\pi G/2\sqrt{\omega^{*2} - G^2})$, that is the first maximum of the damped oscillation. As shown in Fig. 2.18, at small velocity ($v = 1.4(4)\,\mathrm{mm/s}$) the oscillation persists with very small damping ($G = 28(9)\,\mathrm{Hz}$) and δp remains substantially constant during the 25 ms of the measurement. At larger velocity ($v = 2.2(4)\,\mathrm{mm/s}$) we observe a much stronger damping ($G = 84(6)\,\mathrm{Hz}$), indicating a dependence of the phase-slip rate on the velocity. We note that at this interaction energy the velocity is lower than the critical velocity $v_c = 5.4(6)\,\mathrm{mm/s}$ and than the sound velocity $v_s = 3.5(2)\,\mathrm{mm/s}$, suggesting thus that other dissipation mechanisms are negligible.

We repeated this type of measurement in a wide range of velocities and interaction strengths, and also for different temperatures in the accessible experimental range (from 20 to 40 nK). A summary of the behaviour of G with velocity and interaction for $T = 37(7)\,\mathrm{nK}$ is shown in Fig. 2.19a. Here

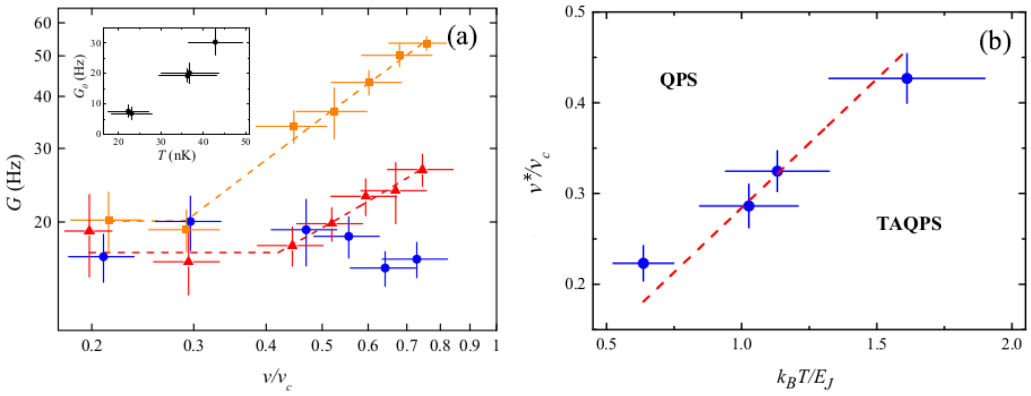

Figure 2.19: (**a**) Damping rate G as a function of the velocity v normalized to the critical velocity v_c, for three interaction energies: $\gamma \simeq 0.13$ (blue circles), $\gamma \simeq 0.19$ (red triangles) and $\gamma \simeq 0.64$ (orange squares). Each data set is fit with a piecewise function (dashed lines) for extracting the QPS-TAPS crossover velocity v^*. (**Inset**) G versus T at small velocities ($v < v^*$) for a given interaction energy ($\gamma \simeq 0.64$). (**b**) Velocity-temperature diagram for the QPS-TAPS crossover. The crossover velocities v^* (dots) are linearly fit (dashed line) to determine the crossover temperature T^*.

v is expressed in units of v_c and each data set corresponds to a different γ[18].

[18]The critical velocity for the dynamical instability, measured as described in Subsec. 2.4.2, decreases with increasing γ (as expected) from 7.1(3) to 5.4(6) mm/s.

At weak interaction (blue), G is essentially independent of v. At stronger interactions (red, orange), we observe instead a clear crossover from a regime of constant G to a regime where G grows with the velocity as a power law. By fitting each set of measurements with a piece-wise power law function, we extract the minimum velocity v^* required to enter the power-law regime. The crossover velocity v^* apparently decreases for increasing interaction. Other data at a different temperature (not reported) show a similar behaviour. In the v-independent regime of G we observe a clear dependence of G on the temperature (inset), while interaction effects result to be dominant in the v-dependent regime.

According to equations 2.26 for the nucleation rates Γ_Q and Γ_{TQ} and to their relation with G ($\Gamma \propto vG$), all these observations are consistent with crossing the TAQPS-QPS transition by tuning velocity and interaction. Our measurements are actually performed with T approximately constant, while T^* is tuned according to Eq. 2.27 by changing v and E_j[19]. For $T^* < T$, i.e. at small velocity and small interaction, the system is apparently in the TAQPS regime of no dependence on v and of power-law dependence on T. For $T^* > T$, i.e. at large velocity and large interaction, the system enters the QPS regime of power-law dependence[20] of G on the velocity.

Let us now show a more quantitative study to characterize the TAQPS-QPS crossover described by Eq. 2.27. In Fig. 2.19b we plot the extracted crossover velocity normalized to the critical one, v^*/v_c, versus the temperature normalized to the Josephson energy, k_BT/E_j. In our accessible range of parameters the data show a clear linear scaling as in Eq. 2.27. From a linear fit we get

$$k_BT^* = 4.8(4)E_jv/v_c - 0.41(10)E_j. \tag{2.29}$$

[19]In our range of interaction strengths $\gamma = 0.13-1.2$, the Josephson plasma temperature E_j/k_B increases with γ ranging from 20 to 35 nK, thus is of the same order of magnitude of the experimental T.

[20]We note that the exponents of the power-law behaviour we measure for $v > v*$ are of the order of unity, therefore quite different from the exponent $2K - 1$ predicted by the theory [122], which ranges from 4.5 to 13 for our interaction parameters. This disagreement might be due to the fact that the theoretical results have been obtained for a strong lattice in the tight binding regime and for very small momenta, $p < hk/6$.

The observed linear behaviour, together with the measured prefactor of order unity, are a clear confirmation that what we observe is indeed a TAQPS-QPS crossover driven by velocity and interaction.

We finally note that these results give a further confirmation that the large damping rate observed in the experiment performed at relatively large v described before is actually due to quantum phase slips. There, the Josephson plasma energy and the temperatures are respectively $E_j/k_B \simeq 20\,\mathrm{nK}$ and $T \simeq 20\,\mathrm{nK}$ [125]; according to 2.29, this implies that $T < T*$ at $v \simeq v_c$, suggesting that the main contribution to the dissipation is due to quantum (rather than thermal) phase slips.

In conclusion we can state that the dynamical instability occurring in 1D systems with strong phase fluctuations can be thought of as a particular case of the phase slip dissipative mechanism. As a matter of fact, the quantum phase slip nucleation rate diverges in the limit of large velocities, $v \to v_c$, resulting in an instability of the system.

CHAPTER 3

DISORDERED SYSTEM: THE BOSE GLASS PHASE

Contents

In the first chapter (Sec. 1.2) we described the different quantum phases that an interacting bosonic system in the presence of disorder can be subject to. In this chapter we will characterize from an experimental point of view the phase diagram describing such a system as a function of the disorder strength Δ and the interaction energy U. In Sec. 3.1, after showing a few $\Delta - U$ theoretical phase diagrams at $T = 0$, we will report the experimental one obtained by coherence and transport measurements. Theoretical methods,

as DMRG and ED already employed in Chapter 2, will allow to investigate the effects of the finite temperature and inhomogeneity of our system on the experimental diagram (Sec. 3.2). Finally, in Sec. 3.3, we will present measurements of the excitation spectrum of the system. Such measurements will allow to determine the features of the strongly-correlated BG phase, and in particular, to distinguish it from the MI present in the lattice at strong interactions. Further spectral measurements extending from weak to strong interactions, will finally show the different nature of the BG phase in the two regimes.

3.1 Δ - U phase diagram

Let us start considering the phase diagram for "dirty" interacting bosons in the conceptually easier case of random disorder, that is in absence of the lattice and consequently of the MI phase. Fig. 3.1 shows the $T = 0$ phase diagram as a function of the interaction energy U and the random disorder strength D. Such a diagram shows that the SF is surrounded by the BG both in the regime of strong (BG I) and weak interactions (BG II). Whether these two phases are the same phase or not is still an open question [127]. Of course for BG I, the correlation length ξ is short, of the order of the mean particles separation, contrary to the weakly-interacting case. But what it is actually interesting to note here is the specular behaviour of the transition lines in those two regimes. This behaviour can be understood considering the fermionic nature of bosons in the limit of infinite interactions (right hand side of the transition blue point). As already described in Subsec. 1.1.3, in such a limit the strong repulsion between bosonic particles acts as the Pauli exclusion principle for fermions, so that here one can assume to deal with non interacting fermions. If we now move from right (blue point) to left (towards the center of the transition curve) the interaction for fermions increases in the opposite way, that is decreasing U. In this frame of symmetry between bosons and fermions, we can easily understand the effect of disorder: as weakly interacting bosons get localized by disorder (see Subsec. 1.2.2), in

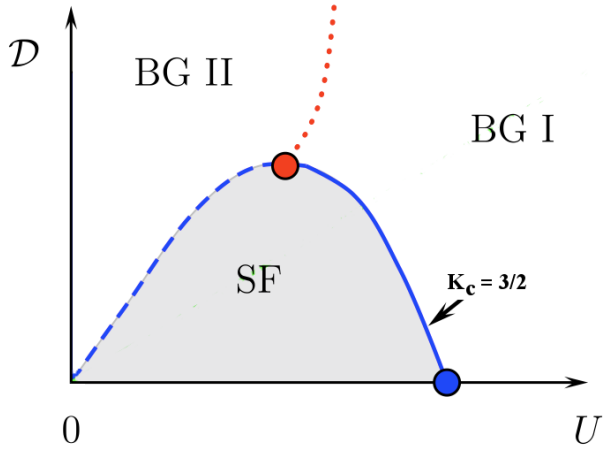

Figure 3.1: Disorder-interaction phase diagram of a 1D Bose gas at $T = 0$ in the case of random disorder D [126]. The BG insulating phase(s) show a symmetric reentrant shape around the SF phase. In the presence of disorder at strong enough interactions the fermonized Bose gas Anderson-localizes at the universal critical value of $K = 3/2$ (solid blue line). The blue dashed line shows the analogous metal-insulator transition for weakly-interacting bosons. The red dotted line marks the possible border between the two (possibly distinct) insulating phases, BG I and BG II.

the same way disorder induces Anderson localization for weakly interacting fermions. Moreover, as the effect of disorder can be screened by increasing U for the weakly interacting localized bosons (Subsec. 1.2.3), in the same way for the weakly interacting localized fermions the coherence of the system can be restored by decreasing U.

Quasi-periodic disorder. Let us now consider the case of the quasi-disorder potential introduced by a bichromatic lattice. For this case, which is also the case of our experiment, we refer to all the arguments described in Sec. 1.2 for the disorder Bose-Hubbard model, whose Hamiltonian is here reported:

$$\begin{aligned} H_{DBH} = & - J\sum_i (b_i^\dagger b_{i+1} + h.c.) + \Delta \sum_i \cos(2\pi\beta i) n_i \\ & + U\sum_i n_i(n_i-1)/2 + \alpha \sum_i (i-i_0)^2 n_i/2 \end{aligned} \tag{3.1}$$

The tunneling energy J, the interaction energy U and the disorder strength

Δ are the three main energy scales characterizing the system properties. α is the energy offset between neighboring sites of the harmonic trap potential.

In Fig. 3.2 I show the $T = 0$ phase diagram of 1D bosons in the quasi-periodic lattice as a function of the ratios Δ/J and U/J, obtained by numerically solving the Bose-Hubbard problem in the particular cases of occupancy $n = 0.5$ and $n = 1$ [74]; As we can see, due to the presence of the lattice

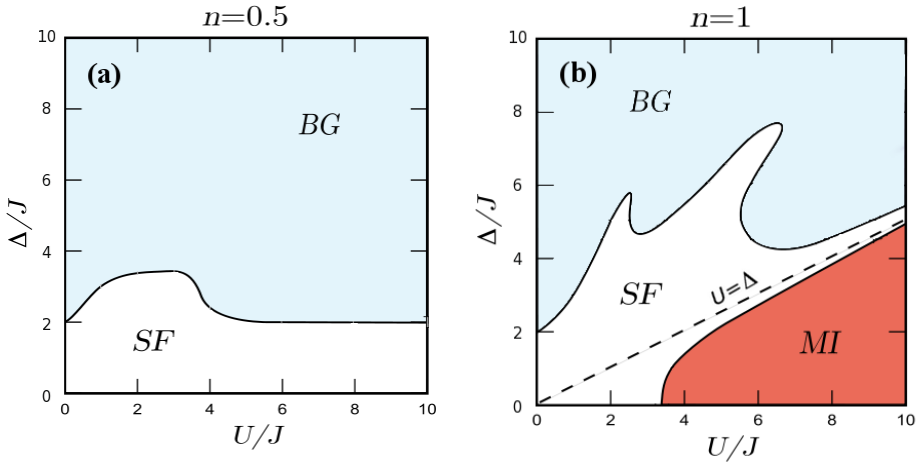

Figure 3.2: $\Delta - U$ phase diagram of a 1D Bose gas at $T = 0$ in the case of a quasi-periodic disorder for two different fillings n [74]. (**a**) $n = 0.5$: the non-interacting bosons (fermions) get Anderson-localized at $\Delta = 2\,J$, the SF-BG transition showing a reentrant shape analogous to that of the continuum case. (**b**) $n = 1$: the dashed line indicates the disorder strength $\Delta = U$ above which for $U \gg J$ the MI energy gap vanishes. An inhomogeneous system (different fillings n) is expected to qualitatively behave as a mixture of the two cases.

the scenario now results clearly more complex. Besides the SF and the BG phases, in general here there is also the MI phase[1]. Nevertheless, since an integer occupancy n is required for the MI phase to form, in the case $n = 0.5$ only the SF and BG phases exist. In this case the SF-BG transition has a reentrant shape that doesn't differ too much with respect to the continuum case previously described, except for the fact that for entering the Anderson insulating phase a minimum disorder strength ($\Delta = 2\,J$) is required (see Sub-

[1]Due to its importance, we recall that the BG can be actually thought of as an intermediate phase between a MI and a SF phase. Like a MI, it is insulating and like a SF, it has a gapless excitation spectrum and consequently a finite compressibility.

sec. 1.2.2), both in the limit of non-interacting bosons and non-interacting fermions.

As for the $n = 1$ case, a MI phase instead forms for strong interactions (see Subsec. 1.2.1). Adding disorder, such a gapped phase persists up to the value $\Delta = U$ (dashed line) where the excitation spectrum becomes gapless and the system first becomes a SF and then a BG.

We finally stress that in the experiments, due to the trap confinement, the number of atoms per site n in general varies along the optical lattice, meaning that we expect a phase diagram that is a combination of the two pictures of Fig. 3.2. In particular we aspect that in the regime of strong interaction ($U \gg J$), the presence of disorder has a twofold effect [16]. On the one hand, it induces a disordered MI in regions with commensurate filling (integer n). On the other hand, in regions with incommensurate filling (non integer n) arguments similar to those used for the strongly correlated 1D system in the continuum can be applied, that is the fermionized bosons localize in the disorder resulting in the BG phase.

3.1.1 Coherence measurements

Let us now see how we can employ our experimental system to build a phase diagram [125], which the theoretical ones just shown have to be compared to. As usual, the experimental setup we employ is a set of quasi-1D systems of ^{39}K atoms in a quasi-periodic optical lattice, which are described by the disordered Bose-Hubbard Hamiltonian 3.1. Here, the tunneling energy $J/h \simeq 110\,\mathrm{Hz}$ is set by the depth ($s = 9$) of the primary lattice, while the interaction energy U and the disorder strength Δ can be independently controlled respectively changing the Feshbach magnetic field and the depth of the secondary lattice. Depending on the U and Δ values, the mean site fillings range from $n = 2$ to $n = 8$. As for the system temperature, with the technique reported in Subsec. 2.3.1 in the SF regime we get $k_B T \simeq 3\,J$, which as already said, is below the degeneracy temperature $k_B T_D \simeq 8\,J$.

As described in Subsec. 2.2.2, the coherence properties of our system can

be investigated by measurements of the momentum distribution $\rho(p)$, which are obtained by standard time of flight images according to the experimental procedure reported in Subsec. 2.2.3. From the fitted root-mean-square width Γ of $\rho(p)$, which can be viewed as a measure of the inverse of the correlation length (Eq. 2.11), we can build a two dimensional diagram; Fig.3.3 shows the behaviour of Γ as a function of Δ/J and U/J, obtained by interpolating 94 sets of measurements. The plot is representative of the phase changes

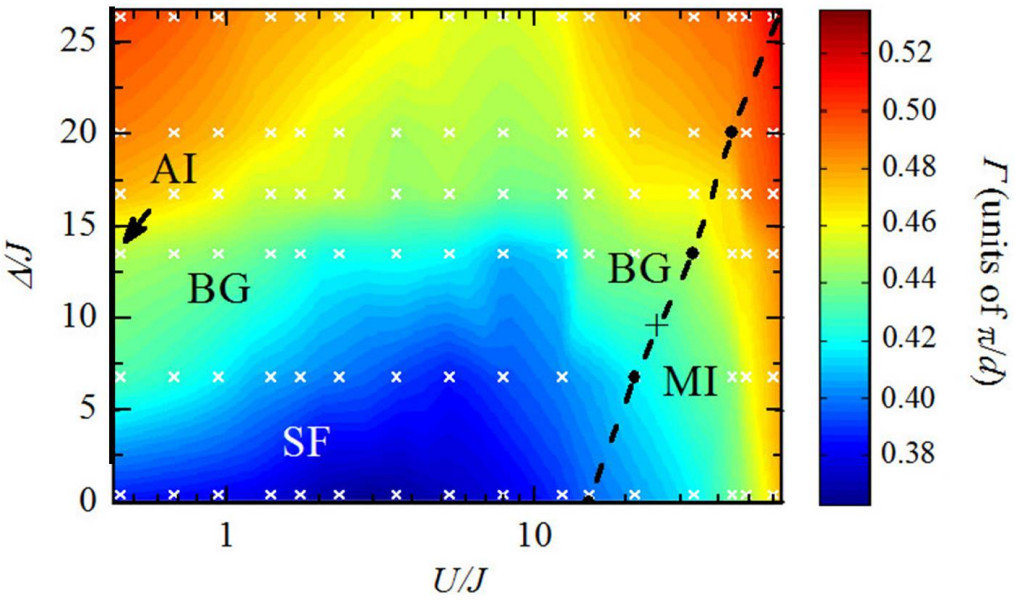

Figure 3.3: Measured rms width Γ of the momentum distribution $\rho(p)$ in the $\Delta - U$ plane. The diagram is built with 94 data points (crosses), with a standard deviation between 2% and 5%. The blue zone corresponds to a narrow momentum distribution (SF phase), whereas the green, yellow and red zones correspond to progressively broader momentum distributions (insulating phases). According to $T = 0$ DMRG calculations MI domains exist only at the right of the dashed line (i.e. $U > 2\Delta$ for large U), where they coexist with SF or BG domains.

occurring in the system. At small disorder and interaction values where the system is SF, $\rho(p)$ is narrow as in Fig. 2.3 (blue zone). At larger disorder and interaction values, $\rho(p)$ progressively broadens (green, yellow and red zones) meaning that the system is becoming more and more incoherent (see Fig. 2.5). In particular, along the $\Delta = 0$ line, there is the progressive forma-

tion of MI, which in our inhomogeneous system coexists with a SF fraction[2]. For increasing Δ along the non-interacting line, an Anderson insulator (AI) forms above the critical value $\Delta = 2\,J$ predicted by the Aubry-André model [49, 84]. For finite U and Δ we observe a reentrant insulating regime extending from small U and $\Delta > 2\,J$ to large U which surrounds a SF regime at moderate disorder and interaction. This shape recalls the behaviour of the BG previously described in the theoretical phase diagram of Fig. 3.1 obtained in the particular case of homogeneous systems at $T = 0$ with random disorder. Of course, the presence of MI domains due to the lattice (together with the system inhomogeneity and finite temperature) makes things more complex here. Nevertheless, it is interesting to note that the phase crossover at strong interactions has an opposite (negative) slope with respect to the dashed line delimiting the region of MI domains (obtained using DMRG calculations, as we shall see in Sec. 3.2). This suggest that the insulating behaviour resulting from the experimental diagram is likely due to the presence of another type of insulator, the BG. Such indication will be confirmed in Sec. 3.3 when probing the nature of the insulating phases with excitation spectrum measurements.

3.1.2 Transport measurements

In order to confirm the insulating nature of the observed incoherent regimes, we have performed transport measurements. These are performed in the following way: we first apply a sudden shift to the harmonic confinement, corresponding to a force $F = mg/3$, g being the gravity acceleration; we then detect with TOF images the quasimomentum p_0 transferred to the system in a time interval of 0.9 ms, just before the system becomes dynamically unstable (see Sec. 2.4.2). The transferred quasimomentum p_0 can be thought of as the effective mobility of the system. The procedure is basically the same as

[2]the unavoidable trapping confinement makes the system inhomogeneous and limits its size. As a consequence, in the experimental system there is coexistence of different phases and the theoretical sharp quantum phase transitions occurring in the case of the thermodynamic limit are actually replaced by broad crossovers.

in the transport measurements described in Fig. 2.9 but instead of measuring the full time evolution of p_0, here the time interval is kept constant. Even though such simplified method doesn't allow to precisely measure the transition between an insulator and a conductor, it is still effective to qualitatively show the insulating behaviour of the system throughout the $\Delta - U$ plane.

In Fig. 3.4 I report the transferred quasimomentum p_0 as a function of U for three different values of Δ. In the case of no disorder and small U

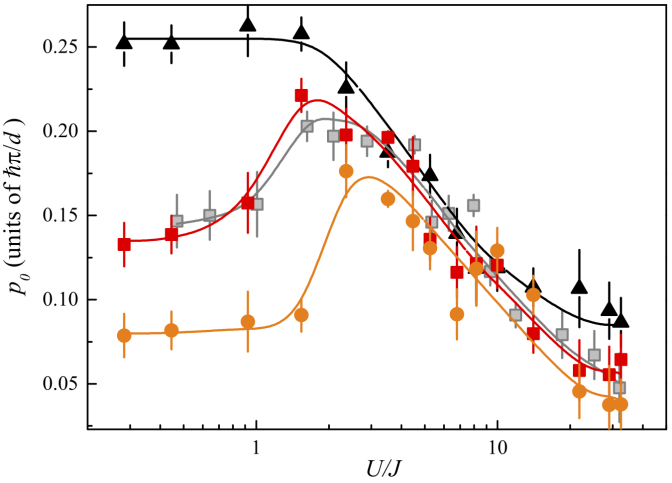

Figure 3.4: Effective mobility p_0 after a given evolution time $t = 0.9\,\mathrm{ms}$ in the tilted potential as a function of U, for three different values of disorder strengths: $\Delta = 0$ (black triangles), $\Delta = 6.2\,J$ (red squares) and $\Delta = 8.8\,J$ (orange circles). Those measurements are preformed at $k_BT = 3.1(4)\,J$. The grey squares show a second measure at $\Delta = 6.2\,J$ but at higher temperature, $k_BT = 4.5(7)\,J$. The lines are a guide to the eye. The error bars are the standard deviation of typically 5 measurements.

the system is conductive; increasing U the mobility decreases more and more while crossing the SF-MI transition. For finite Δ and $U = 0$ the system is an AI, featuring a reduced mobility (which is however not zero, because of the finiteness of F); we then observe an initial increase of the mobility with U, followed by a drop at larger U. These observations indicate that in the presence of disorder both incoherent regimes at small and large U are actually insulating regimes, and not simply incoherent excited phases. They also confirm that a moderate $U \sim \Delta$ tends to bring the weakly interacting insulator back into a fluid regime with a mobility close to that of a SF. A

larger U drives instead the system into an insulating phase which is even less conductive than the clean MI regime.

A second measurement performed at a higher temperature, also shown in Fig. 3.4, indicates that the mobility for intermediate disorder strength is essentially T-independent in the range $k_B T = (3.1 - 4.5)\, J$.

Metal-insulator transition at weak interaction [111]. We now study the metal-insulator transition at weak interaction by applying the more precise transport measurement technique already used in the clean case to determine the SF-MI transition (see Subsec. 2.4.2). Using the same experimental scheme used for the clean lattice, we now add disorder and study the dynamics (that is the time evolution of the transferred quasimomentum p_0) in the quasi-periodic lattice. In particular, here we focus on the weak interaction regime $U < 3\, J$, where the critical momentum p_c for the non-disordered lattice can be measured with high accuracy. Note that a measure of the metal-insulator transition at strong interaction with this technique is prevented by the interaction-enhanced phase fluctuations which make the measure of p_c a difficult task in such regime.

Fig. 3.5a shows the time evolution of the quasimomentum p_0 for a given interaction energy U and for different disorder strengths Δ: increasing Δ the dynamics becomes clearly more and more damped. The experimental data are analyzed in the same way as for the clean case (see Fig. 2.13). We thus distinguish two dynamical regimes: we extrapolate the damping rate G_{in} of the initial, stable regime and the critical momentum p_c for entering the regime of instability. A small disorder Δ results in a moderate increase of G_{in} and in an anticipated instability with respect to the clean case; at large disorder, G_{in} drastically increases and the system immediately "breaks"[3].

[3]We note that both the increase of G_{in} and the reduction of p_c with increasing Δ, can be justified according to the following heuristic picture: in the presence of disorder, the hopping amplitude J reduces, resulting in an effective tunneling energy $J_{eff}(\Delta) < J$, thus inducing an increase of the phase-slips nucleation rates 2.25 which exponentially depend on J. In fact, a related phase-slip model [128] developed for disordered superconductors suggests nucleation rates scaling exponentially with Δ.

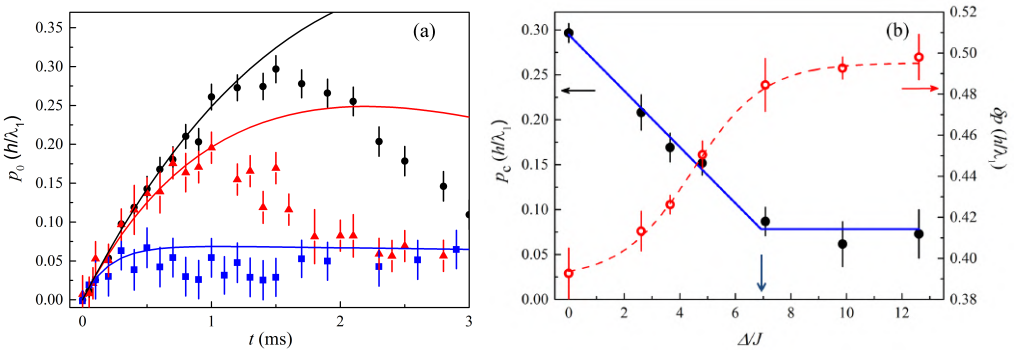

Figure 3.5: (**a**) Time evolution of the quasimomentum p_0 at a given interaction energy ($U = 1.26\,J$) for three disorder strengths: $\Delta = 0$ (dots), $\Delta = 3.6\,J$ (triangles) and $\Delta = 10\,J$ (squares). The lines are fits to the initial oscillation with the solution of the motion equations 2.22. The fitted damping rates are $G_{in}/2\pi = 130(10)$ Hz, $G_{in}/2\pi = 250(30)$ Hz and $G_{in}/2\pi = 1.1(6)$ kHz, respectively. (**b**) Critical momentum p_c (full circles) and initial rms momentum width δp (open circles) as a function of Δ at the same given $U = 1.26\,J$. A peacewise linear fit (continuous line) determines the critical disorder strength Δ_c (blue arrow) to enter the BG phase. The dashed line is a sigmoidal fit of δp.

Fig. 3.5b shows the behaviour of the critical momentum p_c as a function of the disorder strength Δ at the same given U: p_c features a clear decreasing trend for increasing Δ. Above a critical disorder strength Δ_c (of the order of the total interaction energy per atom nU), p_c stops decreasing and remains constant at a small value close to zero, as observed for the MI. By fitting $p_c(\Delta)$ with a piecewise linear function we thus determine the critical value Δ_c to enter the (weakly interacting) BG phase.

In order to determine the SF-BG transition (at weak interaction) we repeated the measurements for different values of U, that is we measured Δ_c as a function of U. A summary of these measurements is reported in the $\Delta - U$ plane of Fig. 3.6 together with the coherence measurements of Fig. 3.3 as a comparison. As expected, Δ_c increases with the interaction energy in agreement with the screening argument described in Subsec. 1.2.3: an increase of interaction delocalizes the system making its effective mobility less affected by disorder.

As for the comparison with the coherence diagram, remarkably the line of the metal-insulator transition has the same slope as the coherence dia-

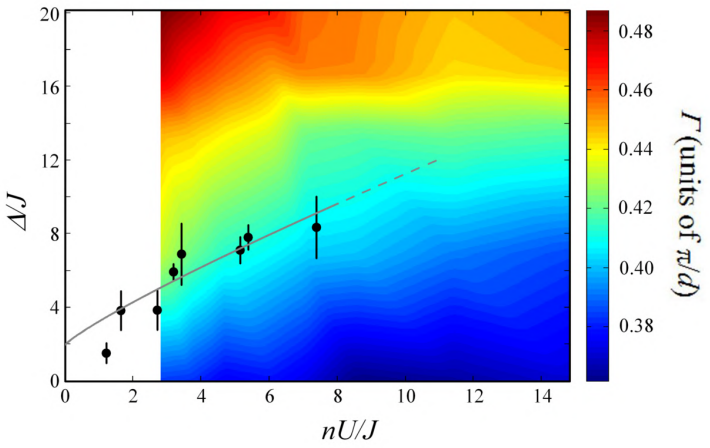

Figure 3.6: Comparison between the metal-insulator transition obtained by transport measurements and the $\Delta - U$ coherence diagram of Fig. 3.3 in the regime of weak interaction. The x-axis of the diagram has been rescaled by the mean site filling n at the interaction U. The red line is a fit to the experimental data (dots) with the function $\Delta_c = 2J + AJ(nU/J)^\alpha$, which accounts for the critical disorder value $\Delta \simeq 2J$ required to localize the non-interacting system [90]. The values of the fit are $\alpha = 0.86(22)$ and $A = 1.3(4)$. The large uncertainty on the data is due to an error of 20 % on the calibration of Δ.

gram. As a matter of fact transport and coherence properties are strongly related one to the other. Nevertheless, while transport measurements allow determining a quite sharp transition, the measurements of coherence provide a broad crossover.

3.2 Comparison with theory

As already mentioned, the challenge of the experimental investigation of the phase diagram and of its comparison with the ideal theoretical case lies in the inhomogeneity and in the finite temperature of the system. In order to achieve the closest experiment-theory comparison we perform a study of the inhomogeneous systems described by Hamiltonian 3.1 using DMRG calculations, as already done in Subsec. 2.3 for the limited case of the SF. In the next section we will then use a phenomenological approach to extend the results to the finite T case. DMRG calculations at $T = 0$ give access to the density profiles of the system and to all the single-particle correlation

functions $g_{ij} = \langle b_i^\dagger b_j \rangle$ in the ground-state.

Let us first consider the effect of the system inhomogeneity. In Fig. 3.7 we report the calculated density profiles in tubes with $N = (20, 55, 96)$ atoms in the case of large interaction. In the absence of disorder, the profiles show

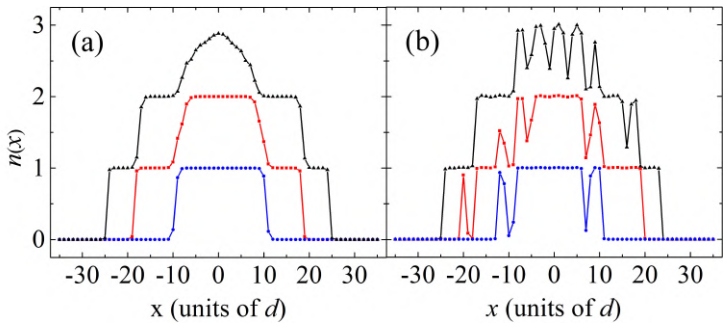

Figure 3.7: Density profiles obtained from DMRG calculations at a given strong interaction, $U = 26\,J$. (**a**) Clean case ($\Delta = 0$): typical wedding cake structure alternating SF and MI phases. (**b**) disordered case with $\Delta = 6.5\,J$: the SF component (non-integer n) is replaced by the BG. Blue, red and black curves refer respectively to tubes with $N = 20, 55, 96$ atoms.

the typical wedding cake structure, where the commensurate Mott domains (integer n) are separated by incommensurate SF regions (non-integer n). Adding disorder, the Mott regions progressively shrink and the smooth density profiles of the incommensurate regions are turned into strongly irregular ones, as expected in the case of a BG. We note that the dashed line in Fig. 3.3 delimits the region of MI domains, which are here defined by the condition that in the density profiles there are at least three consecutive sites with an integer filling.

From the DMRG calculated correlation functions g_{ij} we can then obtain the $T = 0$ momentum distributions $\rho(p)$ for our inhomogeneous system, using Eq. 2.12 as already described in Sec. 2.3. Fig. 3.8 shows the full $\Delta - U$ diagram, obtained by interpolation of the rms widths Γ of $\rho(p)$, together with few distributions $\rho(p)$ at representative points.

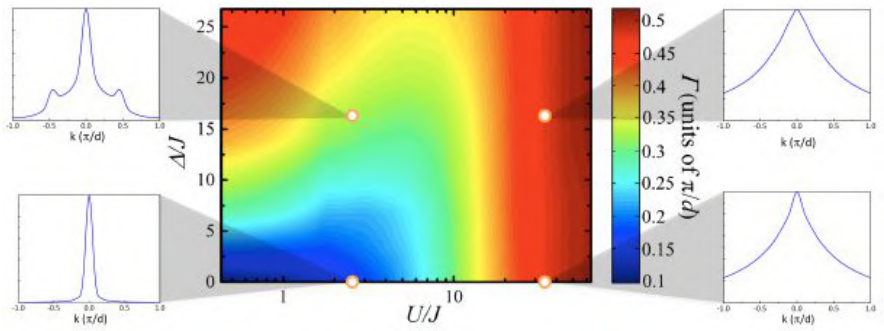

Figure 3.8: Theoretical rms width Γ of $\rho(p)$ at $T = 0$, calculated for individual tubes, and then averaged over the distribution of tubes. The diagram is built with 94 data points at the same positions of the experimental data in Fig. 3.3. For few representative points, $\rho(p)$ is also shown at the side of the diagram.

3.2.1 Finite temperature effects

To account for finite temperature effects, we again extend to the whole phase diagram the procedure described in Sec. 2.3 for the SF. We thus compare the experimental $\rho(p)$ to those of the $T = 0$ theory. By looking at Fig. 3.9, we can immediately notice that for small U (panels a and b) the theoretical $\rho(p)$ (blue curve) is considerably narrower than the experimental one (black curve), while for large U (panels c and d) the thermal broadening is much less relevant. Once again, the thermal broadening is quantified by the inverse thermal correlation length $1/\xi_T$ of Eq. 2.13, here reported:

$$\frac{1}{\xi} = \frac{1}{\xi_0} + \frac{1}{\xi_T}. \tag{3.2}$$

Basically, in Eq. 3.2 $1/\xi_0$ is the width of the $T = 0$ (blue) distribution given by DMRG calculations, while $1/\xi$ is the width of the (red) theoretical distribution (see Fig. 3.9a). More precisely, ξ_T is determined as a free fitting parameter of the theoretical distribution (resulting from the convolution of the $T = 0$ distribution with another Lorentzian distribution of width $1/\xi_T$) that best matches with the experimental one. We obtain a good agreement between theory and experiment in all the representative points of Fig. 3.9 with the only exception of the large-U, low-Δ regime (panel c), where the (red) tails of the theoretical distribution result larger. Such good agreement

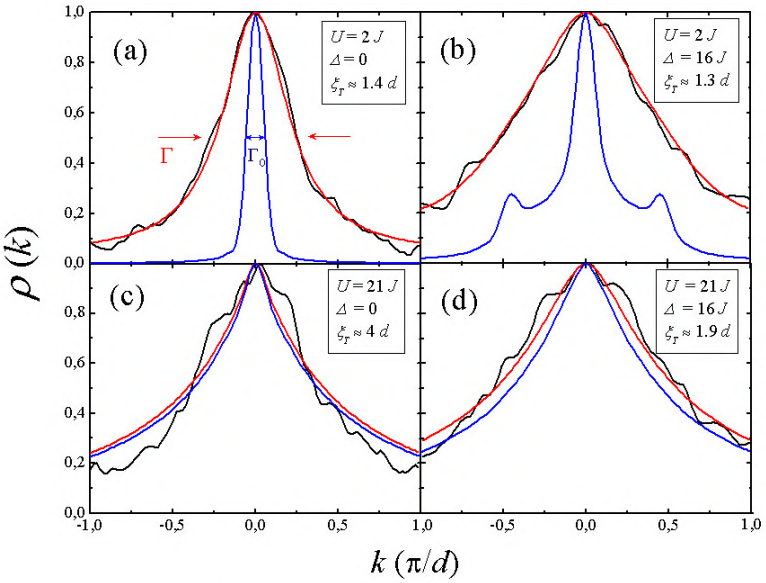

Figure 3.9: Comparison between the experimental momentum distribution $\rho(k)$ (black, continuous) and the one obtained with DMRG calculations for our inhomogeneous system at $T = 0$ (blue, dash-dotted), for four points in the $\Delta - U$ plane. The momentum p is here expressed in terms of the wavevector $k = p/\hbar$. The thermal correlation length ξ_T, which phenomenologically accounts for thermal effects, is obtained from the convolved momentum distribution (red) of width $\Gamma = \Gamma_0 + 1/\xi_T$ that best matches with the experimental one.

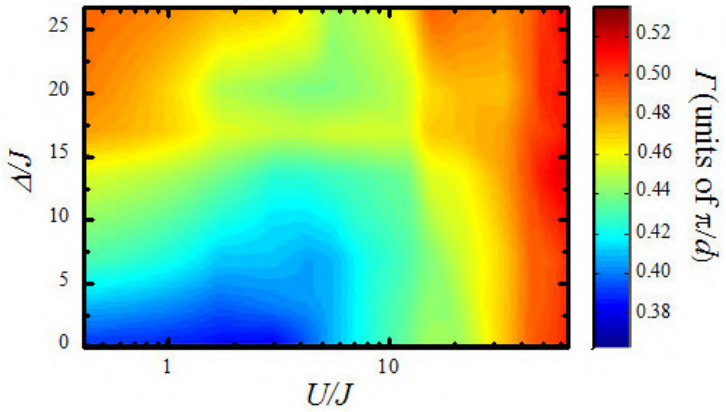

Figure 3.10: $\Delta - U$ diagram for the rms width Γ of $\rho(p)$ obtained starting from DMRG calculations at $T = 0$ and phenomenologically taking into account thermal effects. The diagram is built with the same data points as in Fig. 3.3.

appears even clearer by comparing the whole $\Delta - U$ theoretical diagram for the width Γ of $\rho(p)$ (see Fig. 3.10) with the experimental one of Fig. 3.3.

As a matter of fact, this phenomenological approach well reproduces the experimental $\rho(p)$ in all regimes, except for the one just mentioned where the coexisting incommensurate SF/BG and commensurate MI phases have different ξ_T. As it will be clearer in the next section, the use here of a single ξ_T parameter to fit $\rho(p)$ leads to an overestimation of the rms width Γ.

In Fig. 3.11 we report the fitted ξ_T across the whole $\Delta - U$ diagram. For

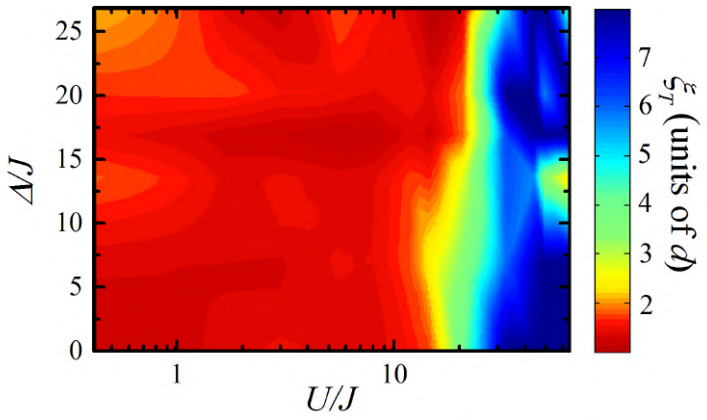

Figure 3.11: $\Delta - U$ diagram of the thermal correlation length ξ_T resulting from the fit in the experiment-theory comparison. Thermal effects are significantly more relevant for small U.

$U < 10\,J$ it is rather short ($\xi_T \approx d$), showing a relevant thermal broadening for the SF and (weakly-interacting) BG phases. ξ_T is also quite constant, indicating that the shape of the diagram is the same as the one at $T = 0$. In the large-U regime, ξ_T does increase considerably, indicating that the strongly-correlated phases are only weakly affected by the finite T. Additional measurements and finite-T simulations shown later on will confirm these indications.

3.2.2 Quantum to normal phase crossover temperature

In Subsec. 2.3.1 we employed the ED method to relate the SF temperature of the system to the measured momentum distribution $\rho(p)$. We now apply the same method to get more information on the finite temperature effects

in our system. Besides confirming the results obtained with the phenomenological approach, such a method will allow us to determine the crossover temperature above which the system in the strong-interaction regime loses its quantum properties. By diagonalizing the Hamiltonian 3.1 for small homogeneous systems with length up to $L = 12\,d$ we obtain, for a given U and Δ value, the temperature dependence of the correlation length $\xi(T)$ of the system.

As a first case we consider the regime of weak interaction. Fig. 3.12 shows the correlation length $\xi(T)$ at a given interaction ($U = 2.3\,J$) for three different disorder strengths. This study confirms the previous results of large

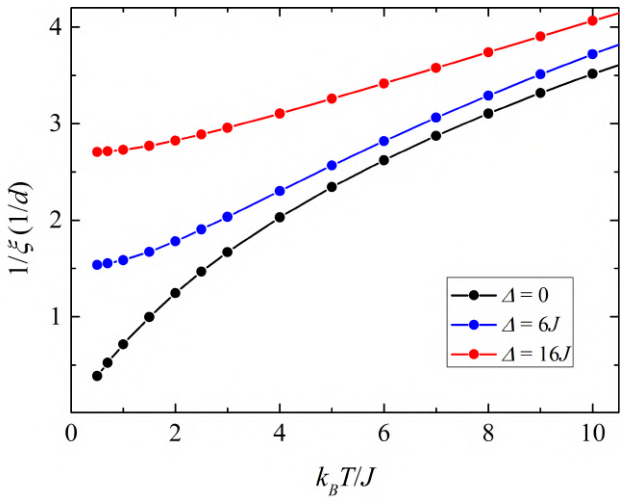

Figure 3.12: Inverse correlation length vs T calculated by exact-diagonalization for a weakly-interacting system ($U = 2.3\,J$) with $n = 0.46$ and for three disorder values ($\Delta = 0,\ 6\,J,\ 16\,J$). Note that thermal effects are relevant already at small T values.

thermal effects for small U. As a matter of fact, the inverse correlation length starts to increase already for very small temperatures, implying a non-negligible impact of thermal fluctuations on the $T = 0$ quantum phases and thus justifying the experimental observation of a rather short ξ_T for weak interactions. Nevertheless, it is interesting to point out that according to the transport measurements previously described (see Fig. 3.4), the loss of coherence due to the increase of temperature is not accompanied by a change

of the system mobility[4].

Differently from the case of small U, for large interactions ($U > 10\,J$) the calculated correlation length $\xi(T)$ is almost T-independent at low temperatures while a relevant broadening sets in only above a crossover temperature T_0 (Fig. 3.13). T_0 is here determined as the maximum of the first derivative

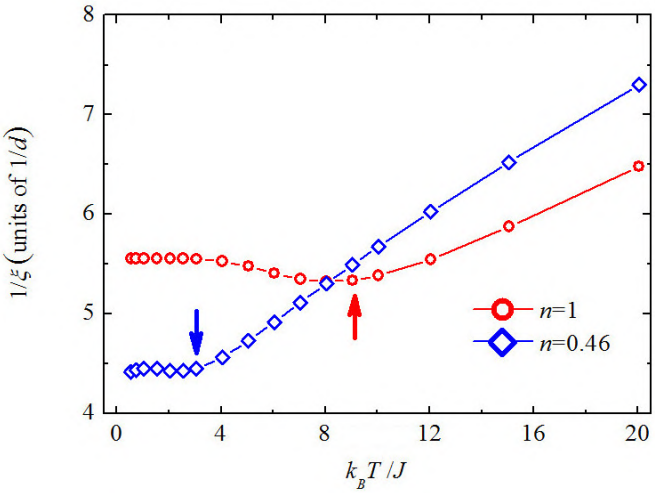

Figure 3.13: Inverse correlation length vs T calculated by ED for a strongly-interacting system ($U = 44\,J$) with $\Delta = 10\,J$ for both the commensurate case of MI ($n = 1$) and the incommensurate case of BG ($n = 0.46$); the arrows mark the crossover temperatures T_0 below which the inverse $\xi(T)$ is quite constant and thus the quantum properties of the system are not affected by the temperature.

of $1/\xi(T)$. This effect can be clearly seen not only for the MI phase, occurring when the thermal energy $k_B T$ becomes comparable with the energy gap U [131], but also for the gapless BG.

Fig. 3.14 shows the calculated crossover temperature T_0 as a function of Δ for one representative interaction strength and for both the cases of commensurate and incommensurate density. For the commensurate density at $\Delta = 0$, we get $k_B T_0 = 0.23(6)\,U$, in agreement with the predicted "melting" temperature for the MI, $k_B T_0 \simeq 0.2\,U$ [131]. As Δ increases T_0 decreases,

[4]The fact that the insulating behaviour persists also at finite T could in principle be related to the many-body localization phenomenon [129, 130].

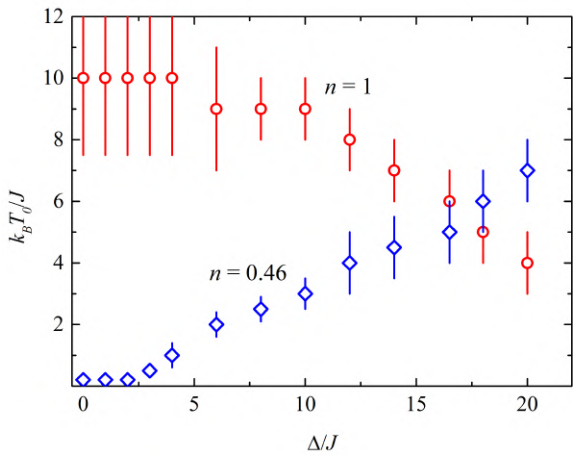

Figure 3.14: Crossover temperature T_0 vs disorder strength Δ, calculated by exact diagonalization for a strongly interacting system ($U = 44\,J$), for both the commensurate case of MI ($n = 1$) and the incommensurate case of BG ($n = 0.46$). In the latter case T_0 shows a linear increase with Δ meaning that at large enough disorder the quantum properties of the BG are preserved even at finite T.

consistently with a reduction of the gap due to the disorder. As for the BG, the crossover temperature instead shows a linear increase, $k_B T_0 \propto \Delta$[5].

For large Δ, the simulations indicate that T_0 is comparable with the temperature 2.17 measured experimentally in the SF regime ($k_B T \simeq 3\,J$), supporting the result obtained in the previous section of a large observed ξ_T at strong interactions. Moreover, in the next section we will see that for $\Delta \approx 10\,J$, where according to the plot Fig. 3.14 we have $T_0 \approx T$, we can observe the excitation spectrum predicted by theory for the BG.

We finally note that the crossover temperatures in the incommensurate and commensurate cases are different for small disorder and large interaction; this fact clarifies why the fit of the momentum distribution with only one ξ_T is not working properly in this regime, as we already mentioned in Subsec. 3.2.1 referring to Fig. 3.9c. In particular, while the SF component

[5]This result, already observed in numerical simulations at small disorder strength [132], can be intuitively justified with the following reasoning: the energy of the lowest levels that the fermionized bosons can occupy increases with the height of the disordered potential; so the higher the disorder strength Δ, the larger the effective Fermi energy for the existence of the quantum phase, that is the BG.

broadens increasing T, in the same way as it does for small U, the weakly-disordered MI component for $T < T_0$ does not. As a consequence, the use of a single ξ_T leads to an overall overestimation of the derived Γ in Fig. 3.10.

Entropy measurements. In order to experimentally confirm the results obtained by ED, a measurement of the momentum distribution width Γ as a function of T would be necessary. Unfortunately, as described in Subsec. 2.3.1, measurements of T are not straightforward outside the SF regime. It is however possible to measure the entropy of the system[6]. In Fig. 3.15 we

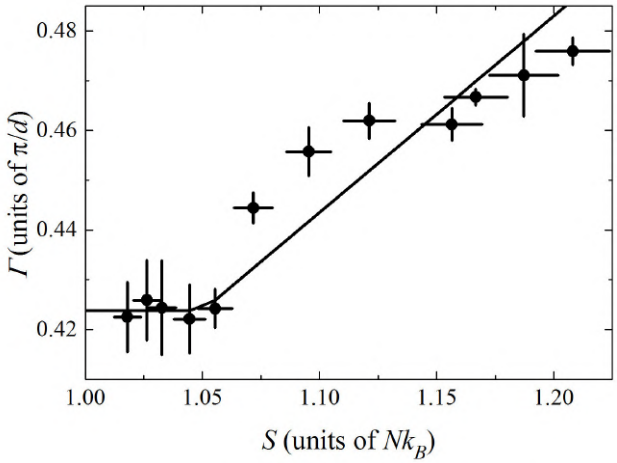

Figure 3.15: Measured rms width Γ of $\rho(p)$ for $U = 23.4\,J$ and $\Delta = 6.6\,J$ as a function of the entropy per particle. The corresponding SF temperature ranges from $3.1(1)\,J$ to $4.7(2)\,J$. Note the plateau at small S before Γ starts increasing. The line is a guide to the eye.

report the measured rms width Γ of $\rho(p)$ as a function of the entropy S in the regime of strong interaction and finite disorder, where the BG and the disordered MI phases coexist. The measurement clearly shows the existence

[6]The procedure for measuring the entropy of the 1D system is the following: we measure the initial entropy in the 3D trap; we measure again the entropy after having transferred the system into the 1D tubes and back into the 3D trap; we assume the mean value of the initial and final entropies as an indication of the entropy in the 1D tubes. In the BEC regime of $T/T_c < 1$, where T_c is the critical temperature for condensation in 3D, we use the relation $S{=}4N_T k_B \zeta(4)/\zeta(3)(T/T_c)^3$, where ζ is the Riemann Zeta function [133]. The reduced temperature T/T_c is estimated from the measured condensed fraction by taking into account the finite interaction energy. In the thermal regime, $T > T_c$, we use the relation $S = N_T k_B[4 - \log(N_T(\hbar\omega/k_B T)^3)]$.

of a plateau at low entropy, before a broadening sets in, which nicely recalls the theoretical behaviour of the inverse $\xi(T)$ in Fig. 3.13. This experimental result thus further strengthen the theoretical predictions that for sufficiently large U and Δ the $T = 0$ quantum phases can persist in the finite-T experiment.

3.3 Excitation spectrum

In Sec. 3.1 we traced the $\Delta - U$ diagram showing the crossover from the conductive to the insulating phases. In order to probe the nature of the insulating phases it is however necessary to investigate the excitation properties of the system. We recall in fact (see Subsec. 1.2.3) that while both the MI and the BG are insulators, they are characterized by a different excitation spectrum, gapped in the former case, gapless in the latter one.

In Fig. 3.16 we report a sketch representative of the predicted excitation spectrum for a bosonic system in a disordered lattice at strong interaction. The figure shows two excitation peaks: one centered at the energy $h\nu \sim U$

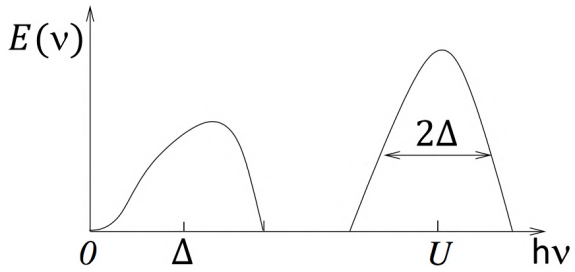

Figure 3.16: Sketch of the absorption energy spectrum of a strongly interacting system in a inhomogeneous disordered lattice. The peak at $h\nu \sim U$ with width $\sim 2\Delta$ is due to the disordered MI (in trap regions with integer n). The peak at $h\nu \sim \Delta$, which makes gapless the low-frequency spectrum, is instead due to the BG (in trap regions with no-integer n). Figure adapted from [134].

with width $\sim 2\Delta$ and the other one centered at $h\nu \sim \Delta$. Such a spectrum is due to the fact that, within an inhomogeneous trapped system, the regions with commensurate filling (integer n) form a MI with an energy gap of the order of U, while the regions with incommensurate filling (no-integer n) form

a BG that fills the low-energy gap. The effect of disorder is thus twofold, on the one side it causes a broadening of the MI peaks, on the other side, more interestingly, it causes Anderson localization for the non interacting fermionized bosons [17].

After describing the experimental procedure, in the following we will thus first consider the just mentioned case of strong interaction to experimentally show such a reach feature of the energy spectrum, able in particular to highlight (and distinguish) the presence of the BG phase coexisting with the MI in our inhomogeneous system (Subsec. 3.3.1). Other measurements performed from weak to strong interactions (Subsec. 3.3.2) will then characterize the spectral properties of the BG across the $\Delta - U$ diagram, corroborating the analysis and the informations obtained by the coherence and transport measurements.

Experimental procedure. In order to investigate the excitation spectrum of the system we employ a lattice modulation spectroscopy technique [92, 135]. This corresponds to measure the energy $E(\nu)$ absorbed by the system when the amplitude V_0 of the main lattice (and therefore the tunneling energy J) is modulated with a sinusoid of variable frequency ν. The experimental sequence is the following: after the standard loading procedure of the 1D quasicondensate in the quasi-periodic lattice (see Subsec. 2.2.3), the main lattice is modulated in amplitude for a given time t[7]. The depth of the main lattice thus becomes

$$V(t) = V_0(1 + A\sin(2\pi\nu t)) \tag{3.3}$$

where A is the modulation amplitude, which is kept constant[8], and ν is the modulation frequency, which is tuned to scan the excitation spectrum. After the excitation, the lattice potentials are exponentially ramped down

[7]We choose a modulation time $t = 200$ ms as long as possible, as allowed by the system background heating, in order to have the maximum sensitivity at low frequencies.

[8]We choose a modulation amplitude small enough ($A \sim 0.1$) to guarantee that the system response $E(\nu)$ to the perturbation (modulation) is linear.

in 300 ms, allowing the system to rethermalize via atom-atom collisions. The amount of energy $E(\nu)$ absorbed by the atoms as a function of ν is obtained by recording TOF absorption images and looking at the increase of the system temperature (with respect to the unperturbed case, i.e. $\nu = 0$). The temperature increase can be estimated in two different ways, either in terms of a reduction of the BEC fraction (as we did at large U) or in terms of an increase of the width σ of the thermal cloud (as we did at small U).

3.3.1 Signature of the Bose glass

Let us now consider a few experimental excitation spectra [125] in the regime of large interaction. This regime is of particular interest for two reasons: first, the reach spectral features expected by the theory, as just discussed. Second, probably more important, the negligible effect of the finite temperature of the experimental system, as described in Sec. 3.2. In this large U regime, we expect in fact that our observations directly reflect the properties of the $T = 0$ quantum phases.

Let us first consider the clean case ($\Delta = 0$). Fig 3.17 shows the standard

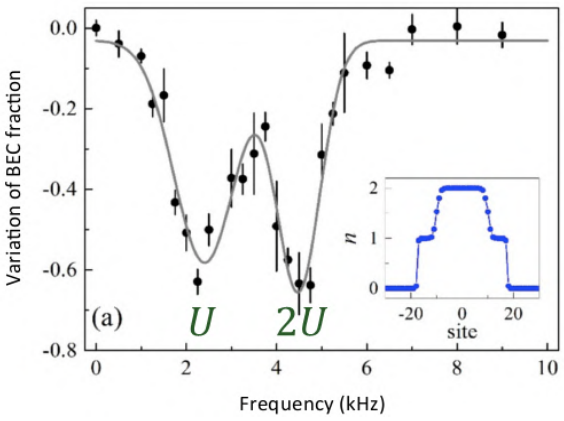

Figure 3.17: Excitation spectrum at $U = 26\,J$ and $\Delta = 0$. At low frequencies the system is not responding; a first excitation peak appears at the Mott-gap, $h\nu = U$, and a second one at about $2\,U$, due to the presence of MI domains with different filling n. Error bars represent the standard deviation of 5 measurements. (**inset**) DMRG density profile calculated for $N = 55$: MI domains with $n = 1$ and $n = 2$ are separated by incommensurate SF components characterized by a smooth (monotonic) change of density.

MI response [136, 137] of a strongly interacting system ($U = 26\,J$): at low frequencies, $h\nu < U$, essentially no absorption is observable. A first excitation peak appears at the Mott-gap, $h\nu = U$. This absorption peak is due to particle-hole excitations in the MI plateaus, that form in the inhomogeneous trapped system. For our typical densities we estimate MI domains with single site filling $n = 1 - 3$, depending on the trap zone. A second peak, centered at $h\nu = 2\,U$, is due to particles hopping from a lattice site with filling n to another site with filling $n + 1$ and is thus a consequence of the system inhomogeneity (see Fig. 1.10 in Subsec. 1.2.1). The MI domains are connected by intermediate SF regions with incommensurate filling (see wedding structure in Subsec. 1.2.1), which do not respond to the excitation in the regime of $U \gg J$.

When a finite disorder Δ is introduced, the system response to the external perturbation drastically changes. Fig. 3.18 shows the excitation spec-

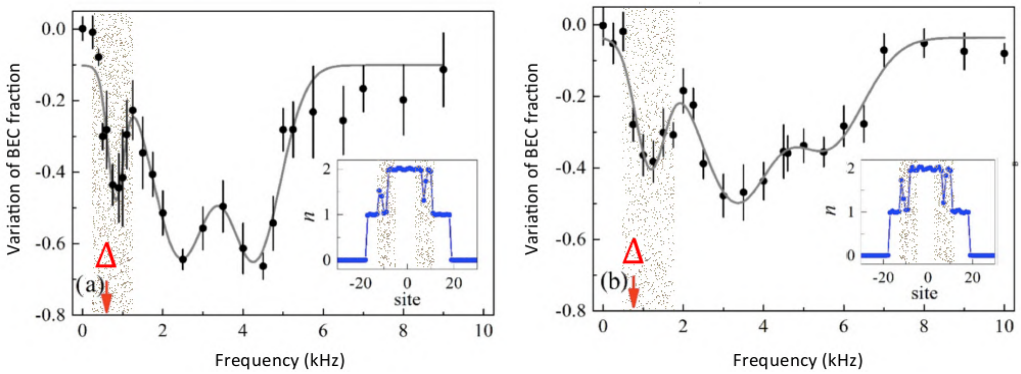

Figure 3.18: Excitation spectra at $U = 26\,J$ and SF temperature $k_B T \simeq 3\,J$, for two disorder strengths. (**a**) $\Delta = 6.5\,J$: with respect to the clean case of Fig. 3.17, the two Mott peaks are broadened and a new peak centered at $1.5\,\Delta$ fills the Mott gap. (**b**) $\Delta = 9.5\,J$: the low-frequency peak shifts towards higher energies and the Mott peaks are further broadened. The lines are a fit with multiple Gaussians. (**insets**) DMRG density profiles calculated for $N = 55$. The shaded areas represent the trap regions with incommensurate n responsible for the formation of the BG, characterized by a strong change of density in real space and by the "Δ peak" in frequency space.

tra at the same large U and SF temperature[9] as before for two different

[9]The experimental temperature $k_B T \simeq 3\,J$, which is measured in the SF regime as

disorder strengths Δ. As for the commensurate MI peaks, they broaden approximately by the amount Δ, as already observed in previous experiments [92], since the energy required to create particle-hole excitations is now site-dependent, and Δ quantifies the spreading of the on-site energies (see Fig. 1.17 in Subsec. 1.2.3). More interestingly, an additional peak fills now the Mott gap, at $h\nu \sim \Delta$. This observation strongly recalls the general picture discussed in Ref. [134] and summarized in Fig. 3.16, predicting a strongly-interacting BG phase characterized by a similar spectral response and coexisting with a disordered MI. As already discussed, within our inhomogeneous system the incommensurate trap regions (shaded areas of the figure) behave as a weakly-interacting Fermi gas, which in the presence of disorder undergoes Anderson localization, showing such a peculiar response at the characteristic disorder value Δ [17].

We finally note that due to the finite resolution[10] of our experiment at low frequencies we are not able to highlight the gapless nature of the system, nevertheless the presence of the extra "Δ-peak" peak strongly indicates that what we are dealing with is actually the BG phase. Such indication is then confirmed by the following comparison with a theoretical model.

Comparison with a model of fermionised bosons. In Fig. 3.19, the experimental data of Fig. 3.18 related to the "Δ-peak" are compared to the excitation spectrum evaluated, on the line of Ref. [134], with a model of fermionized bosons. The calculations are performed in the hard-core limit $U \to \infty$, where bosons can be mapped onto non-interacting fermions. In the regime of linear response, it is possible to derive the energy absorption rate (EAR) [138]. For the incommensurate component, which provides the BG

described in Subsec. 2.3.1, is of the same order of the crossover temperature T_0 below which the quantum properties of the strongly-interacting BG are preserved (see Subsec. 3.2.2).

[10]The finite resolution at low frequency, which is due to the inhomogeneity of our system, is given by the width ($\sim 0.5\,\mathrm{kHz}$) of the "Δ-peak".

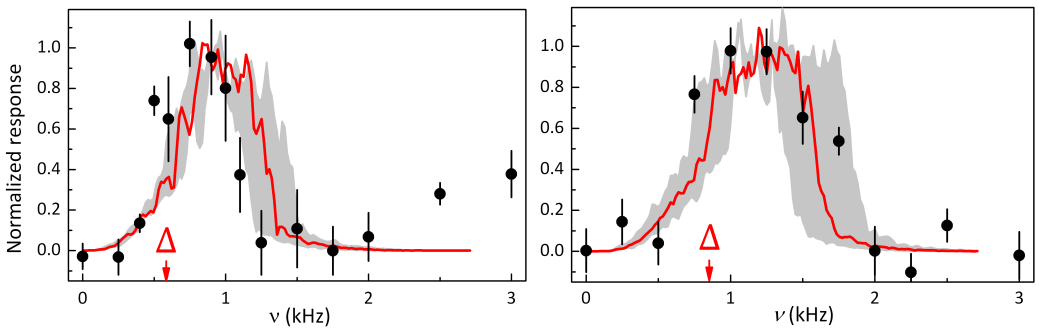

Figure 3.19: Comparison between the experimental data (dots) of the low frequency peak in Fig. 3.18 with a model of fermionized bosons (red curve), for the two disorder strengths: (**a**) $\Delta = 6.5\,J$ and (**b**) $\Delta = 9.5\,J$. Both the theoretical and the experimental peak responses have been normalized to unity; the Gaussian background due to the first Mott peak has been subtracted from the experimental data. The red curve is calculated at the nominal Δ while the grey region shows the effect of the 20 % uncertainty on Δ.

response, the EAR is given by

$$\dot{E}(\nu) = (\delta J^2 \pi^2 \nu) \sum_{a,b} \overline{K_{a,b}[f_{FD}(\epsilon_a) - f_{FD}(\epsilon_b)]\delta(\hbar\omega + \epsilon_a - \epsilon_b)}. \tag{3.4}$$

Here $K_{a,b} = |\sum_i (\phi_a^*(i+1)\phi_b(i) + \phi_a^*(i)\phi_b(i+1)|^2$ is calculated over pairs (a,b) of single-particle eigenstates of the quasi-periodic lattice, $f_{FD}(\epsilon)$ is the Fermi-Dirac distribution at finite T, and the bar represents the averaging over different realizations of the potential. Each spectrum is calculated evaluating Eq. 3.4 at different frequencies ν on a 200-sites lattice confined in a harmonic potential with axial frequency $\omega_z = 150\,\mathrm{Hz}$, as in the experiment. Calculations are performed at the experimental finite temperature $k_B T = 3\,J$. In the experiment the interaction energy U is not infinite, as assumed in the theoretical model; as a consequence the single site filling n is often larger than unity (in some zones of the harmonic potential we have $n = 2 - 3$). In the calculations, this is taken into account employing an extended-fermionization approach [139], i.e. neglecting the coupling between layers with different fillings ($n \leq 1$, $1 < n \leq 2$, $2 < n \leq 3$), and calculating their response independently. The larger kinetic energy of the fermionic excited bands is properly taken into account in the numerics. In fact, this approach is known to work rather well already at relatively small interac-

tions U, provided that the Mott-gap is open. Both the excitation spectra are the average of the spectra calculated for individual tubes over the whole distribution of tubes in the experiment.

As shown in Fig. 3.19, the calculated absorption peak well reproduces the experimental observation, confirming the qualitative picture presented in Fig. 3.16. The systematic shift of the experimental data towards lower frequencies might be a consequence of the $U = \infty$ approximation employed in the theoretical model. Anyway, the appearance of the "Δ-peak" experimentally probes the presence of a strongly-correlated BG coexisting with the disordered MI. Moreover, the theoretical DMRG analysis of the density distributions in the insets of Figs. 3.17 and 3.18, shows the spatial arrangement of the commensurate and incommensurate components in the typical tube ($N = 55$ atoms). Such analysis confirms that the smooth, monotonic density change of the incommensurate SF is turned by the disorder into a strongly varying one, as expected for a BG.

3.3.2 Excitations from weak to strong interactions

Let us now analyze the spectral properties of the system across the phase diagram. We will thus observe the behaviour of the excitation spectrum moving from weak to strong interaction at a given finite disorder. Let us first consider the case of weak interaction ($U < 3\,J$). We recall that in such a regime, thermal effects are quite relevant (small ξ_T in Fig. 3.11) and thus what we are dealing with is actually a finite-temperature system whose quantum properties are not necessarily preserved. We also recall that here the energy absorbed by the atoms is measured in terms of an increase of the width of the thermal cloud[11].

Fig. 3.20 shows the excitation spectra at $\Delta = 6.5\,J$ and for increasing (small) interactions. For vanishing U we observe a weak excitation peak centered at Δ which is consistent with the presence of an Anderson insulator

[11] In the regime of weak interaction, once the sample has been transferred back into the 3D trap decompressing the optical lattices, the BEC fraction results to be almost null.

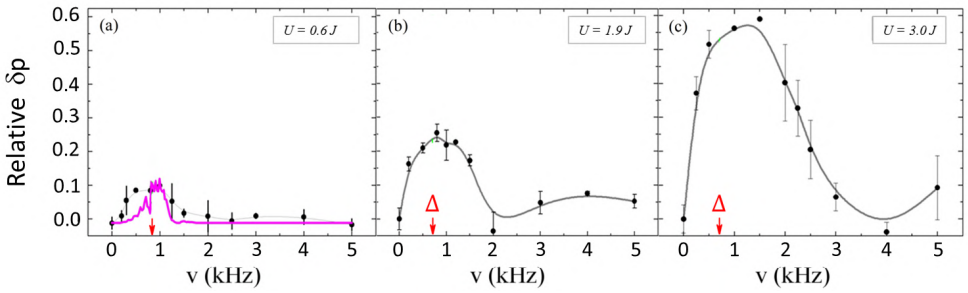

Figure 3.20: BG-SF crossover at $\Delta = 6.5\,J$. The absorbed energy is measured as the relative increase of the momentum distribution width δp. (**a**) AI case ($U = 0.6\,J$): the weak response centered at Δ (arrow) is consistent with a bosonic model (purple line). (**b**) A weak interaction ($U = 1.9\,J$) broadens and enhances the response, consistently with a partially delocalized BG. (**c**) A bit stronger interaction ($U = 3.0\,J$) further increases the low-frequency response, which becomes identical to that of a clean SF (not shown).

(AI). As a matter of fact the experimental excitation spectrum is well reproduced by a non-interacting bosonic model, built replacing $f_{FD}(\epsilon_a) - f_{FD}(\epsilon_b)$ with the Bose-Einstein distribution $f_{BE}(\epsilon_a)$ in the fermionic model previously employed. As we increase U, the system response progressively enhances and broadens, ending up with an excitation spectrum that is undistinguishable from that of a clean SF. This behaviour is thus consistent with the system crossing the BG-SF transition according to the argument discussed in caption of Fig. 1.15.

As for the regime of large U, Fig. 3.21 shows the excitation spectra at the same disorder strength as before and for interactions increasing in the range $U = (20-60)\,J$[12]. As described in the previous subsection, here the absorbed energy is measured in terms of a reduction of the BEC fraction and the peak centered at Δ is the signature of the strongly-correlated BG. The interesting thing is that such "Δ-peak" can be observed only in a limited region of U values[13]. As a matter of fact, when U is comparable with Δ, the MI and

[12]For an intermediate range of interactions ($3 \leq U < 20\,J$), no significative difference from the SF spectrum of Fig. 3.20c can be appreciated.

[13]As for the constraints for Δ, we note that for very large disorder strengths ($\Delta > 20\,J$), the spectrum features a broad peak centered at Δ that is only weakly affected by interaction (in all our accessible range of U), indicating that the system behaviour is dominated by disorder

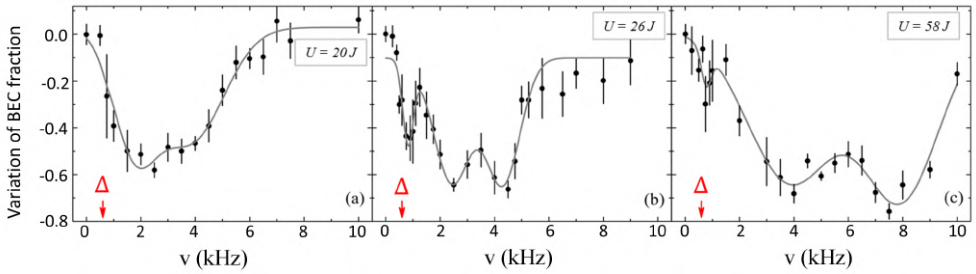

Figure 3.21: Excitation spectra in the strongly-interacting regime for increasing U. The spectra, measured as the relative reduction of the BEC fraction, are shown at the same given disorder strength $\Delta = 6.5\,J$ as in Fig. 3.20 and for three interaction energies. The tunneling energy corresponds to a frequency $J/h = 90$ Hz. (**a**) $U = 20\,J$: next to the broad SF spectrum the MI peak is only weakly enhanced at frequencies around U, while no spectral enhancement can be appreciated around Δ. (**b**) $U = 26\,J$: a BG peak centered at about $1.5\,\Delta$ appears, clearly separated from the two MI peaks. (**c**) $U = 58\,J$: the amplitude of the BG peak decreases, and most of the response is in the MI peak.

BG peaks overlap, the former being larger and covering the latter. When, conversely, U is much larger than Δ, the fraction of the incommensurate density that can form a BG becomes negligible and again only the MI peaks are detectable.

Let us finally compare the effect of increasing interaction in the two opposite regimes. In the low-U bosonic case, a small repulsive interaction favors the coupling of single-particle states, gradually restoring the superfluidity. As a matter of fact, the low-frequency response of the system at weak interactions enhances increasing U, indicating the possibility of long-distance excitations. Conversely, in the large-U fermionic case, excitations occur only on small length scales: increasing U the low-frequency SF response progressively reduces in favour of that of the (disordered) MI and the strongly-correlated BG.

In conclusion, the measurements of the excitation spectra, together with those of coherence (Fig. 3.3) and transport (Fig. 3.4), confirm the opposite (bosonic and fermionic) nature of the two regimes, as opposite is the role played by interactions: while weak interactions compete with disorder and screen the disorder-induced localization, restoring coherence between par-

ticles, conversely, strong interactions act as the Pauli exclusion principle, fermonizing the bosonic sample and favoring (Anderson) localization in the disordered system.

CONCLUSIONS AND PERSPECTIVES

In this thesis I have described how BECs in optical lattices can be employed to study key aspects of the physics of 1D superfluids and disordered systems. My work in particular focuses on two foundamental subjects: the phase slips excitations in 1D superfluids; the phase diagram of disordered, interacting 1D bosonic systems, with the associated problem of the Bose glass phase.

The experimental setup we employ, a ^{39}K BEC with a 3D optical lattice, on the one side offers the possibility to strongly confine the sample to study the 1D physics, on the other side, by means of Feshbach resonances and of a quasi-periodic optical lattice, offers the possibility to independently tune interactions and disorder.

In a first part of experiments we have employed a *clean* optical potential to investigate the coherence and transport properties of a 1D superfluid as well as its mechanisms of dissipation. More precisely, by comparing a static measurement of coherence with DMRG and ED models we established a new criterion to estimate the temperature of the 1D superfluid in the lattice. In particular we found that the estimated experimental temperature is lower than the 1D degeneracy temperature, confirming thus the quantum nature of our quasi-BEC.

As for the dissipation mechanisms of the superfluid, we studied the dynamics of the 1D quasi-BEC performing different transport measurements in

the optical potential. Preliminary measurements in absence of the lattice, showed in particular that for small interaction values, where the sound velocity v_s is smaller than the quasi-BEC velocity, the damping rate of the SF is quite large, as a presumable consequence of the energetic Landau instability.

Other transport measurements performed with a deep lattice ($s = 8$) and for increasing interactions showed that the system becomes dynamically unstable (abruptly strongly dissipative) above another critical velocity v_c, which decreases for increasing U and approaches zero at the SF-MI transition. Moreover, as a consequence of the strong quantum fluctuations present in 1D (especially at large U/nJ values), the dynamics of the quasi-BEC results dissipative even at velocities smaller then v_c, as manifested by the presence of a significant damping rate before the dynamical instability sets in. At the origin of such dissipation process there are the quantum (and thermal) phase slips.

In order to discriminate the phase slips activated by quantum tunneling from those that are thermally assisted, we performed further transport measurements with a small lattice depth ($s = 1$). Such measurements in particular showed a regime of weak phase-slip dissipation at small velocity and interaction and a second regime of stronger, velocity-dependent dissipation for larger velocity and interaction. This change of behaviour, which is consistent with the predicted crossover from thermally-assisted to purely quantum phase slips, provides the first experimental evidence of quantum phase slips in an atomic superfluid.

In a second part of experiments we employed a quasi-periodic lattice to introduce a controllable *disorder* in the system. By performing coherence and transport measurements we characterized, as a function of disorder and interaction, the phase diagram describing the insulating properties of a 1D quasi-condensate. Such a diagram shows, in agreement with theoretical predictions for the Bose glass, an insulating reentrant regime which extends from weak to strong interactions sorrounding the SF. While coherence measure-

ments provide a broad crossover (as a consequence of the system inhomogeneity), momentum-dependent transport measurements allow to determine the metal-insulator transition with higher accuracy, at least in the regime of small-U.

By means of a close comparison between the experiment and a DMRG-based theory across the $\Delta - U$ diagram, we highlighted the different effects of temperature in the regimes of weak and strong interaction. While in the former regime such effects are not negligible, they are significantly less relevant in the latter one. Here, the scaling of the correlation length with temperature, obtained by ED on small-sized systems, shows a weak dependence below a crossover temperature, indicating that the strongly-correlated quantum phases predicted by the $T = 0$ theory seem to persist at the temperatures of our experiment.

In order to probe the nature of the insulating phases in the $\Delta - U$ diagram, we performed measurements of the excitation spectrum. In particular, in the regime of strong interactions, the measurements highlighted the presence of the BG coexisting with the MI in our inhomogeneous system, as demonstrated by the presence of an excitation peak (at the characteristic energy Δ) within the MI gap. Such a signature of the BG phase is then confirmed by a comparison with a model of fermionized bosons, according to which strongly interacting bosons behave as non interacting fermions and Anderson-localize in the presence of disorder.

Finally, further excitation measurements performed from weak to strong interactions, corroborate the measurements of coherence and transport in showing the opposite role played by interactions in the two regimes: while at small U interactions compete with disorder to restore the SF phase of the bosonic system, at large U they instead cooperate with disorder favoring the localization of the fermionized particles.

We now briefly discuss possible future developments of the work reported in this thesis. With regard to the dissipation mechanisms of the SF, further

studies with other types of obstacles to the superflow, such as individual defects [140] or disorder [111, 140], might allow an assessment of other general models for quantum phase slips [121, 141]. As for the finite-T problem, an open question is whether the persisting presence of an insulating behaviour of the system in the weak-U regime, despite its relevant thermal effects, might be somehow related to the proposed many-body localization phenomenon [129, 130].

More in general, the coherence, transport and spectroscopic techniques we employed for studying the physics of 1D bosons could be also applied to systems with a different type of disorder or with higher dimensionality. As for the spectroscopic technique, for example, measurements of the excitation spectrum with speckle potentials or with holographic potentials created by spatial light modulators [142], would allow to highlight the spectral features of the strongly-interacting BG without the interference of the Mott physics due to the lattice. For its analogies to condensed matter systems, another line of interesting research would be the physics of disorder induced by impurities. Such a physics could be investigated by employing for example quantum atomic mixtures [143, 144].

BIBLIOGRAPHY

[1] M. H. Anderson, J. R. Ensher, M. R. Matthews, C. E. Wieman and E. A. Cornell, *Science*, **269**, 198 (1995).

[2] Bose-Einstein condensation in atomic gases, *Proceedings of the International School of Physics 96 "Enrico Fermi"*, course CXL, edited by M. Inguscio, S. Stringari, and C. E. Wieman, IOS Press, Amsterdam (1999).

[3] M. Raizen, C. Salomon, and Q. Niu, *Phys. Today*, **50**, 30 (1997).

[4] J. H. Denschlag, J. E. Simsarian, H. Häffner, C. McKenzie, A. Browaeys, D. Cho, K. Helmerson, S. L. Rolston, and W. D. Phillips, *J. Phys. B*, **35**, 3095 (2002).

[5] O. Morsch, J. H. Müller, M. Cristiani, D. Ciampini, and E. Arimondo, *Phys. Rev. Lett.* **87**, 140402 (2001).

[6] S. Inouye, M. R. Andrews, J. Stenger, H. J. Miesner, D. M. Stamper-Kurn, and W. Ketterle, Observation of Feshbach resonances in a Bose-Einstein condensate, *Science*, **392**, 151 (1998).

[7] S. L. Cornish, N. R. Claussen, J. L. Roberts, E. A. Cornell, and C. E.

Wieman, Stable ^{85}Rb Bose-Einstein Condensates with Widely Tunable Interactions, *Phys. Rev. Lett.* **85**, 1795 (2000).

[8] M. R. Matthews, B. P. Anderson, P. C. Haljan, D. S. Hall, C. E. Wieman, and E. A. Cornell, *Phys. Rev. Lett.* **83**, 2498 (1999).

[9] F. Chevy, K. W. Madison, and J. Dalibard, *Phys. Rev. Lett.* **85**, 2223 (2000).

[10] C. Raman, M. Köhl, R. Onofrio, D. S. Durfee, C. E. Kuklewicz, Z. Hadzibabic, and W. Ketterle, *Phys. Rev. Lett.* **83**, 2502 (1999).

[11] A. Polkovnikov, E. Altman, E. Demler, B. Halperin, M.D. Lukin, *Phys. Rev. A*, **71**, 063613 (2005).

[12] M. Greiner, O. Mandel, T. Esslinger, T. W. Hänsch, and I. Bloch, Quantum phase transition from a superfluid to a Mott insulator in a gas of ultracold atoms, *Nature*, **415**, 39 (2002).

[13] P. W. Anderson, *Phys. Rev.* **109**, 1492 (1958).

[14] J. Billy, V. Josse, Z. Zuo, A. Bernard, B. Hambrecht, P. Lugan, D. Clèment, L. Sanchez-Palencia, P. Bouyer, A. Aspect, Direct observation of Anderson localization of matter waves in a controlled disorder, *Nature*, **453**, 891 (2008).

[15] G. Roati, C. D' Errico, L. Fallani, M. Fattori, C. Fort, M. Zaccanti, G. Modugno, M. Modugno, M. Inguscio, Anderson localization of a non-interacting Bose-Einstein condensate, *Nature*, **453**, 895 (2008).

[16] M. P. A. Fisher, P. B. Weichman, G. Grinstein, and D. S. Fisher. Boson localization and the superfluid-insulator transition. *Phys. Rev. B*, **40**, 546–570 (1989).

[17] T. Giamarchi and H. J. Schulz. Anderson localization and interactions in one dimensional metals. *Phys. Rev. B*, **37**, 325–340 (1988).

[18] H. Gersch, G. Knollman, Quantum Cell Model for Bosons. *Phys. Rev.*, **129**, 959 (1963).

[19] A. Einstein, Sitzber. Kgl. preuss. Akad. Wiss., 261 (1924); ibidem, **3** (1925).

[20] S. N. Bose, *Z. Phys.* **26**, 178 (1924).

[21] W. Ketterle, D. S. Dur fee, and D. M. Stamper-Kurn. Making, probing and understanding Bose-Einstein condenstates, *Proceedings of the Inter national School of Physics "Enrico Fermi"*, course CXL (IOS Press, 1999).

[22] L. D. Landau and E. M. Lifshitz, Statistical Physics, Pergamon Press, Oxford (1969).

[23] H. Feshbach, A Unified Theory of Nuclear Reactions, *Ann. Phys.* **5**, 357 (1958).

[24] H. Feshbach, A Unified Theory of Nuclear Reactions. II, *Ann. Phys.* **19**, 287 (1962).

[25] U. Fano, Sullo spettro di assorbimento dei gas nobili presso il limite dello spettro d'arco, *Nuovo Cimento*, **12**, 156 (1935).

[26] C. Chin, V. Vuletić, A. J. Kerman, and S. Chu, High Resolution Feshbach Spectroscopy of Cesium, *Phys. Rev. Lett.* **85**, 2717 (2000).

[27] C. Chin, R. Grimm, P. Julienne, and E. Tiesinga, Feshbach Resonances in Ultracold Gases, *eprint arXiv*:0812.1496 (2008).

[28] A. J. Moerdijk, B. J. Verhaar, and A. Axelsson, *Phys. Rev. A*, **51**, 4852 (1995).

[29] G. Roati, M. Zaccanti, C. D'Errico, J. Catani, M. Modugno, A. Simoni, M. Inguscio, and G. Modugno, Bose-Einstein Condensate with Tunable Interactions, *Phys. Rev. Lett.* **99**, 010403 (2007).

[30] G. Roati, Quantum degenerate Potassium-Rubidium mixtures, PhD Thesis, University of Trento (2003).

[31] F. Ferlaino, Atomic Fermi gases in an optical lattice, PhD Thesis, University of Florence (2004).

[32] E. de Mirandes, Bloch oscillations of ultracold atoms, PhD thesis, University of Florence (2005).

[33] C. D'Errico, Osservazione di Risonanze di Fano-Feshbach in miscele atomiche K-Rb, Master Thesis, University of Florence (2005).

[34] M. Zaccanti, Tuning of the interactions in ultracold K-Rb quantum gases, PhD thesis, University of Florence (2007).

[35] H. Wang, A. N. Nikolov, J. R. Ensher, P. L. Gould, E. E. Eyler, and W. C. Stwalley, *Phys. Rev. A*, **62**, 052704 (2000).

[36] T. Loftus, C. A. Regal, C. Ticknor, J. L. Bohn, and D. S. Jin, Resonant Control of Elastic Collisions in an Optically Trapped Fermi Gas of Atoms, *Phys. Rev. Lett.* **88**, 173201 (2002).

[37] Y. Kagan, E. L. Surkov, and G. V. Shlyapnikov, Evolution and Global Collapse of Trapped Bose Condensates under Variations of the Scattering Length, *Phys. Rev. Lett.* **79**, 2604 (1997).

[38] C. A. Sackett, H. T. C. Stoof, and R. G. Hulet, Growth and Collapse of a Bose-Einstein Condensate with Attractive Interactions, *Phys. Rev. Lett.* **80**, 2031 (1998).

[39] M. Ueda and A. J. Leggett, Macroscopic Quantum Tunneling of a Bose-Einstein Condensate with Attractive Interaction, *Phys. Rev. Lett.* **80**, 1576 (1998).

[40] M. Prevedelli, F. S. Cataliotti, E. A. Cornell, J. R. Ensher, C. Fort, L. Ricci, G. M. Tino, and M. Inguscio, Trapping and cooling of potassium

isotopes in a double-magneto-optical-trap apparatus, *Phys. Rev. A*, **59**, 886 (1999).

[41] L. De Sarlo, P. Maioli, G. Barontini, J. Catani, F. Minardi, and M. Inguscio, Collisional properties of sympathetically cooled, *Phys. Rev. A* **75**, 022715 (2007).

[42] F. Ferlaino, C. D'Errico, G. Roati, M. Zaccanti, M. Inguscio, and G. Modugno, Feshbach spectroscopy of a K-Rb atomic mixture, *Phys. Rev. A*, **73**, 040702(R) (2006).

[43] A. Simoni, M. Zaccanti, C. D'Errico, M. Fattori, G. Roati, M. Inguscio, and G. Modugno Near-threshold model for ultracold KRb dimers from interisotope Feshbach spectroscopy, *Phys. Rev. A*, **77**, 052705 (2008).

[44] M. Landini, S. Roy, G. Roati, A. Simoni, M. Inguscio, G. Modugno, and M. Fattori. Direct evaporative cooling of ^{39}K atoms to Bose-Einstein condensation. *Phys. Rev. A*, **86**, 033421 (2012).

[45] P. A. Lee and T. V. Ramakrishnan, *Rev. Mod. Phys.* **57**, 287 (1985).

[46] J. W. Goodman. Speckle Phenomena in Optics: Theory and Applications. Roberts and Company Publishers (2007).

[47] J. W. Goodman, J. C. Dainty, Laser speckle and related phenomena, Springer-Verlag, Berlin (1975).

[48] M. Francon, La Granularité Laser (speckle) et ses applications en optique, Masson, Paris (1978).

[49] S. Aubry and G. André, *Ann. Israel Phys. Soc.* **3**, 133 (1980).

[50] D. R. Grempel, S. Fishman, and R. E. Prange, *Phys. Rev. Lett.* **49**, 833 (1982).

[51] V. Guarrera, L. Fallani, J. E. Lye, C. Fort and M. Inguscio, *New J. Phys.* **9**, 107 (2007).

[52] A. Schwartz, M. Dressel, G. Grüner, V. Vescoli, L. Degiorgi, and T. Giamarchi, On-chain electrodynamics of metallic (TMTSF)2X salts: Observation of Tomonaga-Luttinger liquid response, *Phys. Rev. B*, **58**, 1261 (1998).

[53] J. Hager, R. Matzdorf, J. He, R. Jin, D. Mandrus, M. A. Cazalilla, and E. W. Plummert, Non-Fermi-liquid behavior in quasi-one-dimensional $Li_{0.9}Mo_6O_{17}$, *Phys. Rev. Lett.* **95**, 186402 (2005).

[54] F. Wang, J. V. Alvarez, J. W. Allen, S.-K. Mo, J. He, R. Jin, D. Mandrus, and H. Höchst, Quantum Critical Scaling in the Single-Particle Spectrum of a Novel Anisotropic Metal, *Phys. Rev. Lett.* **103**, 136401 (2009).

[55] T. Giamarchi, Theoretical Framework for Quasi-One Dimensional Systems, *Chem. Rev.* **104 (11)**, 5037 (2004).

[56] A. G. Lebed (Editor), The physics of organic superconductors and conductors, Springer Series in Material Science, vol. 110 (Springer, 2008).

[57] D. A. Tennant and R. A. Cowley, Measurement of the spin-excitation continuum in one-dimensional $KCuF_3$ using neutron scattering, *Phys. Rev. B*, **52**, 13368 (1995).

[58] E. Dagotto, Correlated electrons in high-temperature superconductors, *Rev. Mod. Phys.* **66**, 763 (1994).

[59] E. Dagotto and T. M. Rice, Surprises on the way from one- to two-dimensional quantum magnets: The ladder materials, *Science*, **271**, 5249 (1996).

[60] E. Dagotto, Experiments on ladders reveal a complex interplay between a spin-gapped normal state and superconductivity, *Rep. Prog. Phys.* **62**, 1525 (1999).

[61] M. P. A. Fisher and L. I. Glazman, Transport in a one-dimensional Luttinger liquid, in Proceeding of the NATO Advanced Study Institute on Mesoscopic electron transport ed. by L. L. Sohn, L. Kowenhoven, G. Schön (Kluwer Academic Publishers, Dordrecht, 1997).

[62] O. M. Auslaender, A. Yacoby, R. de Picciotto, K. W. Baldwin, L. N. Pfeiffer, and K. W. West, Tunneling spectroscopy of the elementary excitations in a one-dimensional wire, *Science*, **295**, 825-828 (2002).

[63] R. Fazio and H. van der Zant, Quantum phase transitions and vortex dynamics in superconducting networks, *Phys. Rep.* **355**, 235 (2001).

[64] X. G. Wen, Topological orders and edge excitations in fractional quantum Hall states, *Adv. Phys.* **44**, 405 (1995).

[65] M. S. Dresselhaus, G. Dresselhaus, and P. C. Eklund, Science of fullerenes and carbon nanotubes (Academic Press, San Diego, 1995).

[66] H. Ishii, H. Kataura, H. Shiozawa, H. Yoshioka, H. Otsubo, Y. Takayama, T. Miyahara, S. Suzuki, Y. Achiba, M. Nakatake, T. Narimura, M. Higashiguchi, K. Shimada, H. Namatame, M. Taniguchi, Direct observation of Tomonaga-Luttinger-liquid state in carbon nanotubes at low temperatures, *Nature*, **426**, 540 (2003).

[67] D. Jerome and H. J. Schulz, *Adv. Phys.* **31**, 299 (1982).

[68] L. F. Lou, *J. Appl. Phys.* **66**, 979 (1989).

[69] S. Srivastava and B. N. Avasthi, *J. Materials Science* **27**, 3693 (1992).

[70] F. D. M. Haldane, Effective harmonic-fluid approach to low-energy properties of one-dimensional quantum fluids, *Phys. Rev. Lett.* **47**, 1840 (1981).

[71] E. H. Lieb and W. Liniger. Exact Analysis of an Interacting Bose Gas. I. The General Solution and the Ground State. *Phys. Rev.*, **130**, 1605–1616 (1963).

[72] M. Girardeau. Relationship between Systems of Impenetrable Bosons and Fermions in One Dimension. *J. Math. Phys.*, **1**, 516 (1960).

[73] D. Jacksch, C. Bruder, J. I. Cirac, C. W. Gardiner and P. Zoller, *Phys. Rev. Lett.* **81**, 3108 (1998).

[74] G. Roux, T. Barthel, I. P. McCulloch, C. Kollath, U. Schollwöck and T. Giamarchi, *Phys. Rev. A*, **78**, 023628 (2008).

[75] W. S. Bakr, A. Peng, M. E. Tai, R. Ma, J. Simon, J. I. Gillen, S. Folling, L. Pollet, and M. Greiner, Probing the Superuid to Mott Insulator Transition at the Single Atom Level, arXiv:1006.0754v1 (2010).

[76] C. Fort, L. Fallani, V. Guarrera, J. Lye, M. Modugno, D.S. Wiersma, and M. Inguscio, *Phys. Rev. Lett.* **95**, 170410 (2005).

[77] I. Bloch, J. Dalibard, and W. Zwerger, Many-body physics with ultracold gases, *Rev. Mod. Phys.* **80**, 885 (2008).

[78] B. Kramer, and A. MacKinnon, *Rep. Prog. Phys.* **56**, 1469 (1993).

[79] A. Aspect and M. Inguscio. Anderson localization of ultracold atoms. *Physics Today*, **62**(8), 30 (2009).

[80] C. Aulbach, A. Wobst, G. L. Ingold, P. Hanggi, and I. Varga, *New J. Phys.* **6** (2004).

[81] E. Abrahams, P. W. Anderson, D. C. Licciardello, and T. V. Ramakrishnan, *Phys. Rev. Lett.* **42**, 673 (1979).

[82] C. D'Errico, Anderson localization of a weakly interacting Bose-Einstein condensate, PhD Thesis, University of Florence (2009).

[83] P. Pedri, *et al.*, *Phys. Rev. Lett.* **87**, 220401 (2001).

[84] G. Roati, C. D'Errico, L. Fallani, M. Fattori, C. Fort, M. Zaccanti, G. Modugno, M. Modugno, and M. Inguscio, *Nature* **453**, 895 (2008).

[85] B. Deissler, M. Zaccanti, G. Roati, C. D'Errico, M. Fattori, M. Modugno, G. Modugno and M. Inguscio, *Nature Phys.* **6**, 354 (2010).

[86] J. M. F. Gunn, *et al. J. Phys.: Condens. Matter*, **2**, 7753-7768 (1990).

[87] R. T. Scalettar, G. G. Batrouni and G. T. Zimanyi, *Phys. Rev. Lett.* **66**, 3144-3147 (1991).

[88] B. Damski , J. Zakrewski, L. Santos, P. Zoller and M. Lewenstein *Phys. Rev. Lett.* **991**, 080403 (2003).

[89] P. Lugan, D. Clément, P. Bouyer, A. Aspect, M. Lewenstein and L. Sanchez-Palencia, *Phys. Rev. Lett.* **98**, 170403 (2007).

[90] G. Roux, T. Barthel, I. P. McCulloch, C. Kollath, U. Schollwöck and T. Giamarchi, *Phys. Rev. A*, **78**, 023628 (2008).

[91] L. Fontanesi, M. Wouters and V. Savona, *Phys. Rev. Lett.* **103**, 030403 (2009).

[92] L. Fallani, J. E. Lye, V. Guarrera, C. Fort, and M. Inguscio, Ultracold Atoms in a Disordered Crystal of Light: Towards a Bose Glass, *Phys. Rev. Lett.* **98**, 130404 (2007).

[93] L. P. Pitaevskii and S. Stringari, Bose–Einstein Condensation, Clarendon Press, Oxford, (2003).

[94] L. D. Landau. The theory of superfluidity of helium II. *J. Phys. USSR*, **5**, 71 (1941).

[95] Van Der Boog, A. G. M.; Husson, L. P. J.; Disatnik, Y.; Kramers, H. C. Experimental results on the velocity of second sound and the viscosity in dilute ^{3}He-^{4}He mixtures. *Physica B+C* **104 (3)**, 303 (1981)

[96] O. M. Marago, S. A. Hopkins, J. Arlt, E. Hodby, G. Hechenblaikner, and C. J. Foot, *Phys. Rev. Lett.* **84**, 2056 (2000).

[97] H.R. Glyde, R.T. Azuah and W.G. Stirling, *Phys. Rev. B*, **62**, 14337-14349 (2000).

[98] C. J. Pethick, H. Smith, Bose-Einstein condensation in Diluite Gases, Cambridge University Press (2001).

[99] M. Olshanii. Atomic Scattering in the Presence of an External Confinement and a Gas of Impenetrable Bosons. *Phys. Rev. Lett.*, **81**, 938–941 (1998).

[100] S. Richard, F. Gerbier, J. Thywissen, M. Hugbart, P. Bouyer, and A. Aspect, *Phys. Rev. Lett.* **91**, 010405 (2003).

[101] U. Schollwöck, *Rev. Mod. Phys.* **77**, 259 (2005).

[102] I.P. McCulloch, J. Stat. Mech.: Theor. Exp., P10014 (2007).

[103] T. Giamarchi, Quantum physics in one dimension (Clarendon, Oxford, 2004).

[104] D. S. Petrov, G. V. Shlyapnikov, J. T. M. Walraven, *Phys. Rev. Lett.* **85**, 3745 (2000).

[105] J. Sirker, A. Klumper, *Phys. Rev. B*, **66**, 245102 (2002).

[106] E. Hodby, The Superfluid Properties of a Bose-Einstein Condensed Gas, PhD thesis, University of Oxford (2002).

[107] S. Scaffidi, Trasporto di un superfluido in un potenziale periodico unidimensionale, Master thesis, Università di Palermo (2014).

[108] A. Smerzi, A. Trombettoni, P. G. Kevrekidis, and A. R. Bishop, *Phys. Rev. Lett.* **89**, 170402 (2002).

[109] H. Pu, L. O. Baksmaty, W. Zhang, N. P. Bigelow, and P. Meystre. Effective-mass analysis of Bose-Einstein condensates in optical lattices: Stabilization and levitation. *Phys. Rev. A*, **67**, 043605 (2003).

[110] E. Altman, A. Polkovnikov, E. Demler, B. I. Halperin, and M. D. Lukin. Superfluid-Insulator Transition in a Moving System of Interacting Bosons. *Phys. Rev. Lett.*, **95**, 020402 (2005).

[111] L. Tanzi, E. Lucioni, S. Chaudhuri, L. Gori, A. Kumar, C. D'Errico, M. Inguscio, and G Modugno. Transport of a Bose Gas in 1D Disordered Lattices at the Fluid-Insulator Transition. *Phys. Rev. Lett.* **111**, 115301, (2013).

[112] J. Mun, P. Medley, G. K. Campbell, L. G. Marcassa, D. E. Pritchard, and W. Ketterle. Phase Diagram for a Bose-Einstein Condensate Moving in an Optical Lattice. *Phys. Rev. Lett.*, **99**, 150604 (2007).

[113] K.Yu. Arutyunov, D.S. Golubev, A.D. Zaikin, Superconductivity in one dimension, arXiv:0805.2118

[114] I. Danshita and A. Polkovnikov. Superfluid-to-Mott-insulator transition in the one-dimensional Bose-Hubbard model for arbitrary integer filling factors. *Phys. Rev. A*, **84**, 063637 (2011).

[115] L. D. Landau and V. L. Ginzburg, Zh. Eksp. Teor. Fiz. **20**, 1064 (1950).

[116] J.S. Langer, and V. Ambegaokar, *Phys. Rev.* **164**, 498 (1967).

[117] D. McCumber, and B. Halperin, *Phys. Rev. B*, **1**, 1054 (1970).

[118] N. Giordano, *Phys. Rev. Lett.* **61**, 2137 (1988).

[119] C. N. Lau, N. Markovic, M. Bockrath, A. Bezryadin, and M. Tinkham, *Phys. Rev. Lett.* **87**, 217003 (2001).

[120] K.Yu. Arutyunov, D.S. Golubev, and A.D. Zaikin, *Phys. Rep.* **464**, 1 (2008).

[121] H. P. Büchler, V. B. Geshkenbein, and G. Blatter, *Phys. Rev. Lett.* **87**, 100403 (2001).

[122] I. Danshita. Universal Damping Behavior of Dipole Oscillations of One-Dimensional Ultracold Gases Induced by Quantum Phase Slips. *Phys. Rev. Lett.* **111**, 025303 (2013).

[123] L. Tanzi, S. S. Abbate, F. Cataldini, L. Gori, E. Lucioni, C. D'Errico, M. Inguscio, and G. Modugno. Evidence of quantum phase slips in 1D atomic superfluids. To be submitted to *Phys. Rev. Lett.*.

[124] I. Danshita and A. Polkovnikov, *Phys. Rev. A*, **85**, 023638 (2012).

[125] C. D'Errico, E. Lucioni, L. Tanzi, L. Gori, G. Roux, I. P. McCulloch, T. Giamarchi, M. Inguscio, and G. Modugno. Observation of a Disordered Bosonic Insulator from Weak to Strong Interactions. *Phys. Rev. Lett.* **113**, 095301, (2014).

[126] Z. Ristivojevic, A. Petkovic, P. Le Doussal, and T. Giamarchi. Phase transition of interacting disordered bosons in one dimension. *Phys. Rev. Lett.* **109**, 026402 (2012).

[127] M. A. Cazalilla, R. Citro, T. Giamarchi, E. Orignac and M. Rigol. One dimensional bosons: from condensed matter systems to ultracold gases. *Rev. Mod. Phys.* **83**, 1405 (2011).

[128] S. Khlebnikov and L. P. Pryadko. Quantum Phase Slips in the Presence of Finite-Range Disorder. *Phys. Rev. Lett.* **95**, 107007 (2005).

[129] I. L. Aleiner, B. L. Altshuler, G. V. Shlyapnikov, *Nature Physics* **6**, 900 (2010).

[130] V. Michal, B. L. Altshuler, G. V. Shlyapnikov, arXiv.1402.4796.

[131] F. Gerbier, Phys. Rev. Lett. **99**, 120405 (2007).

[132] N. Nessi, A. Iucci, Phys. Rev. A, **84**, 063614 (2011).

[133] J. Catani, G. Barontini, G. Lamporesi, F. Rabatti, G. Thalhammer, F. Minardi, S. Stringari, and M. Inguscio, *Phys. Rev. Lett.* **103**, 140401 (2009).

[134] G. Orso, A. Iucci, M. A. Cazalilla, and T. Giamarchi. Lattice modulation spectroscopy of strongly interacting bosons in disordered and quasiperiodic optical lattices. *Phys. Rev. A*, **80**, 033625 (2009).

[135] T. Stf̈erle, H. Moritz, C. Schori, M. Köhl, and T. Esslinger. Transition from a Strongly Interacting 1D Superfluid to a Mott Insulator. *Phys. Rev. Lett.* **92**, 130403 (2004).

[136] C. Kollath, A. Iucci, T. Giamarchi, W. Hofstetter, and U. Schollwc̈k. Spectroscopy of Ultracold Atoms by Periodic Lattice Modulations. *Phys. Rev. Lett.* **97**, 050402 (2006).

[137] D. Clément, N. Fabbri, L. Fallani, C. Fort, and M. Inguscio. Exploring Correlated 1D Bose Gases from the Superfluid to the Mott-Insulator State by Inelastic Light Scattering. *Phys. Rev. Lett.* **102**, 155301 (2009).

[138] A. Iucci, M. A. Cazalilla, A. F. Ho, and T. Giamarchi. Energy absorption of a Bose gas in a periodically modulated optical lattice. *Phys. Rev. A*, **73**, 041608 (2006).

[139] G. Pupillo, A. M. Rey, C. J. Williams, and C. W. Clark. Extended fermionization of 1d bosons in optical lattices. *New J. Phys.*, **8 (8)**, 161 (2006).

[140] D. Dries, S. E. Pollack, J. M. Hitchcock, and R. G. Hulet, *Phys. Rev. A*, **82**, 033603 (2010).

[141] S. Khlebnikov and L.P. Pryadko, *Phys. Rev. Lett.* **95**, 107007 (2005).

[142] D. McGloin, G. C. Spalding, H. Melville, W. Sibbett and K. Dholakia, Applications of spatial light modulators in atom optics, Vol. 11, No. 2 optics express, 158 (2003).

[143] U. Gavish and Y. Castin, Matter-Wave Localization in Disordered Cold Atom Lattices, *Phys. Rev. Lett.* **95**, 020401 (2005).

[144] M. Antezza, Y. Castin and D. Hutchinson, Quantitative study of two- and three-dimensional strong localization of matter waves by atomic scatterers, *Phys. Rev. A*, **82**, 043602 (2010).